CHEMICAL ENRICHMENT OF THE EARLY SOLAR SYSTEM

Matthew David Goodson

A dissertation submitted to the faculty at the University of North Carolina at Chapel Hill in partial fulfillment of the requirements for the degree of Doctor of Philosophy in the Department of Physics and Astronomy.

Chapel Hill
2017

Approved by:

Fabian Heitsch

Joaquín E. Drut

Charles R. Evans

Christian Iliadis

Nicholas M. Law

ABSTRACT

Matthew David Goodson: Chemical Enrichment of the Early Solar System. (Under the direction of Fabian Heitsch.)

Meteorites preserved from the birth of the solar system over 4.5 billion years ago contain the chemical signature of a nearby contemporaneous stellar explosion in the form of short-lived radioisotopes (SLRs) such as Aluminum-26. Yet results from hydrodynamical models of SLR injection into the pre-solar cloud or disk encounter a common problem: it is difficult to sufficiently mix the hot, enriched gas into the cold, dense, cloud without disrupting the formation of the solar system. I first consider the role of numerical methods in limiting the mixing. I implement six turbulence models in the Athena hydrodynamics code. I then explore an alternative mechanism to overcome the mixing barrier: microscopic dust grains. I numerically model the interaction of a supernova remnant containing SLR-rich dust grains with a nearby molecular cloud. The results suggest that SLR transport on dust grains is a viable mechanism to explain solar system enrichment. Finally, I attempt to constrain the formation timescale of stellar systems such as the solar system using deuterium fractionation as a "chemical clock". I determine the physical conditions necessary to reach the observed values of deuterium fraction in pre-stellar cores.

ACKNOWLEDGMENTS

Many hands and hearts have contributed to this work. I have had tremendous support from my friends, family and communities – from Lincolnton to Furman, from Big Sky to Durham, my relationships with wonderful people have shaped me into who I am and inspired me to pursue my passion.

I am eternally grateful to my wife Kimberly. Her unending love, encouragement, and understanding have sustained me in this journey. I am honored to share my life with her, through the best and worst of all that has and will come.

My family, especially my parents Stan and Linda and my brother Daniel, have always fully supported me in my endeavors. Their steadfast love and generosity has been a source of strength and hope throughout this process.

I am forever grateful to my advisor Fabian Heitsch for his guidance and wisdom in my graduate career. His gracious patience and counsel have taught me how to be a better researcher, teacher, mentor, colleague, and citizen.

I am a Tar Heel born and a Tar Heel bred, and I am immensely grateful to the Department of Physics & Astronomy at the University of North Carolina at Chapel Hill for the opportunity to study and teach here. The students, faculty, and staff have been a source of joy, knowledge, and support. A special thanks to my group mates in the Astrophysical Fluid Dynamics Lab for their help and advice: Christopher Frazer, Brandon Bartell, Christina Haig, Ryan Tanner, and Thomas Dombroski. I am especially grateful to Chris, who always lends an ear and an idea to help me solve an issue. I would also like to thank Ian Luebbers and Lindsey Yales for their important contributions to this project. Finally, I would like to thank Karl Eklund, Jenny Williams, and the rest of the folks at UNC Research Computing for their help in performing and optimizing our simulations. This work would not have been

possible without their technical expertise.

I am indebted to Jonathan Tan, Shuo Kong, and Paola Caselli for bringing me on board with the deuterium chemistry project and reminding me that there are real stars in the sky. I am also grateful to Zhaohuan Zhu, Jim Stone, Eve Ostriker, and Bruce Draine for helpful discussions about turbulent mixing, supernova remnants, and interstellar dust.

This work was supported in part by the University of North Carolina at Chapel Hill Graduate School, the North Carolina Space Grant, and the National Science Foundation under Grant AST-1109085. The work on supernova dust grains began as a summer project with Ian Luebbers through the UNC Chapel Hill Computational Physics and Astronomy Research Experience for Undergraduates, which is supported by NSF Award ACI-1156614.

"All come from dust and to dust return," yet I know there is hope.
ο πρωτος ανθρωπος εκ γησ χοικος; ο δευτερος ανθρωπος εξ ουρανου.

TABLE OF CONTENTS

LIST OF FIGURES

LIST OF TABLES

LIST OF ABBREVIATIONS

AMR	Adaptive mesh refinement
CAI	Calcium-aluminum-rich inclusion
CTU	Corner transport upwind (method)
ESS	Early solar system
ILES	Implicit large-eddy simulation
IRDC	Infrared dark cloud
ISM	Interstellar medium
KH	Kelvin-Helmholtz (instability)
LES	Large-eddy simulation
MHD	Magnetohydrodynamics
OPR	Ortho-to-para ratio
RANS	Reynold-Averaged Navier-Stokes
RM	Richtmeyer-Meshkov (instability)
RT	Rayleigh-Taylor (instability)
SLR	Short-lived radioisotope
SMR	Static mesh refinement
SN	Supernova
SNe	Supernovae
SNR	Supernova remnant
ST	Sedov-Taylor
TILES	Turbulent implicit large-eddy simulation
VL	van Leer (method)

CHAPTER 1: INTRODUCTION

1.1 Short-lived radioisotopes

The solar system formed from the gravitational collapse of an interstellar gas cloud over 4.5 Gyr ago (Amelin et al., 2010). The gas cloud has long since dissipated, but a record of its physical conditions and chemical composition is preserved in meteorites. Calcium–aluminium-rich inclusions (CAIs) in chondritic meteorites are the oldest known solar system solids, with ages of ≈ 4.567 Gyr (Amelin et al., 2002, 2010). Spectroscopic analyses of CAIs in the 1970s revealed isotopic excesses due to the *in situ* decay of short-lived radioisotopes (SLRs) (Lee et al., 1976, 1977), so named because of their half-lifetimes of $\lesssim$ a few Myr (Russell et al., 2001; McKeegan & Davis, 2007). Table 1.1 summarizes the SLRs present in the early solar system (ESS) and their relative abundances inferred from meteoritic studies.

The importance of these SLRs in solar system evolution lies in their radioactive nature. The SLRs present in the ESS were incorporated into small rocky bodies (planetesimals) and eventually planets, where their radioactive decay produced large amounts of heat. In particular, the decay of Aluminum-26 (denoted ^{26}Al, $\tau_{1/2} \approx 0.7$ Myr) and Iron-60[1] ($\tau_{1/2} \approx 2.6$ Myr) fueled the differentiation of planetesimals (Sahijpal et al., 2007) and the internal melting of ice in rocky bodies (Travis & Schubert, 2005) during the first 10 Myr of solar system evolution (Urey, 1955). The sustained aqueous state in these bodies due to SLR heating may have allowed the synthesis of amino acids – the biomolecular precursors for life (Cobb & Pudritz, 2014). Understanding the origin of SLRs is therefore critical in assessing other planetary systems and the probability of life elsewhere in the cosmos.

[1]The number indicates the atomic mass; for these elements, the most common stable isotopes are Aluminum-27 and Iron-56.

Table 1.1: Summary of short-lived radioisotopes in the early solar system.

Parent SLR	$\tau_{1/2}$ (Myr)	Daughter Isotope	Reference Isotope	Initial Abundance Ratio	Initial ESS Mass Fraction
^{10}Be	1.5	^{10}B	^{9}Be	$3 - 10 \times 10^{-4}$	$6.5 - 22 \times 10^{-14}$
^{26}Al	0.72	^{26}Mg	^{27}Al	5.2×10^{-5}	3.3×10^{-9}
^{36}Cl	0.3	^{36}Ar	^{35}Cl	$\gtrsim 1.7 \times 10^{-5}$	9.4×10^{-11}
^{41}Ca	0.1	^{41}K	^{40}Ca	$4 - 6 \times 10^{-9}$	$3.0 - 4.5 \times 10^{-13}$
^{53}Mn	3.7	^{53}Cr	^{55}Mn	$6 - 8 \times 10^{-6}$	$8.5 - 1.1 \times 10^{-10}$
^{60}Fe	2.6	^{60}Ni	^{56}Fe	$3 - 7 \times 10^{-7}$ $\lesssim 7 - 12 \times 10^{-9}$	$4.4 - 10 \times 10^{-10}$ $1.0 - 1.8 \times 10^{-11}$
^{107}Pd	6.5	^{107}Ag	^{108}Pd	5.9×10^{-5}	2.6×10^{-13}
^{182}Hf	8.9	^{182}W	^{180}Hf	1×10^{-4}	9.0×10^{-14}

References: ^{10}Be: McKeegan et al. (2000); Srinivasan & Chaussidon (2013); ^{26}Al: Lee et al. (1976); Jacobsen et al. (2008); ^{36}Cl: Lin et al. (2005); Jacobsen et al. (2009); ^{41}Ca: Liu et al. (2012); Srinivasan & Chaussidon (2013); ^{53}Mn: Shukolyukov & Lugmair (2006); Trinquier et al. (2008); ^{60}Fe: Tachibana & Huss (2003); Mishra & Goswami (2014); Moynier et al. (2011); Tang & Dauphas (2012); ^{107}Pd: Chen & Wasserburg (1996); Schönbächler et al. (2008); ^{182}Hf: Burkhardt et al. (2008); Kruijer et al. (2014).
Initial ESS mass fraction is estimated using the initial solar abundances of Lodders (2003).
Measurements of the ^{60}Fe initial abundance based on secondary ionization mass spectrometry (SIMS) and multi-collector inductively coupled plasma mass spectrometry (MC-ICPMS) do not agree; each is therefore reported independently.

The presence and abundance of SLRs also provides clues about the birth environment of the solar system. The presence of "live" SLRs in the ESS seems remarkable; SLRs rapidly decay and must therefore either be produced locally or quickly transported through the interstellar medium (ISM) from a nearby massive, evolved nucleosynthetic source (Lee et al., 1977). In the latter case, the presence of a nearby massive star provides constraints on the birth environment of the solar system, such as cluster size (Adams, 2010) and dynamical evolution (Parker et al., 2013; Pfalzner, 2013). However, the conditions leading to enrichment are uncertain. The initial abundances of some SLRs in the ESS appear to be enhanced above the Galactic background level (Diehl et al., 2006), but similar conditions may be common in star-forming regions (Vasileiadis et al., 2013; Jura et al., 2013; Young, 2014).

The origin scenarios and initial abundances for SLRs are still a matter of debate, but it seems likely that both solar and extra-solar enrichment sources are required to explain the observed variety. Local mechanisms such as solar radiation-induced spallation reactions

can produce some SLRs (e.g. ^{10}Be) but not all (e.g. ^{60}Fe) (Heymann & Dziczkaniec, 1976; Gounelle & Meibom, 2008). Although recent estimates of the initial ^{60}Fe/^{56}Fe ratio argue against significant ^{60}Fe enrichment (Tang & Dauphas, 2012), the enhanced ^{26}Al/^{27}Al ratio probably requires external sources (Makide et al., 2013). Asymptotic giant branch (AGB) star winds (Wasserburg et al., 1994), Wolf–Rayet (WR) winds (Prantzos & Casse, 1986), or Type II (core-collapse) supernova (SN) shock waves (Cameron & Truran, 1977) could transport SLRs and contaminate the ESS at some phase of its evolution (e.g. pre-solar molecular cloud, pre-stellar core, or proto-planetary disc).

1.1.1 Supernova enrichment

Among the various enrichment sources, Type II supernovae (SNe) have received the most attention in the literature (Cameron & Truran, 1977; Foster & Boss, 1997; Ouellette et al., 2005; Pan et al., 2012). SNe are naturally associated with star-forming regions, and predicted SLR yields from SNe match reasonably well with ESS abundance estimates (Meyer & Clayton, 2000). Additional evidence is provided by the anomalous ratio of oxygen isotopes ($[^{18}O]/[^{17}O]$) in the solar system, which is best explained by enrichment from Type II SNe (Young et al., 2011).

Following the discovery of ^{26}Al in CAIs, Cameron & Truran (1977) suggested that a nearby SN could have simultaneously injected SLRs and triggered the collapse of the ESS. In this scenario, a single SN shock wave rapidly transports and deposits SLRs into an isolated marginally-stable pre-stellar core. The impinging shock wave compresses the core and triggers gravitational collapse while at the same time generating hydrodynamical instabilities at the core surface that lead to mixing of SLRs with the solar gas. Foster & Boss (1997) first demonstrated the plausibility of this scenario with hydrodynamical simulations, and subsequent iterations of the experiment (Boss et al., 2010; Boss & Keiser, 2012, 2013, 2014, 2015) have defined a range of acceptable shock wave parameters (e.g. speed, width, density) for enrichment. This 'triggered formation' scenario requires nearly perfect timing

and choreography. The SN must be close to the pre-stellar core ($\lesssim$ 0.1–4 pc) at the time of explosion to prevent significant SLR radioactive decay during transit; yet the SN shock must slow considerably (from $\gtrsim$ 2000 km s^{-1} at ejection to $\lesssim$ 70 km s^{-1} at impact) to prevent destruction of the core, requiring either large separation ($\gtrsim$ 10 pc) or very dense intervening gas ($\gtrsim$ 100 cm^{-3}). Gritschneder et al. (2012) demonstrated that injection at higher velocities (up to 270 km s^{-1}) may be possible, but this is yet to be confirmed in three-dimensional models.

The amount of SLRs injected in the 'triggered formation' scenario is typically below observed values; both Boss & Keiser (2014) and Gritschneder et al. (2012) find SLR injection efficiencies $\lesssim$ 0.01, compatible with only the lowest estimates for ESS values (Takigawa et al., 2008). Enrichment relies on hydrodynamical mixing of the ejecta into the pre-stellar gas, primarily via the Rayleigh–Taylor (RT) instability (Boss & Keiser, 2012). However, mixing in inviscid hydrodynamical simulations is controlled by numerical viscosity; because the instabilities grow fastest on the smallest scales, the details of the small-scale mixing are dominated by resolution effects. Shin et al. (2008) found that all quantities except the mixing fraction show convergence in shock-cloud simulations, similar to those performed by Boss & Keiser (2014). Hence estimates of the SLR injection from hydrodynamical simulations may be underestimated due to numerical effects.

1.1.2 Models for turbulent mixing

One possible means to mitigate resolution effects in hydrodynamical simulations is a turbulence model, sometimes referred to as a subgrid-scale (SGS) model (Schmidt, 2014). Turbulence models attempt to mimic the effect of unresolved small-scale turbulence on the large-scale flow, often through the addition of "turbulent" stresses. Gray & Scannapieco (2011) used a turbulence model to track metal enrichment in galactic haloes, and Pittard et al. (2009) examined the effect of turbulence models on the shock-cloud interaction. From these studies, it is difficult to assess what effect a turbulence model would have on SLR

enrichment, as the environments and physics are different in each application.

I therefore develop a common framework for two-equation Reynolds-Averaged Navier-Stokes (RANS) turbulence models (Goodson et al., 2017), and I implement six such models in the Athena hydrodynamics code (Stone et al., 2008). I verify each implementation with the standard subsonic mixing layer, although the level of agreement depends on the definition of the mixing layer width. I then test the validity of each model into the supersonic regime, showing that compressibility corrections can improve agreement with experiment. For models with buoyancy effects, I also verify the implementation via the growth of the Rayleigh-Taylor instability in a stratified medium. The models are then applied to the shock-cloud interaction in three dimensions. I focus on the mixing of shock and cloud material, comparing results from turbulence models to high-resolution simulations (up to 200 cells per cloud radius) and ensemble-averaged simulations. I find that the turbulence models lead to increased spreading and mixing of the cloud, although no two models predict the same result. Increased mixing is also observed in inviscid simulations at resolutions greater than 100 cells per radius; this suggests that the turbulent mixing only begins to be resolved at point and previous studies may underestimate the SLR injection.

1.1.3 Supernova dust grains

Even with a turbulence model, hydrodynamical mixing alone may not be sufficient to explain the enrichment of the ESS. The (linear) growth rates of the involved fluid instabilities depend on the square root of the density contrast (Chandrasekhar, 1961), resulting in an inevitable impedance mismatch between the hot, diffuse stellar ejecta and the cold, dense pre-solar core.

As an alternative, I explore the injection of SLRs via supernova dust grains as a way to overcome the mixing barrier (Goodson et al., 2016b). I numerically model the interaction of a supernova remnant containing SLR-rich dust grains with a nearby molecular cloud using the Athena code. I find that the expanding gas shell stalls upon impact with the

dense cloud, and gas-phase SLR injection occurs slowly due to hydrodynamical instabilities at the cloud surface. In contrast, dust grains of sufficient size ($\gtrsim$ 1 μm) decouple from the gas and rapidly penetrate into the cloud. Once inside the cloud, the dust grains are destroyed, releasing SLRs and rapidly enriching the dense (potentially star-forming) regions. This suggests that SLR transport on dust grains is a viable mechanism to explain SLR enrichment. Furthermore, dust grains of different sizes penetrate different distances, which could explain the discrepancy between ^{26}Al and ^{60}Fe in CAIs.

1.1.4 Massive star formation timescales

As indicated above, the primary source of SLRs is massive, evolved stars ($> 8M_{\odot}$). A key constraint on models of supernova enrichment is the timescale for massive star formation (Gounelle et al., 2009; Gaidos et al., 2009). Since the SLRs rapidly decay, the SN must be close to the ESS in both time and distance, preferably within the same molecular cloud complex. Since the age spreads of clusters are small (Hartmann et al., 2001; Hartmann, 2003), enrichment is most likely if the SN progenitor forms first and forms rapidly. Yet it is unclear from dynamical observations whether massive stars form slowly (Tan et al., 2013) or rapidly (Vázquez-Semadeni et al., 2007). An alternative means to probe the age and state of massive starless cores is using chemical tracers, in particular deuterated molecules (Ceccarelli et al., 2014). In sufficiently dense ($n_{\rm H} > 10^5$ cm^{-3}), cold ($T < 20$ K) environments, CO freeze-out opens a pathway for ion-neutral reactions that increase the deuterium fraction, i.e., the ratio of deuterated to non-deuterated species, $D_{\rm frac}$. High levels of deuterium fraction in N_2H^+ are observed in some pre-stellar cores (Kong et al., 2016). Single-zone chemical models find that the timescale required to reach observed values ($D_{\rm frac}^{\rm N_2H^+} \equiv N_2D^+/N_2H^+ \gtrsim 0.1$) is longer than the free-fall time, possibly ten times longer (Kong et al., 2015).

I explore the collapse and deuteration of turbulent, magnetized cores with 3D magnetohydrodynamics simulations (Goodson et al., 2016a). I construct an approximate chemical model to follow the growth in abundances of N_2H^+ and N_2D^+. I then examine the dynamics

of the core using each tracer for comparison to observations (Kong et al., 2017). I find that the velocity dispersion of the core as traced by N_2D^+ appears slightly sub-virial compared to predictions of the Turbulent Core Model of McKee & Tan (2003), except at late times just before the onset of protostar formation. By varying the initial mass surface density, the magnetic energy, the chemical age, and the ortho-to-para ratio of H_2, I also determine the physical and temporal properties required for high deuteration. I find that low initial ortho-to-para ratios ($\lesssim 0.01$) and/or multiple free-fall times ($\gtrsim 3$) of prior chemical evolution are necessary to reach the observed values of deuterium fraction in pre-stellar cores. This suggests that the collapse rate may be significantly slower than the free-fall time, or the deuteration process begins earlier than assumed.

1.2 Overview of contents

Chapter 2 provides an overview of the Athena magnetohydrodynamics code, as well as modifications to the code. The most significant modification to the code is described in Chapter 3, which details a suite of two-equation turbulence models. These models are applied to the generic shock-cloud interaction to investigate turbulent mixing, especially in relation to SLR injection. While this affects the gas mixing, Chapter 4 investigates a different solution to the mixing problem, namely injection of SLRs by supernova dust grains. The formation timescales of the massive stars that ultimately produce supernovae are considered in Chapter 5, specifically in relation to observed deuteration of pre-stellar cores. Finally, I conclude in Chapter 6.

CHAPTER 2: NUMERICAL METHODS

2.1 The Athena code

The evolution of an ideal, inviscid magnetized fluid is governed by three conservation equations for the mass, the momentum, and the energy:

$$\frac{\partial \rho}{\partial t} + \nabla \cdot (\rho \mathbf{u}) = 0 \tag{2.1.1}$$

$$\frac{\partial \rho \mathbf{u}}{\partial t} + \nabla \cdot (\rho \mathbf{u}\mathbf{u} - \mathbf{B}\mathbf{B} + \frac{\mathbf{B} \cdot \mathbf{B}}{2} + P\mathbf{I}) = 0 \tag{2.1.2}$$

$$\frac{\partial E}{\partial t} + \nabla \cdot [(E + P + \frac{\mathbf{B} \cdot \mathbf{B}}{2})\mathbf{u}] = 0 \tag{2.1.3}$$

with the density ρ, the velocity vector $\mathbf{u}$, the magnetic field vector $\mathbf{B}$[1], the unit dyad $\mathbf{I}$, the thermal pressure P, and the total energy density E:

$$E = \frac{P}{\gamma - 1} + \frac{1}{2}\rho |\mathbf{u}|^2 + \frac{\mathbf{B} \cdot \mathbf{B}}{2}, \tag{2.1.4}$$

where the ideal gas law $P = (\gamma - 1)e$ has been used to relate the pressure P to the internal energy density e via the adiabatic index γ. For magnetized fluids, Maxwell's relations must be coupled with the fluid equations. For an ideal (perfectly-conducting) plasma, Faraday's law and Ohm's law lead to the induction equation:

$$\frac{\partial \mathbf{B}}{\partial t} - \nabla \times (\mathbf{u} \times \mathbf{B}) = 0. \tag{2.1.5}$$

[1]The units are such that the magnetic permeability $\mu = 1$.

Finally, in many applications it is helpful to evolve a passive color field:

$$\frac{\partial \rho C}{\partial t} + \nabla \cdot (\rho \mathbf{u} C) = 0. \tag{2.1.6}$$

Color fields do not affect the dynamics; they are therefore often used to trace the flow and mixing of different fluids or to follow chemical abundances.

We use the Athena magnetohydrodynamics (MHD) code (Stone et al., 2008) to numerically solve Eqs. 2.1.1-2.1.6. Athena integrates the fluid equations using a finite-volume method on a uniform Cartesian grid in three dimensions. The hydrodynamical variables (ρ, $\mathbf{u}$, E) are represented as volume-averages at cell centers, while the magnetic fields ($\mathbf{B}$) are represented as an area-average at cell interfaces. Athena uses a high-order Godunov method; in short, the time integration is performed by computing time- and area-averaged fluxes at cell interfaces as a solution to the Riemann problem. The Riemann problem describes the one-dimensional evolution of two uniform gases initially separated by an interface. If the gas properties are discontinuous across the interface, removal of the interface will generate a family of waves that propagate through the fluids with characteristic speeds dependent on the initial conditions. The Godunov method treats the evolution of fluids through each cell interface at each time step as a Riemann initial value problem. Further details of the Riemann problem and its extension to three-dimensions are given by Toro (2009).

The Godunov method used in Athena has three main elements: the time integration scheme, the spatial reconstruction scheme, and the Riemann solver. Two directionally-unsplit integration methods are available: the corner transport upwind method (CTU) of Colella (1990) and the predictor-corrector method of van Leer (2006) (VL; see also Stone & Gardiner, 2009). Both methods employ constrained transport (CT; Evans & Hawley, 1988) to preserve the divergence–free constraint on the magnetic field. Athena uses the spatial reconstruction methods of Colella & Woodward (1984) to interpolate cell-centered quantities to the cell interfaces for evaluation of the fluxes in the Riemann method. Exact solutions of the Riemann problem are computationally expensive (Toro, 2009); therefore approximate

solutions are often used. We prefer solvers in the HLL family (Harten et al., 1983) that average over intermediate states in the Riemann problem. For hydrodynamics, we use the HLLC solver (Toro, 2009) which includes the contact wave; this is extended for MHD to include the Alfvén wave in the HLLD solver (Miyoshi & Kusano, 2005).

Athena conserves the mass, momentum, total energy, and divergence of the magnetic field to machine accuracy. Eqs. 2.1.1-2.1.6 do not include viscosity; however, the discretization, integration, and interpolation introduce numerical viscosity proportional to the grid resolution, time accuracy, and interpolation order, respectively. This allows Athena to handle non-conservative phenomena such as supersonic shocks. Eqs. 2.1.1-2.1.3 also do not include additional source terms such as gravity and radiative cooling. Gravity is implemented in Athena in a way that conserves momentum but not energy (see Section 2.2.2). Other sources, such as diffusion and radiative cooling, are implemented at first order in time via operator splitting.

2.2 Modifications to Athena

2.2.1 Dual energy formulation

Certain source terms, such as radiative cooling, require the temperature T, which is proportional to the internal energy density $e = P/(\gamma - 1)$ via the ideal gas law. Athena evolves the total energy density E, and the internal energy is evaluated by subtracting the kinetic energy $E_{\rm kin} \equiv \rho|\mathbf{u}|^2/2$ from the total energy. In regions where the kinetic energy is a significant fraction of the total energy, the difference will be susceptible to numerical errors and the internal energy returned may be non-physical ($e < 0$). Therefore, we simultaneously solve the internal energy equation:

$$\frac{\partial e}{\partial t} + \nabla \cdot (e\mathbf{u}) = -P\ \nabla \cdot \mathbf{u}. \tag{2.2.1}$$

If the internal energy is a small fraction of the total energy ($e/E \leq 10^{-3}$), we revert to using e rather than $E - E_{\rm kin}$. This "Dual Energy Formulation" is also used in Enzo (Bryan et al., 2014) and Flash (Fryxell et al., 2000). The check is performed any time the internal energy (or pressure or temperature) is required, such as calculating the pressure at cell interfaces as inputs to the Riemann solver. We prefer the dual energy formulation over a pressure or temperature floor in our models; while reverting the pressure to a small number ($\sim 10^{-20}$) may not affect the dynamics in most situations, the cooling depends very sensitively on the temperature.

The internal energy equation (Eq. 2.2.1) is not conservative. The left-hand side can be treated as an advection equation for e/ρ. We therefore use the density flux returned from the Riemann solver to advect the internal energy, treating e as a passive color field. The source term is calculated and applied at cell centers using a monotonic central difference to evaluate the gradients of the velocity in each direction. In contrast to Bryan et al. (2014), we use the updated pressure [calculated from $P = e(\gamma - 1)$] when applying the source term at the full time-step update in the integrator. The non-conservative formulation can lead to large discrepancies from the correct internal energy if the equation is allowed to evolve on its own (see Figure 2.1). Therefore, we follow the recommendation of Bryan et al. (2014) and synchronize the internal energy using the total energy when deemed safe to do so. We reset $e = (E - \rho|\mathbf{u}|^2/2)$ if $e/E_{\rm max} \geq 0.1$, where $E_{\rm max}$ is the maximum total energy of the cell and its immediate neighbours [eq. 45 of Bryan et al. (2014) with $\eta_2 = 0.1$].

Test case: Sod shock tube

The Sod shock tube is a standard hydrodynamical test case (Tasker et al., 2008). The set-up is a variant of the Riemann problem described in Section 2.1: two uniform gases are initialized with a discontinuity in the density and pressure. The analytic solution is known from the Riemann problem. $t = 0$ then corresponds to the removal of the interface, and the discontinuity should generate three waves – a shock wave, a contact wave, and a rarefaction

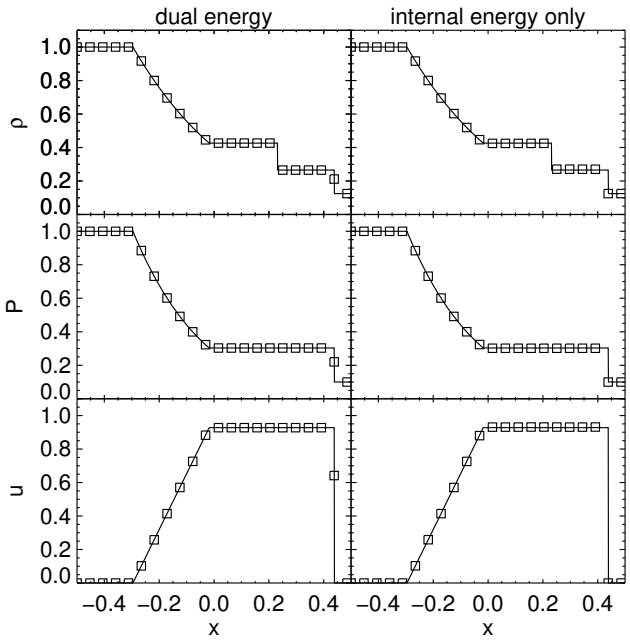

Figure 2.1: Profiles of the density, pressure, and velocity in the 1D Sod shock tube test case with 1024 grid points at $t = 0.25$ (in computational units). The analytic solution is shown as the solid line, with simulation results overplotted in open squares. From left to right in each profile are the rarefaction, contact, and shock discontinuities. The left column shows the result obtained with the standard dual energy method, while the right column shows the result when only the internal energy is used. The results show good agreement except in the shock front, which proceeds too slowly if only the internal energy is used.

wave. We test the dual energy formulation in two ways: 1) as described above with checks and syncing of the total energy, and 2) completely using the internal energy instead of the total energy. The latter represents the worst-case scenario; in practice, the internal energy is a fall-back mechanism only used in a neglible fraction of cells per time-step.

Figure 2.1 shows the density, pressure, and velocity in the Sod shock tube at $t = 0.25$ (in computational units). The left column shows the standard dual energy formulation, while the right column shows the worst-case scenario. In the standard case, the dual energy shows excellent agreement with the analytic solution; the rms error on the energy is 7.04×10^{-4}. However, if only the internal energy is evolved (and not the total energy), the shock propagates too slowly and the rms error on the energy increases to 5.26×10^{-3}. This illustrates the non-conservative nature of Eq. 2.2.1, as the source term on the right hand side creates issues; the dilatational term ($\nabla \cdot \mathbf{u}$) is large at the shock front and depends sensitively on the

method used in calculating the velocity gradients. Despite this, the internal energy is still very accurate in the rarefaction and contact regions. As previously mentioned, the internal energy is only rarely used as a fallback mechanism. Overall, the dual energy formulation maintains a high degree of accuracy while preventing unphysical states and avoiding *ad hoc* floor values.

2.2.2 Gravity

Gravity is implemented in Athena in a way that conserves momentum but not energy:

$$\frac{\partial \rho \mathbf{u}}{\partial t} + \nabla \cdot (\rho \mathbf{u}\mathbf{u} - \mathbf{B}\mathbf{B} + \frac{\mathbf{B}\cdot\mathbf{B}}{2} + P\mathbf{I} + \mathbf{T_g}) = 0 \tag{2.2.2}$$

$$\frac{\partial E}{\partial t} + \nabla \cdot [(E + P + \frac{\mathbf{B}\cdot\mathbf{B}}{2})\mathbf{u}] = -\rho \mathbf{u} \cdot \nabla \phi \tag{2.2.3}$$

where ϕ is the gravitational potential and $\mathbf{T_g}$ is the gravitational tensor defined as (Jiang et al., 2013):

$$\mathbf{T_g} = \frac{1}{4\pi G}[\nabla\phi\nabla\phi - \frac{1}{2}(\nabla\phi)\cdot(\nabla\phi)\mathbf{I}] \tag{2.2.4}$$

with G the gravitational constant. This allows the momentum change due to gravity to be treated as a flux rather than a source term. The potential ϕ is evaluated at each time step via solution of Poisson's equation,

$$\nabla^2\phi = 4\pi G\rho. \tag{2.2.5}$$

This elliptic partial differential equation can be evaluated using a variety of methods, such as multigrid methods or Fourier transforms, provided an approriate discretization and boundary conditions.

2.2.3 Gravity with SMR

Athena includes static mesh refinement (SMR) which allows for additional grid resolution in specific regions. In contrast to adaptive mesh refinement (AMR), SMR refinement

grids remain in a fixed location for the duration of the simulation. This provides strict control over where and how refinement is achieved. Unfortunately, mesh refinement complicates standard solving procedures for gravity. Athena currently does not support gravity with SMR. We have thererfore implemented a new gravitational potential solver compatible with SMR.

We follow a procedure similar to that used in Enzo (Bryan et al., 2014). We use an iterative process to determine the gravitational potential level-by-level. First, we use a standard FFT-based method to compute the potential on the root domain, for either isolated or periodic boundary conditions. We then prolongate (interpolate) the potential to set boundary conditions on the next finer level. These values are used as Dirichlet boundary conditions for a Poisson solve on the fine domain. We use the standard second-order finite-difference approximation to the Poisson equation. The resulting linear equation is solved with the Hypre library (Falgout et al., 2006). Hypre provides easy access to a variety of parallelized multigrid methods. The resulting potential is then interpolated to the next fine domain, and the process repeats. Finally, all fine domain potentials are restricted (averaged) back onto the coarse domains to reduce errors.

We use the same prolongation and restriction operators as Athena uses for the scalar hydrodynamic variables, namely those of Tóth & Roe (2002). For prolongation, this is a conservative linear interpolation with a monotonic slope limiter. The slope limiter prevents new extrema as a result of interpolation. Athena prolongates a single cell-centered coarse value into a $2 \times 2 \times 2$ (in 3D) cube of fine-grid values. The method is conservative in that the mean of the cube of values is equivalent to the coarse value. However, the linear interpolation routine is slightly inaccurate for fields with non-linear gradients. As an example, consider a smooth point-mass potential going as r^{-1}. The linear interpolation will overshoot on one side of the center and undershoot on the other side, resulting in a checkerboard pattern. The size of the errors is dependent on the steepness of the gradient, but generally this error is small. Further, the prolongation is only used to set boundary values for the potential

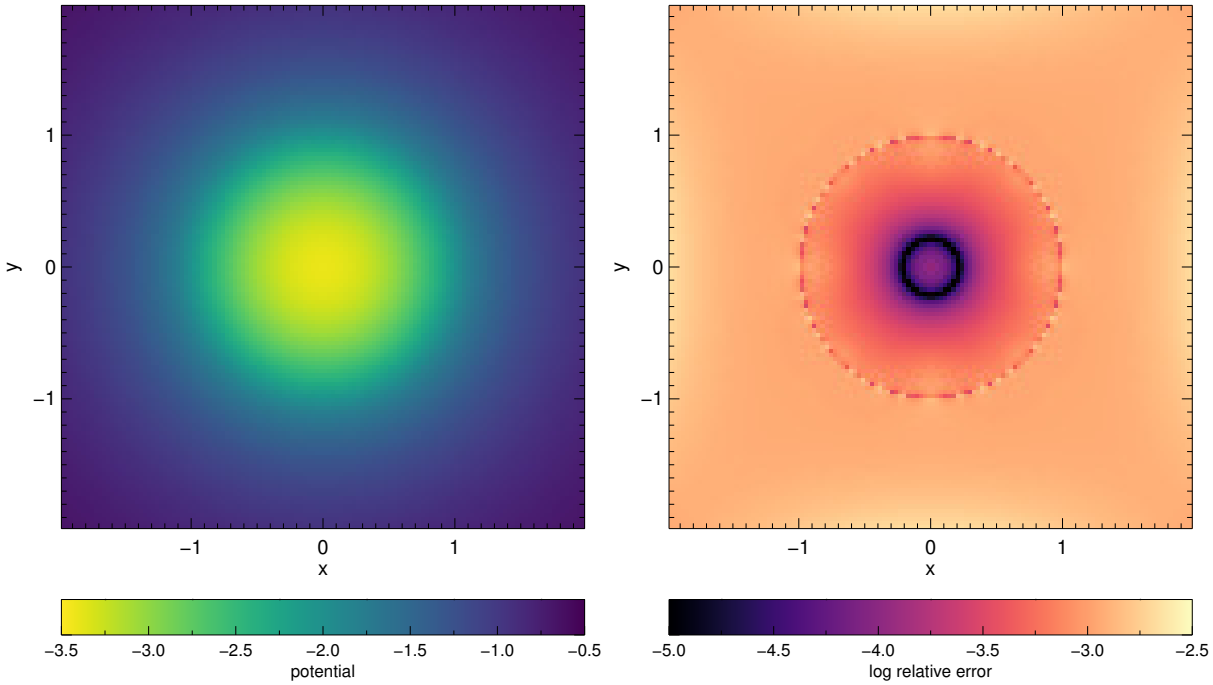

Figure 2.2: Midplane slice at $z = 0$ of the gravitational potential (left panel) resulting from an oblate spheroid determined using HYPRE on a single fixed grid of 128^3 cells. The log of the relative error is also shown (right panel). HYPRE use parallelized multigrid methods to solve the linear system resulting from the finite-difference approximation to the Poisson equation. Boundary conditions are evaluating using a high-order multipole expansion.

solve. The fine grid density field is not interpolated, and therefore the resulting potential is (overall) smooth.

Test case: MacLaurin spheroid

A homoegenous oblate spheroid (or so-called "MacLaurin" spheroid) is ideal for testing the accuracy of gravity solvers (Couch et al., 2013) because the potential can be expressed analytically (Ricker, 2008) and the partial symmetry will reveal dimension-dependent errors. We initialize a static oblate spheroid with semi-major axis $a = 1.0$, ellipticity $e = 0.9$, and uniform density $\rho = 1.0$ in a negligible background $\rho_0 = 10^{-10}$. The spheroid is centered in a simulation cube of width $L = 4.0$.

We first test our new HYPRE-based Poisson solver on a single fixed grid of 128^3 support points. We use a multipole expansion (up to octupole) to compute the potential at the

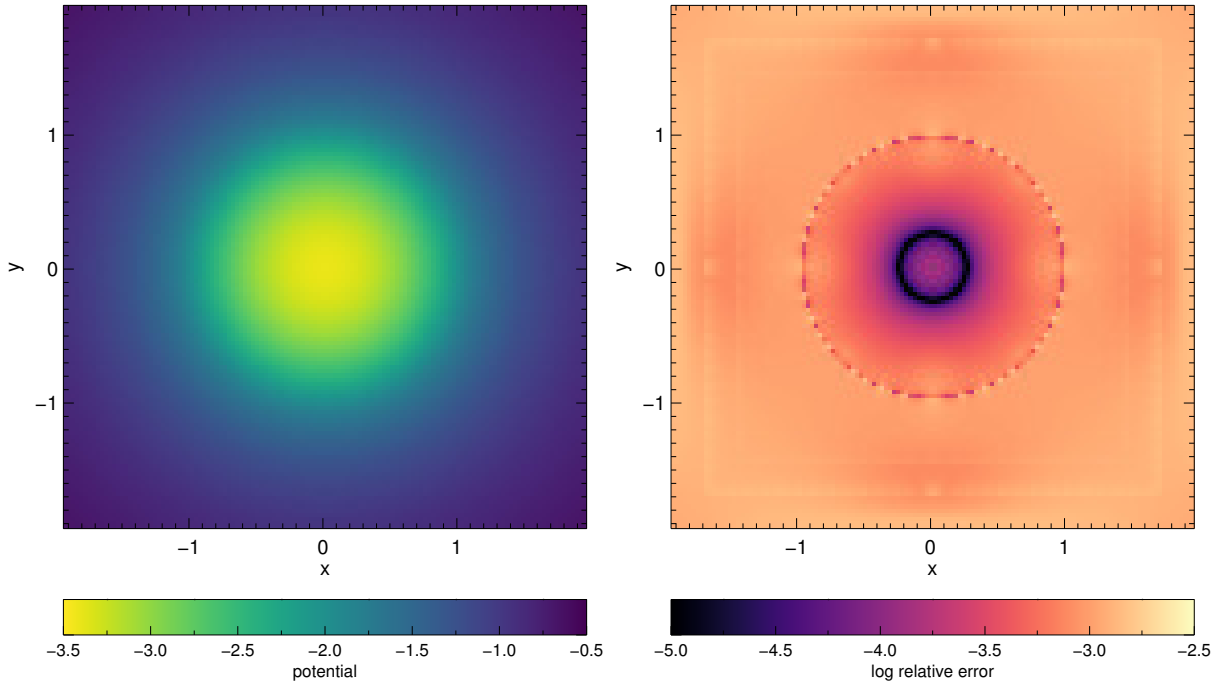

Figure 2.3: Same as Figure 2.2, but for a nested SMR grid of three levels. The root grid is 32^3, resulting in an effective resolution of 128^3. The SMR refinement boxes are barely visible in the error (right panel) due to the interpolation from coarse to fine levels.

boundaries. The solution to linear system resulting from discretization of Eq. 2.2.5 is evaluated using the generalized minimal residual (GMRES) method with a semicoarsening multigrid (SMG) pre-conditioner. Figure 2.2 shows the potential and relative error in a midplane slice at $z = 0$. Comparing to the analytic solution, our solver yields an rms relative error of 3.2×10^{-6}, with a maximum error of 3.5×10^{-3}.

We then test the solver on a nested SMR grid of three levels, with 32^3 support points on the coarest level and an effective resolution of 128^3 on the finest level. Similar to Figure 2.2, Figure 2.3 shows the potential and relative error in a midplane slice at $z = 0$. The outlines of the SMR refinement grids are visible in the error, but overall the potential is still highly accurate. Compared to the fixed grid, the rms error and maximum error are only slightly increased to 4.0×10^{-6} and 4.5×10^{-3}, respectively. Most importantly, the use of SMR reduces the computational time by over an order of magnitude, despite having to solve for the potential on multiple levels sequentially.

2.2.4 Dust dynamics

Particles, such as dust grains, follow a different equation of motion which must be solved simultaneously. We have added passive particles to the VL integrator (Stone & Gardiner, 2009) in Athena (Stone et al., 2008). The particle update is performed using the predictor values. Comparisons with the CTU integrator, which includes particles by default, show nearly absolute agreement. We have also extended Athena to include drag forces, collisional destruction, and dust evaporation; full details including a test case are presented in Section 4.2.3.

CHAPTER 3: TURBULENCE MODELS IN THE SHOCK-CLOUD INTERACTION[1]

3.1 Introduction

Since the discovery of ^{26}Al in CAIs by Lee et al. (1976), the leading hypothesis has been injection of SLRs by a nearby supernova (Cameron & Truran, 1977; Margolis, 1979). In this scenario, a SN launches a supersonic blast wave carrying SLRs into the ISM that collides with nearby molecular gas clouds (McKee & Ostriker, 1977). The impinging shock wave drives hydrodynamic instabilities at the cloud surface, such as the Rayleigh-Taylor (RT), Kelvin-Helmholtz (KH), and Richtmeyer-Meshkov (RM) instabilities (Stone & Norman, 1992), that could simultaneously inject SLRs and trigger gravitational collapse (Foster & Boss, 1997).

If the blast wave has traveled sufficient distance, or if the target cloud is sufficiently small, the blast wave can be considered approximately planar when it collides with the molecular cloud. In this case, the interaction resembles the standard shock-cloud interaction – a well-studied problem in numerical simulations (Stone & Norman, 1992; Klein et al., 1994; Xu & Stone, 1995; Nakamura et al., 2006; Pittard et al., 2009; Pittard & Parkin, 2016). Foster & Boss (1997) first performed shock-cloud simulations of SN enrichment, and subsequent shock-cloud experiments (Boss et al., 2010; Boss & Keiser, 2012, 2013, 2014, 2015) have extending the physics and parameter space. Yet these simulations encounter a common bottleneck – it remains difficult to mix the hot SN ejecta into the dense molecular cloud without disrupting the cloud. Most recently, Boss & Keiser (2015) find that less than

[1]Portions of this chapter previously appeared as an article in Monthly Notices of the Royal Astronomical Society. The original citation is as follows: Goodson, M. D., Heitsch, F., Eklund, K., & Williams, V. A. "A systematic comparison of two-equation Reynolds-averaged NavierStokes turbulence models applied to shockcloud interactions," MNRAS (2017).

10% of incident SN material is injected into a dense pre-solar core, reaching only the lowest estimates for ESS abundances (Takigawa et al., 2008).

It may be that the mixing observed in shock-cloud simulations is artificially suppressed by insufficient resolution. In Goodson et al. (2017), we explore the dynamics and mixing of the shock-cloud interaction in detail. We consider turbulence models as a means to reduce resolution effects, and we implement six models in the Athena code. We test the ability of the models to capture hydrodynamical instabilities, and we apply the models to a shock-cloud interaction in three dimensions. We find that the turbulence models predict higher levels of mixing, with injection fractions $\gtrsim 30\%$. Increased mixing is also seen in inviscid simulations only once sufficient resolution is achieved (greater than 50 cells per cloud radius). This suggests that the turbulent cascade begins to be resolved at this point, and simulations with lower resolutions may underestimate the turbulent mixing.

3.1.1 Hydrodynamical modeling of the shock-cloud interaction

In Eulerian hydrodynamics simulations, the growth of turbulence is controlled by numerical viscosity (resolution effects). Adequate resolution is therefore necessary to properly capture the dynamics. Previous work on the shock-cloud interaction has found that about 100 cells per radius are necessary for convergence of global quantities (Klein et al., 1994; Nakamura et al., 2006; Pittard et al., 2009), although this requirement may be relaxed in 3D simulations (Pittard & Parkin, 2016). However, because the instabilities grow fastest on the smallest scales, the details of the small-scale mixing are dominated by resolution effects. Shin et al. (2008, hereafter SSS08) found that all quantities except the mixing fraction show convergence in shock-cloud simulations.

One possible means to mitigate resolution effects is a turbulence model, sometimes referred to as a subgrid-scale (SGS) model. Turbulence models attempt to mimic the effect of unresolved small-scale turbulence on the large-scale flow, often through the addition of "turbulent" stresses. Such models are common in engineering codes, and they are increasingly

used in astrophysics (Schmidt et al., 2006; Scannapieco & Brüggen, 2008; Pittard et al., 2009; Gray & Scannapieco, 2011; Schmidt & Federrath, 2011; Schmidt, 2014; Pittard & Parkin, 2016). Turbulence models can be separated into two types: Reynolds-averaged Navier-Stokes (RANS) and Large-Eddy Simulations (LES). The former relies on time-averaging of the decomposed fluid equations, while the latter uses spatial filtering of variables. Here, we only consider RANS models; for a review of LES methods, see Schmidt (2014).

3.1.2 Turbulence models in the shock-cloud interaction

Both RANS and LES turbulence models have been used to model the interaction of a shock with a cloud, in different environments and with different results. Pittard et al. (2009, hereafter P09) examined the hydrodynamic shock-cloud interaction in two dimensions with the k-ε model, a two-equation RANS model. The authors argued that the k-ε turbulence model adequately captured the dynamics of the shock-cloud interaction and reduced the resolution requirements. Follow-up studies by Pittard & Parkin (2016, hereafter PP16) revealed that the k-ε model did not significantly alter the dynamics or improve the resolution convergence in three dimensional simulations.

Gray & Scannapieco (2011, hereafter GS11) used a different two-equation RANS model, based on the k-L formalism, to track metal enrichment in so-called "minihalos". An enriched supersonic galactic outflow impacts a diffuse cloud of primordial gas, subject to both gravity and radiative cooling. The authors modified the k-L model of Dimonte & Tipton (2006, hereafter DT06), which was calibrated for RT and RM instabilities, to include the KH instability and compressibility effects. Here the authors specifically investigated the turbulent mixing of metals. While there were notable differences in the enrichment of diffuse gas, the metal abundance in the dense gas was largely unaffected by the turbulence model.

Schmidt et al. (2014) applied a one-equation LES model to the simulations of Iapichino et al. (2008), which studied a cosmological minor-merger, i.e., the infall of a low-mass subcluster into a larger cluster. This resembles the shock-cloud interaction but on larger scales.

For this application, the authors used a linear eddy-viscosity relation with a dynamic procedure to calculate transport coefficients ("shear-improved" SGS model). The authors found that, while the LES turbulence model did not significantly alter the energy of the interaction, it did affect the vorticity and subsequent evolution of the infalling gas.

It is difficult to interpret and compare the effects of the turbulence models in the simulations described above. First, each application explored different physical regimes and therefore included different physics (e.g. radiative cooling, gravity). Second, some turbulence models incorporated additional effects, such as buoyancy and compressibility, that other models implicitly neglect. Third, each turbulence model affects the dynamics differently. In the case of LES, the resolved dynamics are largely unaffected, as the model only considers turbulent effects near and below the filter width, which is typically close to the grid scale. However, RANS models average out dynamical fluctuations at all scales below some characteristic length scale, which varies throughout the simulation and could be much larger than the grid scale. Fourth, the "true" solution to the shock-cloud interaction is unknown. One can compare results obtained with a turbulence model to higher-resolution simulations, but without an explicit viscosity the degree of mixing remains constrained by the numerical viscosity.

Finally, it is unclear whether these turbulence models are valid in the astrophysical regimes being probed. All turbulence models rely on closure approximations with adjustable parameters often determined by comparison with empirical results. The laboratory experiments used for calibration are typically subsonic and incompressible in nature. While some models can be modified to produce correct results in transonic and moderately compressible regimes, it is unknown whether these modifications remain valid in the highly supersonic, highly compressible conditions characteristic of the ISM.

3.1.3 Motivation and outline

In an effort to better understand the effects and validity of turbulence models in astrophysical applications such as SLR enrichment, we perform hydrodynamical simulations of the generic shock-cloud interaction with six two-equation RANS models. We first develop a common framework for two-equation turbulence models, and we implement this framework in the Athena hydrodynamics code (Stone et al., 2008). We verify the implementation of each turbulence model with the subsonic shear mixing layer test, ensuring that the width of the mixing layer grows linearly in accord with experimental results. We also highlight the dependence of the growth rate on the definition of the mixing layer width. We then test the validity of each model into the supersonic regime. Most models are known to perform poorly in transonic applications, but we explore three common "compressibility corrections" that improve results. Three of the models here considered include buoyancy effects, such as the RT instability. For these models, we further verify our implementation with a stratified medium test, in which we compare the temporal growth of the RT boundary layer to experimental results.

After determining that the turbulence models are implemented correctly, we test each turbulence model in a three-dimensional adiabatic shock-cloud interaction. We quantify not only the global dynamics but also the small-scale mixing. To examine the validity of the turbulence models, we perform a resolution convergence test of the inviscid shock-cloud interaction, up to 200 cells per radius in full 3D on a fixed grid. We also compare results to an ensemble-average of inviscid simulations initialized with grid-scale initial turbulence, scaled to roughly match the initial conditions of the turbulence models. Finally, we consider the effects of initial conditions and compressibility corrections in the turbulence models, finding that the former makes a significant difference in evolution whereas the latter does not.

We outline the six RANS turbulence models and their implementation in Athena in Section 3.2. We verify each implementation with a mixing layer test in Section 3.3, and we further verify three of the models with the stratified medium test in Section 3.4. The

turbulence models are then used in the shock-cloud simulation; the set-up and results of these simulations are presented and discussed in Section 3.5. Finally, we discuss the validity of turbulence models in astrophysical applications in Section 3.6 before concluding in Section 3.7.

3.2 Turbulence models

We extend Eqs. 2.1.1 – 2.1.6 as follows:[2]

$$\frac{\partial \rho}{\partial t} + \nabla \cdot (\rho \mathbf{u}) = 0 \tag{3.2.1}$$

$$\frac{\partial (\rho \mathbf{u})}{\partial t} + \nabla \cdot (\rho \mathbf{u}\mathbf{u} + P\mathbf{I}) = \nabla \cdot \tau' \tag{3.2.2}$$

$$\frac{\partial E}{\partial t} + \nabla \cdot [(E + P)\mathbf{u}] = \nabla \cdot (\mathbf{u}\tau' - \mathbf{q}') + \Psi_E \tag{3.2.3}$$

$$\frac{\partial (\rho C)}{\partial t} + \nabla \cdot (\rho C \mathbf{u}) = \nabla \cdot \mathbf{d}' \tag{3.2.4}$$

$$\frac{\partial (\rho k)}{\partial t} + \nabla \cdot (\rho k \mathbf{u}) = \nabla \cdot (\frac{\mu_T}{\sigma_k} \nabla k) + \Psi_k \tag{3.2.5}$$

$$\frac{\partial (\rho \xi)}{\partial t} + \nabla \cdot (\rho \xi \mathbf{u}) = \nabla \cdot (\frac{\mu_T}{\sigma_\xi} \nabla \xi) + \Psi_\xi \tag{3.2.6}$$

with the specific turbulent kinetic energy k, an auxiliary turbulence variable ξ, the turbulent stress tensor τ', the turbulent heat flux $\mathbf{q}'$, the turbulent diffusive flux $\mathbf{d}'$, turbulent viscosity μ_T, turbulent diffusion coefficients σ, and source terms due to turbulent effects Ψ. E now represents the total resolved energy density E [3].

Two-equation models are so named because they add two "turbulent" variables – the specific turbulent kinetic energy k and an auxiliary variable ξ that varies from model to model – with corresponding transport equations (Eqs. 3.2.5-3.2.6). Models are typically

[2]For simplicity of notation, we do not differentiate Reynolds-averaged $(\overline{\rho}, \overline{P})$ and Favre-averaged $(\tilde{\mathbf{u}}, \tilde{E}, \tilde{C})$ variables, where $\tilde{\phi} \equiv \overline{\rho\phi}/\overline{\rho}$.

[3]We do not include the turbulent kinetic energy ρk in the definition of total energy; therefore we are simulating the total *resolved* energy. See section 2.4.5 of Garnier et al. (2009) for a complete discussion of compressible energy equation systems.

denoted by the chosen auxiliary turbulence variable; e.g., $\xi \rightarrow \varepsilon$ yields the k-ε model. Here, we examine the standard k-ε model of Launder & Spalding (1974, hereafter LS74), as well as the extended model of Morán-López & Schilling (2013, hereafter MS13); the k-L models of Chiravalle (2006, hereafter C06) and GS11; and the k-ω models of Wilcox (1988, hereafter W88) and Wilcox (2006, hereafter W06). For the k-ε and k-ω models, we also test the effect of three standard compressibility corrections, presented in Sarkar et al. (1989, hereafter S89), Zeman (1990, hereafter Z90), and Wilcox (1992, hereafter W92).

The turbulent stress tensor τ' is defined as

$$\tau'_{ij} = 2\mu_T(S_{ij} - \frac{1}{3}\delta_{ij}S_{kk}) - \frac{2}{3}\delta_{ij}\rho k \tag{3.2.7}$$

with resolved stress rate tensor $\mathbf{S}$ given by

$$S_{ij} = \frac{1}{2}(\frac{\partial u_i}{\partial x_j} + \frac{\partial u_j}{\partial x_i}). \tag{3.2.8}$$

The specific turbulent kinetic energy k is defined as $k \equiv (1/2)\tau'_{kk}$ and requires an additional transport equation. The generic transport equation (Eq. 3.2.5) is applicable to (almost) all models investigated, with source term

$$\Psi_k = P_T - C_D\rho\varepsilon + C_B\rho\sqrt{k}A_i g_i \tag{3.2.9}$$

with the production term $P_T = \tau'_{ij}\partial u_i/\partial x_j$, specific dissipation ε, dissipation coefficient C_D, buoyancy coefficient C_B, and Atwood number in the ith direction A_i with acceleration $g_i = -(1/\rho)\partial P/\partial x_i$. The source term on the energy equation is $\Psi_E = -\Psi_k$. Table 3.1 presents a summary of all model constants and values.

In adiabatic simulations, the turbulent heat flux vector $\mathbf{q}'$ is defined as

$$q'_j = -\kappa_T\frac{\partial T}{\partial x_j} = \frac{\gamma}{\gamma - 1}\frac{\mu_T}{Pr_T}\frac{\partial T}{\partial x_j} \tag{3.2.10}$$

Table 3.1: Summary of model constants. Some values may appear at variance with the reference; this is due only to our generic formalism, which redefines and combines certain constants for consistency across all models. Values presented for the W06 model neglect limiting functions and should therefore be considered approximations.

Constant	Description	LS74	MS13	C06	GS11	W88	W06
C_μ	Turbulent viscosity	0.09	0.09	0.30	1.00	1.00	1.00
C_D	Dissipation of turbulence	1.00	1.00	8.91	3.54	0.09	0.09
C_B	Buoyancy effects	0.00	0.10	1.70	1.19	0.00	0.00
Pr_T	Turbulent Prandtl number	0.90	0.90	1.00	1.00	0.90	0.89
σ_k	Turbulent energy diffusion	1.00	0.50	1.00	1.00	2.00	1.67
σ_ξ	Turbulent diffusion	1.30	0.50	1.00	0.50	2.00	2.00
σ_C	Turbulent Schmidt number	1.00	0.50	1.00	1.00	1.00	1.00
C_1	Turbulence generation	1.44	1.44	1.00	0.33	0.56	0.52
C_2	Additional effects	1.92	1.92	1.00	1.00	0.08	0.07
C_3	Buoyancy effects	0.00	0.09	0.00	0.00	0.00	0.00

with turbulent thermal conductivity $\kappa_T = c_p \mu_T / Pr_T$, specific heat capacity $c_p = \gamma/(\gamma - 1)$, and turbulent Prandtl number Pr_T.

Passively advected scalar fields are diffused using a gradient-diffusion approximation, where the turbulent diffusive flux vector $\mathbf{d}'$ is given by

$$d'_j = \frac{\mu_T}{\sigma_C} \frac{\partial C}{\partial x_j}, \tag{3.2.11}$$

with Schmidt number σ_C generally of order unity.

3.2.1 k-ε models

In the k-ε formalism, the auxiliary turbulence variable ξ is defined to be the specific turbulent energy dissipation $\varepsilon \propto k^{3/2} L^{-1}$, where L is a defined turbulent length scale. The exact scaling depends on the implementation; we here use $\varepsilon = C_\mu^{3/4} k^{3/2} L^{-1}$, where C_μ is a model constant related to the viscosity.

LS74

LS74 outlined the standard version of the k-ε model, and it is perhaps the most widely used RANS turbulence model. The model uses the eddy-viscosity μ_T defined as

$$\mu_T = C_\mu \rho \frac{k^2}{\varepsilon} \tag{3.2.12}$$

with $C_\mu = 0.09$. The transport equation for ε (Eq. 3.2.6) has the source term

$$\Psi_\varepsilon = C_1 \frac{\varepsilon}{k} P_T - C_2 \rho \frac{\varepsilon^2}{k}. \tag{3.2.13}$$

The model constants are summarized in Table 3.1. Because $C_B = 0$, the model neglects buoyant effects, such as the RT instability.

MS13

To include the RT and RM instability effects in the k-ε model, MS13 added a buoyancy term, with the Atwood number in Eq. 3.2.9 defined as

$$A_i = \frac{k^{3/2}}{\rho\varepsilon}\left(\frac{\partial \rho}{\partial x_i} - \frac{\rho}{P}\frac{\partial P}{\partial x_i}\right). \tag{3.2.14}$$

The source term for the dissipation equation Ψ_ε is also extended as

$$\Psi_\varepsilon = C_1 \frac{\varepsilon}{k} P_T - C_2 \rho \frac{\varepsilon^2}{k} + C_3 \rho \frac{\varepsilon}{\sqrt{k}} A_i g_i. \tag{3.2.15}$$

The model constants are summarized in Table 3.1; we note that the MS13 values are largely the same as LS74 but with modified transport coefficients and $C_B \neq 0$.

3.2.2 k-L models

The k-L model is a two-equation RANS model developed by DT06 to study RT and RM instabilities. Shear (KH instability) was added by C06 and extended to include compressibility effects by GS11. The auxiliary variable ξ is defined to be the eddy length scale L. The model uses the eddy-viscosity

$$\mu_T = C_\mu \rho L \sqrt{2k}. \tag{3.2.16}$$

The transport equation for L (Eq. 3.2.6) has the source term

$$\Psi_L = C_1 \rho L (\nabla \cdot \mathbf{u}) + C_2 \rho \sqrt{2k}. \tag{3.2.17}$$

Again, we here set the specific dissipation in Eq. 3.2.9 to be $\varepsilon = C_\mu^{3/4} k^{3/2} L^{-1}$.

C06

C06 added shear to the k-L model of DT06 by employing the full stress tensor rather than just the turbulent pressure term. This necessitated re-calibrating the model coefficients of DT06. We note that C06 used a slightly different RT growth rate parameter ($\alpha = 0.05$ instead of $\alpha = 0.0625$ in DT06) when calibrating the model. Buoyancy effects are included via the Atwood number defined as

$$A_i = \frac{\rho_+ - \rho_-}{\rho_+ + \rho_-} + \frac{L}{\rho} \frac{\partial \rho}{\partial x_i}, \tag{3.2.18}$$

where ρ_+ and ρ_- are the reconstructed density values at the right and left cell faces, respectively. The model constants are summarized in Table 3.1; we note that the constant values appear to differ from those given in C06, but that this is solely due to our generic two-equation framework which combines and re-defines certain constants.

GS11

Similar to C06, the model of GS11 is based on the k-L model of DT06, but with the complete turbulent stress tensor to include KH effects. The model uses a slightly different definition of the Atwood number from C06, with

$$A_i = \frac{\rho_+ - \rho_-}{\rho_+ + \rho_-} + \frac{2L}{\rho + L\left|\partial\rho/\partial x_i\right|}\frac{\partial\rho}{\partial x_i}, \tag{3.2.19}$$

where again ρ_+ and ρ_- are the reconstructed density values at the right and left cell faces, respectively.

GS11 also introduces a variable ($\tau_{\rm KH}$) to account for compressibility effects by modifying the turbulent stress tensor,

$$\tau'_{ij} = 2\mu_T\tau_{\rm KH}(S_{ij} - \frac{1}{3}\delta_{ij}S_{kk}) - \frac{2}{3}\delta_{ij}\rho k. \tag{3.2.20}$$

$\tau_{\rm KH}$ is calibrated with compressible shear layer simulations and estimated using a "local" Mach number $M_l \equiv |\nabla \times \mathbf{u}|\, L/c_s$, where c_s is the local sound speed. However, the piecewise fit for $\tau_{\rm KH}$ given by Eq. 19 in GS11 is discontinuous, which can lead to numerical issues. We therefore fit their formulation with a smooth function,

$$\tau_{\rm KH}(M_l) = 0.000575 + \frac{0.19425}{1.0 + 0.000337\exp(17.791\ M_l)}. \tag{3.2.21}$$

The model constants are summarized in Table 3.1; we note that the C06 and GS11 model constants differ despite significant similarity in model formulation and calibration.

3.2.3 k-ω models

The k-ω model was first developed by W88 and updated in Wilcox (1998) and W06. The auxiliary variable ξ is defined to be the specific dissipation rate (or eddy frequency) $\omega = k^{1/2}L^{-1}$, which has units of inverse time. Then the specific dissipation is $\varepsilon = C_\mu k\omega$. To

our knowledge, this is the first use of a k-ω model in an astrophysical application.

W88

The first version of the k-ω model is outlined in W88. The model uses the eddy-viscosity

$$\mu_T = C_\mu \frac{\rho k}{\omega}. \tag{3.2.22}$$

The transport equation for ω (Eq. 3.2.6) uses the source term

$$\Psi_\omega = C_1 \frac{\omega}{k} P_T - C_2 \rho \omega^2. \tag{3.2.23}$$

The model constants are summarized in Table 3.1.

W06

The most recent version of the k-ω model is presented in W06 and Wilcox (2008). While the model is similar to W88, there are important (and elaborate) differences, such as cross-diffusion terms and stress limiters. While the additional terms improve the accuracy and reduce the dependence on initial conditions, the model is sufficiently complex to prohibit a generic description. Our implementation in Athena includes the additional terms, and we refer the reader to W06 and Wilcox (2008) for a full description of the model. For completeness we note approximate constant values in Table 3.1.

3.2.4 Compressibility corrections

A common way to account for compressibility effects is to modify the turbulence dissipation rate ε. In theory, ε is decomposed into solenoidal and dilatational components, with the latter only manifesting in compressible turbulence. In practice, only a slight modification is needed to the k and ω equations. In Eq. 3.2.9, the second term on the right hand side is modified as $C_D \rho \varepsilon \rightarrow C_D \rho \varepsilon [1 + F(M_t)]$, where $F(M_t)$ is a function of the local

turbulent Mach number $M_t \equiv \sqrt{2k}/a_s$, with a_s the local sound speed. No further changes are needed in the k-ϵ formalism. In the k-ω formalism, Eq. 3.2.23 is also modified with $C_2\rho\omega^2 \rightarrow [C_2 - C_D F(M_t)]\rho\omega^2$. We consider three forms for $F(M_t)$ proposed in the literature. The simplest model is that of S89 which uses

$$F(M_t) = M_t^2. \tag{3.2.24}$$

The most complex model is that of Z90 with

$$F(M_t) = 0.75\{1.0 - \exp[-1.39(\gamma + 1.0)(M_t - M_{t0})^2]\}\mathcal{H}(M_t - M_{t0}), \tag{3.2.25}$$

with $\mathcal{H}$ the Heaviside step function and $M_{t0} \equiv 0.10\sqrt{2/(\gamma + 1)}$. Finally, the model of W92 suggests

$$F(M_t) = 1.5(M_t^2 - 0.0625)\mathcal{H}(M_t - 0.25). \tag{3.2.26}$$

It is worth noting that these are purely phenomenological models; resolved DNS simulations by (Vreman et al., 1996) have demonstrated that the dissipation is not actually reduced in compressible turbulence. Despite this realization, compressibility corrections that modify the dissipation are still commonly used because they yield accurate results in many applications. As noted in Section 3.2.2, GS11 uses a different type of compressibility correction which modifies the turbulent stress tensor. No satisfactory correction is available for C06.

3.2.5 Turbulence model initial conditions

In simulations with a turbulence model, we must specify initial conditions for the turbulent kinetic energy k and the additional turbulent variable ($\xi \rightarrow \varepsilon$, L, or ω). We desire identical initial conditions for all models; we therefore set the turbulent length scale L in all models and convert using scaling relations. Based on dimensional arguments, $\varepsilon \propto k^{3/2}/L$ and $\omega \propto k^{1/2}/L$. The literature values for the constant of proportionality vary; we obtained

Table 3.2: Mixing layer growth rates for $M_c = 0.10$.

Model	C_{b10}	C_{b1}	C_{s10}	C_ω	C_θ
empirical	0.082-0.100 [a]	0.170-0.181 [b]	0.058-0.084 [a]	0.081-0.091 [a,c]	0.016-0.018 [d]
LS74	0.070	0.092	0.056	0.083	0.015
MS13	0.067	0.091	0.053	0.077	0.014
C06	0.181	0.206	0.143	0.066	0.038
GS11	0.123	0.189	0.100	0.134	0.026
W88	0.052	0.062	0.041	0.040	0.011
W06	0.061	0.074	0.047	0.069	0.013

[a]Barone et al. (2006); [b]Papamoschou & Roshko (1988), with $\delta_{viz} \approx \delta_{b1}$; [c]Brown & Roshko (1974); [d]Pantano & Sarkar (2002).

the best agreement across models using $\varepsilon_0 = C_\mu^{3/4} k_0^{3/2} L_0^{-1}$ and $\omega_0 = C_\mu^{-1/4} k_0^{1/2} L_0^{-1}$.

3.2.6 Implementation in Athena

The turbulence update is first order in time and implemented via operator splitting. The fluxes are calculated at cell walls using a simple average to reconstruct quantities from cell-centered values. Spatial derivatives are computed using second order central differences. Source terms are evaluated after application of the viscous fluxes and are applied with an adaptive Runge-Kutta-Fehlberg integrator (RKF45). Stability of the explicit diffusion method is preserved by limiting the overall hydrodynamic time step based on the condition $\Delta t \leq (\Delta^2 \rho)/(6\mu_T)$, where Δ is the minimum cell size. The dependence on Δ^2 limits the feasibility of our implementation to low resolution simulations.

3.3 Mixing layer test

To verify the implementation of each turbulence model in Athena, we perform a one-dimensional temporal mixing layer test. Our set-up is nearly identical to that described in section 2.2.2 of GS11, which was adapted from section 3 of C06. We initialize a discontinuity in the perpendicular (y) velocity at the origin. The difference in velocity between the left and

right states sets the convective Mach number, defined as (Papamoschou & Roshko, 1988)

$$M_c \equiv \frac{|v_l - v_r|}{c_l + c_r}, \tag{3.3.1}$$

with v the y-velocity and c the sound speed, with subscripts l and r for the left and right regions respectively. Unlike GS11, we shift the frame of reference to move at the convective velocity; then $v_l = -v_r$. We also smooth the initial velocity discontinuity with a hyperbolic tangent function, as was done in Palotti et al. (2008). The parallel (x) velocity is zero. We use an ideal equation of state with $\gamma = 1.4$. The density and pressure are constant at $\rho_0 = 1.0\,\mathrm{g\,cm^{-3}}$ and $P_0 = 1.72 \times 10^{10}\,\mathrm{erg\,cm^{-3}}$, corresponding to a uniform sound speed $c_l = c_r = 1.55 \times 10^5\,\mathrm{cm\,s^{-1}}$. The simulation domain is a one-dimensional region with extent -5.0 cm $< x <$ 5.0 cm with a resolution of 4096 cells. Similar to GS11, we initialize a small shear layer of width $\delta_0 = 0.1$ cm centered at the interface with turbulent energy $k = 0.02(\Delta v)^2$ and $L = 0.2\delta_0$, where $\Delta v = |v_l - v_r|$. This initial layer is also smoothed to the background values of $k_0 = 10^{-4}(\Delta v)^2$ and $L_0 = 10^{-2}\delta_0$.

We run each simulation for 200 μs. The velocity discontinuity generates a shear layer, and the width of the shear layer δ grows linearly in time as

$$\delta(t) = C_\delta\ \Delta v\ t, \tag{3.3.2}$$

where C_δ is a constant. The exact value for C_δ depends on how the shear layer thickness δ is defined. In lab experiments, the visual thickness δ_{viz} (Brown & Roshko, 1974) or pressure thickness δ_p (Papamoschou & Roshko, 1988) are used. In numerical experiments, the velocity thickness δ_b, energy thickness δ_s, and vorticity thickness δ_ω are often used (Barone et al., 2006); less common is the momentum thickness, δ_θ (Vreman et al., 1996). C06 and GS11 used a 1 per cent threshold on the velocity thickness (which we will denote as δ_{b1}), considering regions where $0.01 < (v - v_l)/(\Delta v) < 0.99$; engineering literature tends to use a 10 per cent threshold (δ_{b10}), defined similarly to δ_{b1}. W88 used a 10 per cent energy thickness

(δ_{s10}), defined where $0.1 < (v - v_l)^2/(\Delta v)^2 < 0.9$. We will compare results using these three definitions, as well as the momentum thickness $\delta_\theta = 1/[\rho_0(\Delta v)^2] \int \rho(v_l - v)(v - v_r)\, dx$ and the vorticity thickness $\delta_\omega = |v_l - v_r|/(\partial v/\partial y)_{max}$.

A further complication is that lab experiments of the plane mixing layer measure a spatial spreading rate, $\delta'(x) \equiv d\delta/dx$. In our experiment, we move in a frame of reference at the convective velocity $v_c = (1/2)(v_l + v_r)$ (assuming $c_l = c_r$) and therefore measure a temporal spreading rate, (e.g., Vreman et al., 1996; Pantano & Sarkar, 2002)

$$\delta'(t) = \frac{d\delta}{dt} = \frac{dx}{dt}\frac{d\delta}{dx} = v_c \delta'(x). \tag{3.3.3}$$

Values for C_δ estimated from plane mixing layer experiments (Brown & Roshko, 1974; Papamoschou & Roshko, 1988) and high-resolution numerical simulations (Pantano & Sarkar, 2002; Barone et al., 2006) are reported in Table 3.2, where the subscript on C indicates the corresponding shear layer thickness definition.

3.3.1 Mixing layer results

Figure 3.1 shows the time evolution of a subsonic ($M_c = 0.1$) mixing layer with the LS74 k-ε model. The profiles of the the y-velocity v, turbulent kinetic energy k, and turbulent length L all spread in time; as noted, the exact spreading rate depends on how the layer thickness is defined. Figure 3.2 shows the growth of the shear layer thickness $\delta(t)$ for different layer definitions. All definitions show linear growth in time. The 1 per cent velocity thickness grows at the greatest rate, while the momentum thickness increases at the lowest rate. We use a χ^2 minimization linear fit to estimate C_δ; the results are presented in Table 3.2.

Table 3.2 also shows the growth rates at $M_c = 0.10$ for all RANS models tested. We find that the various turbulence models lead to differing growth rates on the same test problem. Although most models do not reproduce the measured growth rate for all thickness definitions, all models do produce linear growth in time and roughly agree with the measured value for at least one definition, leading us to conclude that our models are implemented correctly

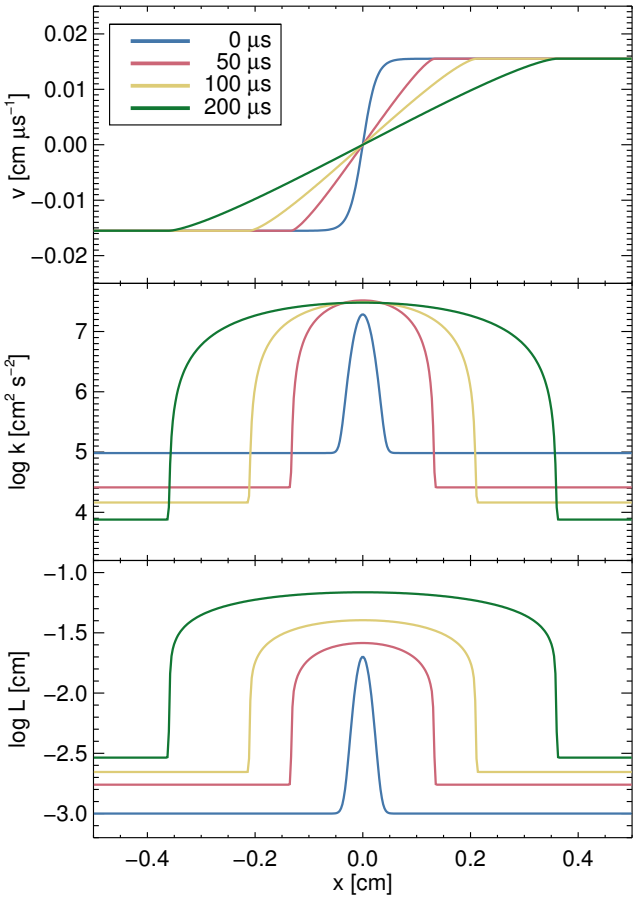

Figure 3.1: Time evolution of the one-dimensional subsonic ($M_c = 0.10$) shear flow test with the LS74 k-ε turbulence model. From the top, profiles of the y-velocity v, specific turbulent kinetic energy k, and turbulent length scale $L = C_\mu^{3/4} k^{3/2} \varepsilon^{-1}$. Profiles are shown at times $t = 0$, 50, 100, and 200 μs, indicated by colour.

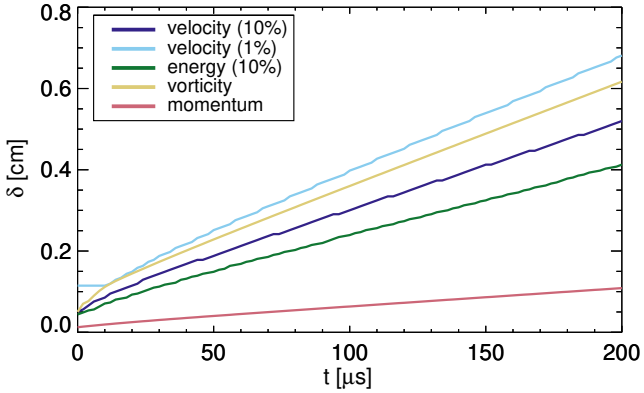

Figure 3.2: Growth of the shear layer width $\delta(t)$ in the subsonic ($M_c = 0.10$) mixing layer with the LS74 k-ε turbulence model. The shear layer definition is indicated by colour. All definitions produce linear growth but at different rates.

in ATHENA. Variations in numerical method between codes could lead to discrepancies with previous work; further, there is significant uncertainty on the measured values. Interestingly, there is no clear relation between the different measures and models; for example, C_{b10} is much greater with the GS11 model compared to the LS74 model, but C_ω is slightly less. This suggests no single measure should be preferred.

Finally, we note that C06 and GS11 calibrated their turbulence models using a 1 per cent velocity definition for the mixing layer. While their models show good agreement with this definition, we find that these models largely do not predict spreading rates in agreement with measured values when using other definitions. This suggests that a 1 per cent criterion may not be the best definition for comparison.

3.3.2 Compressible mixing layer

The spreading rate of a compressible mixing layer is found to decrease with increasing convective Mach number (Birch & Eggers, 1973; Brown & Roshko, 1974; Papamoschou & Roshko, 1988). The difference is expressed as the compressibility factor $\Phi \equiv \delta'/\delta'_i$, where δ'_i is the incompressible growth rate. Experiments have yielded different relations between M_c and Φ, such as the popular "Langley" curve (Birch & Eggers, 1973), the results of Papamoschou & Roshko (1988), and the fit of Dimotakis (1991).

We perform simulations with increasing convective Mach number up to $M_c = 10$. We use the growth rate determined at $M_c = 0.1$ with thickness δ_{b10} as our incompressible growth rate δ'_i. Results obtained with the LS74 model are presented as solid circles in Figure 3.3, with two experimental curves shown for comparison. Although the spreading rate does decrease with increasing Mach number, it does not follow the experimental trend. This is consistent with previous work which shows that standard two-equation RANS turbulence models do not reproduce the observed reduction in spreading rate without modifications.

As described in Section 3.2.4, three authors (S89, Z90, and W92) have proposed "compressibility corrections" to better capture the decrease. These corrections work by increasing

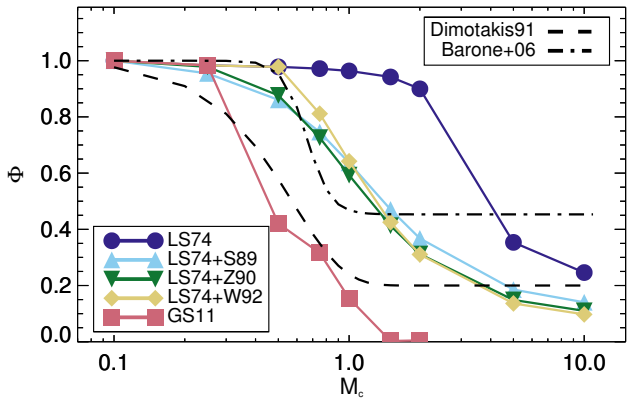

Figure 3.3: The compressibility factor $\Phi \equiv \delta'/\delta'_i$ as a function of convective Mach number M_c. Results are shown for the standard LS74 model with no compressibility correction (purple dots) and with the compressibility corrections of S89 (blue upward triangles), Z90 (green downward triangles), and W92 (gold diamonds); as well as for the GS11 model (red squares), which includes a stress modification (τ_{KH}). The empirical curves of Dimotakis (1991, dashed) and Barone et al. (2006, dot-dashed) are also shown for comparison.

the dissipation rate due to pressure-dilatation effects. Although direct numerical simulation results have shown that this is not actually the case (Vreman et al., 1996), these *ad hoc* compressibility corrections are still widely used because they produce more accurate results (at least in the transonic regime). Figure 3.3 also shows results obtained when the three compressibility corrections are applied to the LS74 model. All three corrections do decrease the spreading rate to roughly the experimental values, at least up to $M_c = 5$; above this, the growth rate is slightly below the experimental estimate. The difference between the corrections of S89, Z90, and W92 is negligible. Similar results are obtained when applied to the MS13, W88, and W06 models.

There is no straightforward way to apply these corrections to the model of C06; however, GS11 does include a compressibility correction through the variable τ_{KH} (see Section 3.2.2). Results obtained with the model of GS11 are also shown on Figure 3.3. The asymptotic nature of the τ_{KH} function (Eq. 3.2.21) reproduces the observed behavior of compressible layers up to $M_c \approx 1$; however, above this point the GS11 formulation leads to growth rates that are too small. Indeed, data points are not available for $M_c > 2.5$ for GS11 because the model did not evolve.

3.4 Stratified medium test

Three of the models here considered include buoyant effects to capture the RT instability, namely MS13, C06, and GS11. To further verify the implementation of these models, we perform a two-dimensional stratified medium test. Our set-up is nearly identical to that described in section 2.2.1 of GS11, which was itself adapted from section 5 of DT06. We accelerate a heavy fluid of density $\rho_1 = 1.0$ g cm^{-3} into a lighter fluid of density $\rho_2 = 0.9$ g cm^{-3} from an initially hydrostatic state. The acceleration acts in the $-y$ direction at $g = 9.8 \times 10^8$ cm s^{-2}. The grid is 0.02×1.0 cm with a resolution of 16×800 cells, and the interface is at the midpoint of the y axis. The temperature is discontinuous at the interface, with $T_1 = 45$ K and $T_2 = 50$ K, and follows a profile to maintain hydrostatic equilibrium. Note that we do not perturb the interface; as the interface is grid-aligned, the RT instability will not develop in an inviscid code. However, a buoyant turbulence model will recognize the impulsive density and pressure gradients and generate turbulence, leading to the development of a mixing layer between the two fluids. Bubbles of light fluid will penetrate the heavy fluid with height $h(t) = \alpha_b A g t^2$, where $A = (\rho_1 - \rho_2)/(\rho_1 + \rho_2)$ is the Atwood number and $\alpha_b \approx 0.06$ is a constant empirically determined from experiments (Dimonte et al., 2004). Numerical simulations of the RT instability tend to underestimate the growth by a factor of ~ 2 (Dimonte et al., 2004; Stone & Gardiner, 2007), underscoring the need for a turbulence model.

Figure 3.4 shows the evolution of the boundary layer for the turbulence models of C06, GS11, and MS13. The other turbulence models (LS74, W88, and W06) lack buoyant source terms; hence they cannot capture the RT instability and show no evolution in this test case. We compare the growth of turbulent kinetic energy $k(y,t)$ and turbulent length scale $L(y,t)$ with the analytic solutions given in DT06. The model of GS11 shows good agreement with the analytic predictions; however, the models of C06 and MS13 do not accurately follow the evolution. We note that C06 used a slightly lower value of the bubble penetration constant α_b compared to DT06 when calibrating the model; however this is insufficient to fully explain

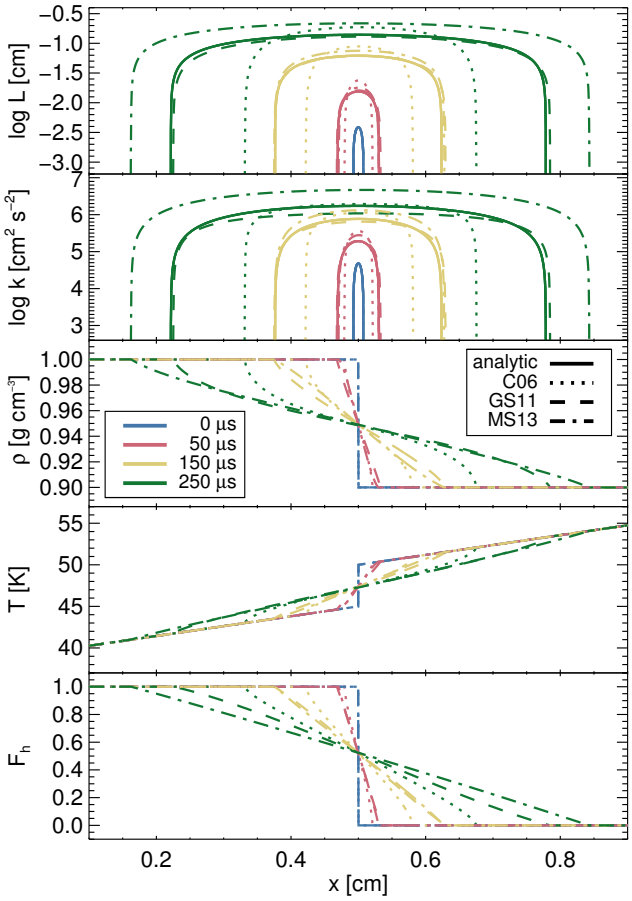

Figure 3.4: Time evolution of the stratified medium test with the buoyant turbulence models (dotted: C06; dashed: GS11; dot-dashed: MS13). From the top, profiles of the turbulent length scale L, specific turbulent kinetic energy k, density ρ, temperature T, and heavy-fluid mass fraction F_h. Profiles are shown at times $t = 50$, 100, 200, and 300 μs, indicated by colour. Analytic solutions are shown for L and k with solid lines. While GS11 matches well, C06 grows too slowly and MS13 too quickly.

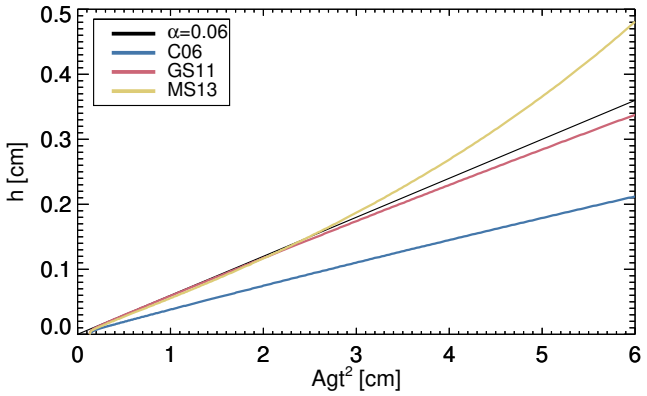

Figure 3.5: Growth of the bubble height h as a function of Agt^2 for the buoyant turbulence models (C06, GS11, and MS13). The growth should be linear with slope equal to the DT06 experimental bubble constant $\alpha = 0.06$, shown in black. GS11 matches well with linear growth at $\alpha \approx 0.05$. C06 is also linear but with a lower value of $\alpha \approx 0.038$. MS13 matches well initially with $\alpha \approx 0.06$, but eventually the evolution becomes non-linear and diverges.

the discrepancy. Figure 3.4 also shows the evolution of the density ρ, the temperature T, and the heavy fluid mass fraction F_{h}, determined using a passive color field C that is initialized to unity in the heavy fluid and to zero in the light fluid.

We can also determine the growth rate of the bubble height $h(t)$, estimated as the point where the mass fraction of heavy material $F_{\mathrm{h}} = 0.985$ (Stone & Gardiner, 2007). Figure 3.5 shows the growth of the bubble height $h(t)$ plotted against Agt^2; hence the lines should be linear with a slope of $\alpha \approx 0.06$. We see that, after an initial transient phase, the GS11 model does show a linear trend with $\alpha \approx 0.050$ – slightly lower than expected but still in good agreement. The model of C06 also shows a linear trend, but the layer grows too slowly with $\alpha \approx 0.038$. The MS13 model is initially in good agreement with $\alpha \approx 0.060$ but eventually diverges and grows non-linearly. It is unclear what in the MS13 model causes this runaway growth, but the test result suggests that MS13 may not properly account for sustained buoyancy and will therefore yield inconsistent results.

3.5 Shock-cloud simulations

Having verified and validated our turbulence model implementation with idealized tests, we now explore a complex problem: the astrophysical shock-cloud interaction. We solve Eqs. 3.2.1-3.2.6 in Athena using the directionally unsplit CTU integrator (Colella, 1990) with third order reconstruction in the characteristic variables (Colella & Woodward, 1984) and the HLLC Riemann solver (Toro, 2009). Simulations are performed on Cartesian grids in three dimensions. We use an adiabatic equation of state with the ratio of specific heats $\gamma = C_{\rm p}/C_{\rm V} = 5/3$. Self-gravity and magnetic fields are not included.

3.5.1 Setup and initial conditions

Our simulation is a variant of the typical shock-cloud interaction: a planar shock wave of hot diffuse gas propagates through a uniform medium and impacts a cold, dense cloud. The initial conditions are determined by the Mach number of the shock M, the radius of the cloud R, and the density ratio of cloud to the ambient medium χ. Our fiducial simulation uses $M = 10$, $R = 1$, and $\chi = 10$.

The ambient medium is initially uniform with density $\rho_0 = 1$ and pressure $P_0 = 1$, in arbitrary (computational) units. Our simulation domain initially extends from $-5 \leq x \leq 15$, $-5 \leq y \leq 5$, and $-5 \leq z \leq 5$, again in arbitrary units. All boundaries are outflow-only, except the upstream boundary (see below). The simulation resolution is indicated by the number of cells per cloud radius $N_{\rm R}$; our fiducial simulation is $N_{\rm R} = 25$, corresponding to a resolution of $512 \times 256 \times 256$. We perform a resolution test in Section 3.5.2 up to $N_{\rm R} = 200$; while $N_{\rm R} = 25$ is sufficient for most quantitative estimates, the details of the mixing are notably different for $N_R \geq 100$.

The cloud begins centered at the origin and in pressure equilibrium with the ambient medium. The cloud has a spherically-symmetric density profile given by (e.g., Nakamura

et al., 2006):

$$\rho(r) = \rho_0 + \frac{\rho_c - \rho_0}{1 + (\frac{r}{R})^n}, \tag{3.5.1}$$

where $\rho_c = \chi\,\rho_0$ is the central density and n controls the steepness of the profile. We use $n = 20$ to obtain a profile similar to that of P09 but steeper than that of SSS08 (which used $n = 8$). As in SSS08, we must set an arbitrary boundary for the "cloud," which we denote as r_b and define where $\rho(r_b) = 1.01\rho_0$; for $R = 1$ and $n = 20$, $r_b = 1.25$. To trace cloud material, a passive scalar field C_c is set to unity where $r \leq r_b$ and zero otherwise.

We initialize the shock with the adiabatic solutions of the Rankine-Hugoniot jump conditions for a given Mach number M. The upstream boundary condition maintains these quantities, resulting in a shocked wind model. The shock begins at $x = -2$ and propagates in the $+x$ direction. We use an additional passive colour field to trace the mixing of shocked material in the simulation. A shock tracer C_s is initialized to unity only within the leading edge of the shock with a width of one cloud radius, i.e., $C_s = 1.0$ where $-3 < x < -2$ and zero otherwise.

The time is given in terms of the "cloud crushing time", t_{cc}, defined as (Klein et al., 1994)

$$t_{cc} \equiv \frac{R}{u_s} = \frac{\chi^{1/2} R}{M a_s}, \tag{3.5.2}$$

where u_s is the shock velocity within the cloud and $a_s = \sqrt{\gamma P_0/\rho_0} = \sqrt{5/3}$ is the ambient sound speed in computational units.

We do not use any mesh refinement – simulations are run on a single mesh of uniform spacing. Athena is capable of static mesh refinement (SMR), which differs from adaptive mesh refinement (AMR) in that in SMR the refinement grids are placed at the beginning of the simulation and remain fixed. We did attempt to use SMR but encountered significant issues when combined with a turbulence model. Interpolation of the conserved variables (namely energy and momentum) across coarse-fine interfaces produced small numerical errors in the primitive variables (namely pressure and velocity), which were sufficient to generate

artificial vorticity that was amplified by the turbulence models. Using a single grid has the further advantage that the diffusive properties of the code remain uniform across the domain.

Turbulence model initial conditions

Following GS11, we set the initial value for k relative to the internal energy as $k_0 = k_i\, e_{\rm int}$ on a cell by cell basis with $e_{\rm int} = P/(\gamma - 1)$; similarly, we set the initial value for L relative to the cloud radius as $L_0 = L_i\, R$. For our fiducial simulation, we choose $k_i = 10^{-2}$ and $L_i = 10^{-2}$ everywhere to roughly match the initial conditions of GS11. We note that this differs from the approach of P09 in which the authors used different initial conditions for the shock and cloud; the effect of initial conditions will be explored in Section 3.5.2.

Co-moving grid

The cloud will be accelerated and disrupted by the shocked wind, and eventually all cloud material will leave the initial simulation domain. To follow the cloud evolution for as long as possible, we implement a "co-moving grid" similar to the method used in SSS08. We adjust the x-velocity at each time step to keep our domain centered on the bulk of the cloud material. At the beginning of each integration, we compute the mass-averaged cloud velocity

$$\langle v_x \rangle = \frac{\int_V (\rho C_c)^g\, v_x\, dV}{\int_V (\rho C_c)^g\, dV}, \tag{3.5.3}$$

where g is a weighting factor we introduce to keep the grid fixed on the densest cloud material. While SSS08 used $g = 1$, we find we are better able to follow the cloud with $g = 4$. We then subtract $\langle v_x \rangle$ from the x-velocity everywhere in the simulation and update the grid location and inflow conditions accordingly. To prevent cloud material from encroaching on the upstream boundary, we limit the co-moving velocity when cloud material would come within a distance of $2r_b$ from the upstream boundary. We also prohibit the inflow velocity from becoming subsonic to prevent information traveling upstream. We have verified this method by comparing to simulations performed in an elongated static grid ($-5 < x < 45$);

the resulting cloud evolution is nearly indistinguishable.

Implicit Large Eddy Simulations

Grid-based hydrodynamics simulations performed without a turbulence model are sometimes referred to as "inviscid" simulations; however, the discretization of the Euler equations introduces numerical viscosity, and the turbulent cascade is truncated at the grid scale. The grid thus serves as an "implicit" filter, and such a simulation may be referred to as an "Implicit Large-Eddy Simulation", or ILES (Garnier et al., 2009; Schmidt, 2014). We therefore denote simulations performed without a turbulence model as ILES. We perform high-resolution ILES simulations up to $N_{\rm R} = 200$ for comparison to simulations with a turbulence model.

Ensemble-averaged simulations with grid-scale turbulence

Even at high resolution, an ILES simulation with static initial conditions is not equivalent to models with a turbulence model because the turbulence models are initialized with non-zero small-scale turbulent energy ($k_0 \neq 0$). P09 therefore compared shock-cloud simulations performed with the LS74 k-ε model to an inviscid simulation with random perturbations to the density, velocity, and pressure in the post-shock flow. We extend the P09 approach by averaging multiple high-resolution inviscid simulations initialized with different random perturbations. This should provide a good comparison, as the results from a RANS turbulence model can be interpreted as an ensemble average over many turbulent flow realizations. The velocity perturbations are drawn from a Gaussian distribution, and the width of the Gaussian is set to match the initial level of turbulence in the models, namely $k_i = 10^{-2}\, e_{\rm int}$. The amplitude of the density perturbations is drawn from a Gaussian with a width of 0.01. Note that, unlike P09, we do not perturb the pressure. We perform 10 simulations at $N_R = 25$ with different turbulent realizations and then average on a cell-by-cell basis. We refer to results from this method as "Turbulent ILES", or TILES.

Diagnostics

For comparison to previous shock-cloud simulations, we compute several standard integrated diagnostic quantities (Klein et al., 1994). The cloud-mass-weighted average of a quantity f is defined as

$$\langle f \rangle = \frac{1}{M_{cl}} \int_V \rho C_c f dV, \tag{3.5.4}$$

where the initial cloud mass $M_{cl} = \int_{t=0} (\rho C_c)\, dV$.

We follow the effective radius normal to the x-axis

$$a = [5(\langle x^2 \rangle - \langle x \rangle^2)]^{1/2}, \tag{3.5.5}$$

with similar expressions along the y and z axes denoted b and c respectively. We also compute the rms velocity along each axis (Nakamura et al., 2006),

$$\delta v_x = (\langle v_x^2 \rangle - \langle v_x \rangle^2)^{1/2}, \tag{3.5.6}$$

again with similar expressions in y and z.

To follow the mixing, we adopt the mixing fraction $f_{\rm mix}$ introduced in Xu & Stone (1995) and used in SSS08, where

$$f_{\rm mix} = \frac{1}{M_{cl}} \int_{0.1<C_c<0.9} \rho C_c dV. \tag{3.5.7}$$

As the cloud material (initially $C_c = 1.0$) is mixed into the ambient medium (initially $C_c = 0.0$), the cloud concentration will take on intermediate values and $f_{\rm mix}$ will increase.

We also examine another quantitative estimate of the mixing: the injection efficiency $f_{\rm inj}$, defined as

$$f_{\rm inj} = \frac{1}{\eta_{\rm geom} M_s} \int_{C_c \geq 0.1} \rho C_s dV, \tag{3.5.8}$$

where $M_s = \int_{t=0} \rho C_s dV$ is the initial shock tracer mass and η is a normalization factor. As the shock passes over the cloud, mixing at the leading edge by RT instabilities and at the

edges by KH instabilities will "inject" shock material (such as SLRs) into the cloud. As in 4.3.3, the injection efficiency is normalized via $\eta_{\rm geom}$ such that only the mass of the shock tracer directly incident on the cloud cross-section πr_b^2 is considered; hence, $f_{\rm inj} = 1$ indicates "perfect" injection.

Optimization and Performance

The shock-cloud simulations were performed on the KillDevil Cluster at UNC Research Computing. To our knowledge, the run with $N_R = 200$ is the largest fixed-grid simulation of the three-dimensional shock-cloud interaction performed to date, with $4096 \times 2048 \times 2048$ grid cells. Evolving the simulation to $t = 10t_{\rm cc}$ required over 500,000 CPU-hours, with a maximum memory usage of nearly 13 TB across 2,048 CPUs.

Due to the fixed-grid nature of Athena, there is very little overhead in our simulations, and communication between processors is largely limited to transmission of boundary values after each update. Athena has been demonstrated to scale well out to 20,000 processors (Stone et al., 2008). We judge performance using the number of cells updated per CPU second. In our shock-cloud simulations, we find that the performance of the code is better for larger jobs, increasing from 2.02×10^4 cells per second at $N_R = 6$ up to 2.10×10^5 at $N_R = 200$. This increase is not surprising, as the ratio of computational work to inter-process communication increases with increasing resolution. In our largest simulation, the processors spent over 99% of their time in active computation, indicating that the load is well-balanced and that inter-process communication over the InfiniBand network did not saturate significantly.

3.5.2 Results

Dynamical evolution

We follow the interaction of the shocked wind with the cloud for up to 10 cloud-crushing times. Figure 3.6 shows the time evolution of the cloud column density $\Sigma(C_c) =$

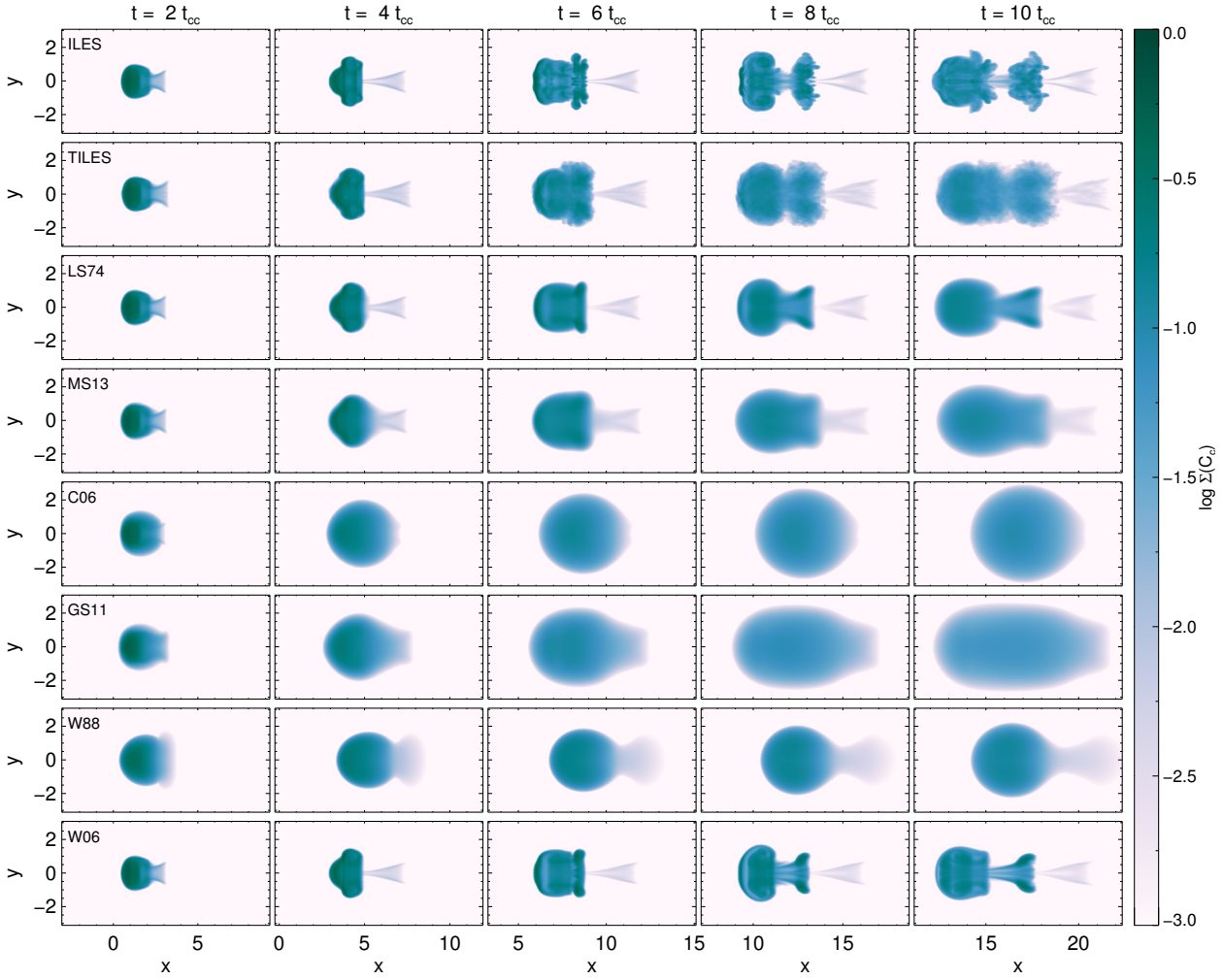

Figure 3.6: Time evolution of the logarithm of the density-weighted cloud column density $\Sigma(C_c) \equiv \int \rho C_c \, dz / \int \rho \, dz$ in the fiducial ($N_{\rm R} = 25$) three-dimensional shock-cloud interaction. The units are arbitrary. From left to right, the columns show snapshots at $t = 2$, 4, 6, 8, and 10 t_{cc}. From top to bottom, the rows show simulations performed with no turbulence model (ILES), ensemble-averaged grid-scale turbulence (TILES), the k-ε models of LS74 and MS13, the k-L models of C06 and GS11, and the k-ω models of W88 and W06. As the cloud is accelerated by the shock, the simulation domain moves to follow the bulk of the cloud material. The cloud is ablated forming a head-tail structure, and the characteristic vortex ring is visible at $t = 4t_{\rm cc}$. The RANS turbulence models smooth the fluctuating structures below a characteristic length scale L, in some cases completely diffusing the cloud.

$\int \rho C_c \, dz / \int \rho \, dz$ in the fiducial ($N_{\rm R} = 25$) simulations for each of the models, including no turbulence model (ILES) and ensemble-averaged grid-scale turbulence (TILES). The cloud material is initially confined within $r \leq r_b$, but after impact material is ablated and mixed into the shock and ambient medium, leading to a head-tail structure. The cloud is accelerated in the $+x$-direction; as described in Section 3.5.1, we shift our grid to be co-moving with the densest cloud material. The location of the cloud at a given time varies from run to run, as each turbulence model uniquely alters the cloud acceleration and destruction. As material is ablated from the edges of the cloud, large KH rolls develop in the ILES simulation. Around 4 t_{cc}, the characteristic vortex ring is clearly evident. The evolution of an inviscid adiabatic shock-cloud interaction is described in detail in PP16; we here focus on the differences resulting from the turbulence models.

The turbulence models also include diffusion of passive colour fields, which is of particular importance for the mixing estimates. In the ILES simulations, cloud material is most concentrated at the cloud edges as a result of the KH instability. The additional viscosity from the turbulence models diffuses the colour field to varying degrees. In the models of LS74, MS13, and W06, three structures still remain in the colour field: the dense head, the vortex ring, and the diffuse tail. However, in the models of C06, GS11, and W88, the colour field is largely smoothed. In C06 and GS11, the cloud material becomes nearly uniformly distributed in an oblate spheroid. It is unclear whether this is due to increased buoyancy, shear effects, and/or over-production of turbulent energy.

Figure 3.7 presents the time evolution of the density-weighted column of specific turbulent energy $\Sigma(k) = \int \rho k \, dz / \int \rho \, dz$. For the ILES and TILES runs, the turbulent energy is not explicitly tracked; we therefore follow Schmidt & Federrath (2011) and construct an estimate for $k = C_k \Delta^2 |S^*|^2$, where Δ is the grid resolution, $S^*_{ij} = S_{ij} - (1/3)\delta_{ij} S_{kk}$ is the trace-free resolved strain rate tensor (see Eq. 3.2.8), and C_k is a scaling constant. The exact scaling is uncertain; Schmidt & Federrath (2011) used $C_k \approx 0.013$ based on supersonic isothermal turbulence. Here, we set $C_k = 1$ and treat k as a morphological rather than

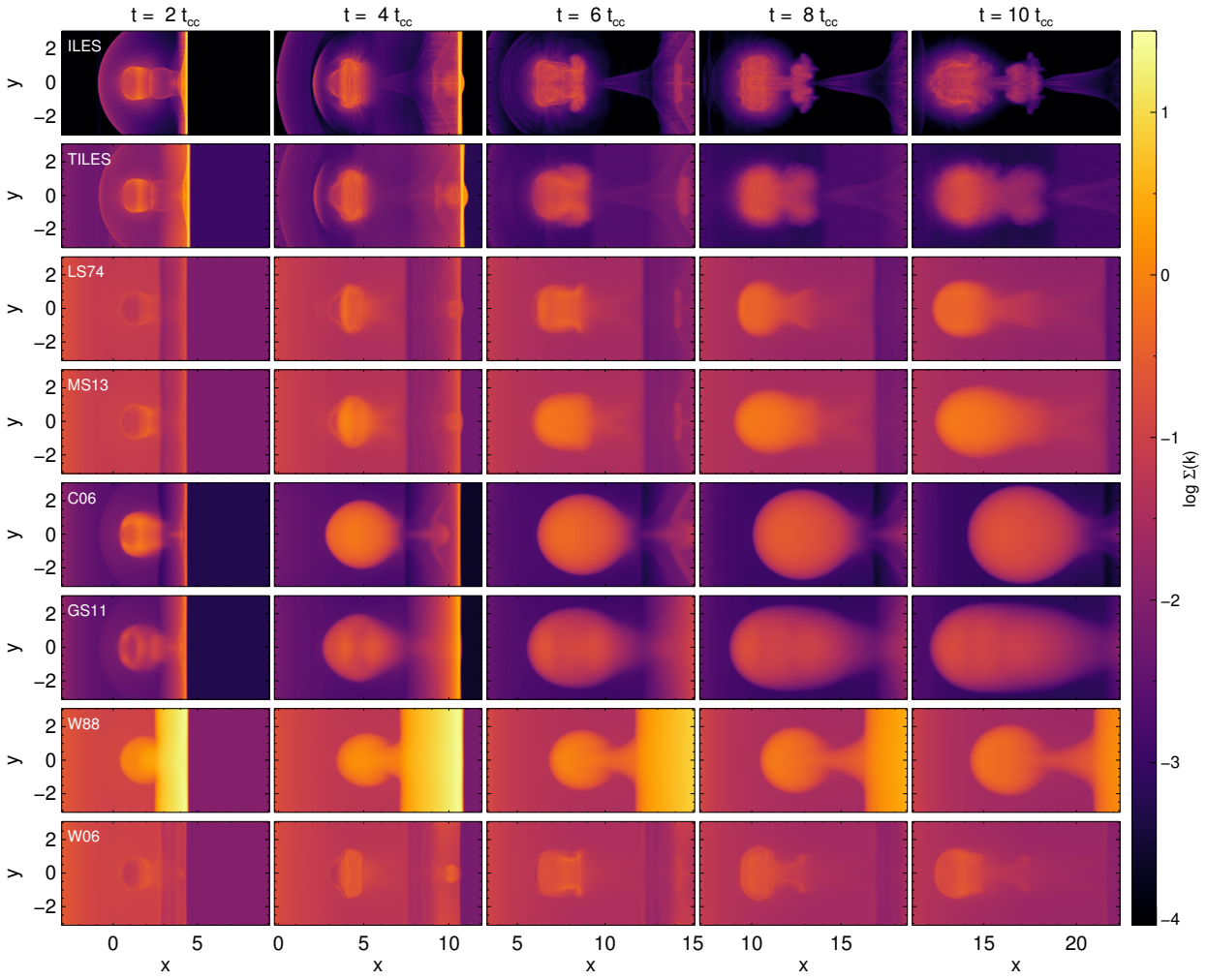

Figure 3.7: Similar to Figure 3.6, but showing the density-weighted column of turbulent kinetic energy $\Sigma(k) \equiv \int \rho k \, dz / \int \rho \, dz$. The units are arbitrary. In runs without a turbulence model (ILES and TILES), k is estimated from the resolved strain-rate tensor.

quantitative estimate.

Figure 3.7 shows that in all runs the strongest areas of turbulence generation are 1) at the cloud edges due to shearing motions; 2) in the cloud tail due to shear and compression; and 3) at the shock front due to compression. LS74 and W06 produce relatively little turbulence, resulting in a correspondingly low turbulent viscosity. These models produce only slight differences in morphology from the ILES and TILES cases. While the small-scale structure is smoothed, the two large KH rolls are still present. In contrast, W88 produces large amounts of turbulent energy, particularly in the shock. The turbulent pressure term ultimately leads to non-physical spreading of the shock downstream. The strong shear at the cloud edges spreads material into two primary streamers. This also occurs in MS13, but the dominant turbulence is at the leading edge of the cloud due to the inclusion of buoyancy effects (RT instability). A similar effect is seen in C06 and GS11 due to the buoyancy; however, in C06 and GS11 the ambient turbulence dissipates rapidly and the cloud expands due to the increased interior turbulent pressure.

The transmitted shock within the cloud also increases the turbulent length scale L via the dilatation term $(\nabla \cdot \mathbf{u})$ in Ψ_L of the k-L models (C06 and GS11); this is seen in Figure 3.8, which shows the evolution of the density-weighted column of L, $\Sigma(L) = \int \rho L \, dz / \int \rho \, dz$. These models show turbulent length scales roughly an order of magnitude greater than the other models, while the turbulent kinetic energy is roughly an order of magnitude lower. The most similar model is MS13; however, all three models with buoyancy terms (MS13, C06, and GS11) show significant expansion, and the cloud is eventually diffused completely. The models without a turbulence model (ILES and TILES) are not shown in Figure 3.8, as L would simply be the grid scale Δ.

Evolution of diagnostic quantities

Figure 3.9 shows the time evolution of various diagnostic quantities. Overall, the turbulence models produce similar results for the cloud axis ratio b/a, excepting C06 and W88.

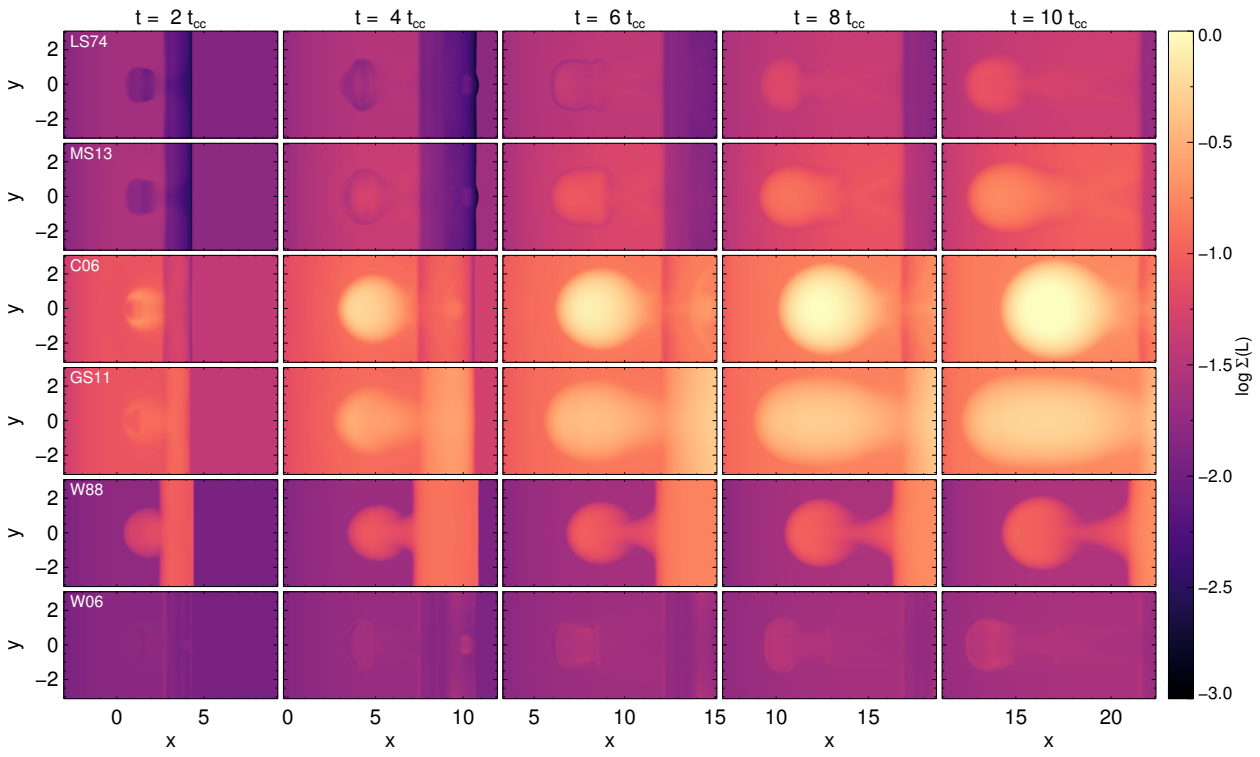

Figure 3.8: Similar to Figure 3.6, but showing the density-weighted column of turbulent length scale $\Sigma(L) \equiv \int \rho L \, dz / \int \rho \, dz$. The units are arbitrary. The runs without a turbulence model (ILES and TILES) are not shown, as $L = \Delta$ by definition.

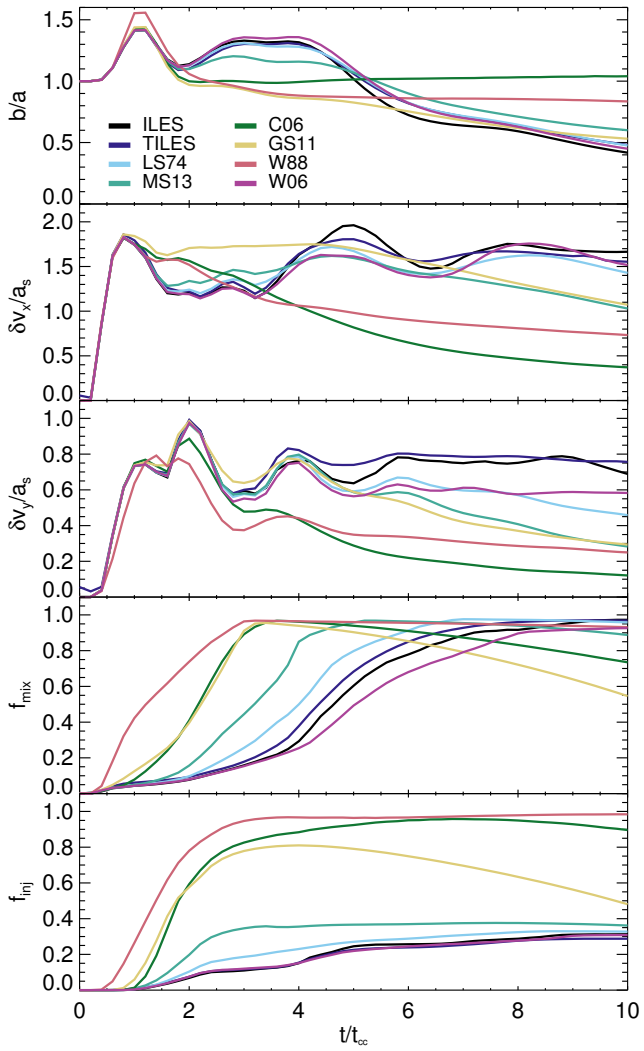

Figure 3.9: Evolution of diagnostic quantities in the three-dimensional shock cloud simulation. From top to bottom, the cloud axis ratio b/a; the rms velocity along the x-axis relative to the sound speed a_s; the rms velocity along the y-axis relative to the sound speed a_s; the mixing fraction $f_{\rm mix}$; and the injection efficiency $f_{\rm inj}$. The turbulence model is indicated by line colour, with the inviscid case shown in black. The units are arbitrary.

In C06, large amounts of turbulent pressure within the cloud cause the cloud to expand and become spherical. However, the turbulence models show little agreement in their treatment of either motions (δv) or mixing ($f_{\rm mix}$ and $f_{\rm inj}$). The ILES and TILES simulations are comparable, but all simulations with a turbulence model show reduced rms velocity dispersions, as the additional turbulent viscosity diffuses the small-scale turbulent motions. Recall that the turbulence models work by averaging out the fluctuating velocities below the characteristic length scale. C06 and GS11 lead to the largest values of L – on the order of the cloud radius within the cloud – and therefore smooth nearly all small-scale fluctuations.

This also affects the mixing. The TILES model shows only slightly faster mixing than the ILES result. This differs from what was observed by P09, where the mixing of material proceeded almost twice as fast in models with grid-scale turbulence compared to those without (see, e.g. fig. 15g of P09, where $m_{\rm core}$ is an alternative measure for mixing). This is mostly likely due to the strength of the imposed turbulence, which was considerably higher in P09 than in our TILES simulations.

As already noted, LS74 and W06 introduce the least turbulent viscosity and therefore most resemble the ILES case. Surprisingly, W06 shows a reduction in $f_{\rm mix}$ relative to the ILES runs. In all runs, $f_{\rm mix}$ approaches unity, indicating complete cloud disruption. In several models, the expansion of the cloud at late times reduces the concentration of cloud colour field below the mixing threshold ($C_c \geq 0.1$) which causes $f_{\rm mix}$ to decrease. A different trend is observed in the injection efficiency, where the three most diffusive models (W88, C06, and GS11) reach a significantly different peak value from the other models. Both the shock and cloud are diffused, and the increased viscosity leads to enhanced injection. There is agreement between most models at a final value of $f_{\rm inj} \approx 0.3$ – slightly higher than previous shock-cloud studies of solar system enrichment, which found $f_{\rm inj} \lesssim 0.1$ (Boss & Keiser, 2015).

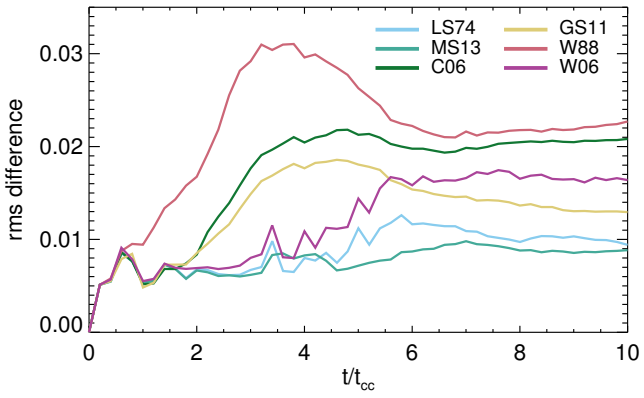

Figure 3.10: Time evolution of the rms difference between the TILES result and the turbulence models for the density-weighted cloud colour field $\Sigma(C_c)$. The turbulence model is indicated by line colour. LS74 and MS13 show the best agreement with the TILES result.

Model validity

A primary goal of this work is to compare the behavior of turbulence models in an identical astrophysical application. Clearly the models do not all reproduce the same dynamical and quantitative evolution. As noted in Section 3.5.1, we believe the best reference for a RANS model is an ensemble-average of high-resolution grid-scale turbulence simulations. We therefore compare the turbulence model results to the TILES result. We compute an rms difference for the density-weighted cloud colour field at each time step using the TILES result as the reference. The time evolution of the rms difference is shown Figure 3.10. We observe that the k-ε models of LS74 and MS13 agree best with the TILES result. A similar trend is observed when compared to the highest resolution ILES simulation ($N_R = 200$, see Section 3.5.2).

Effect of compressibility corrections

As seen in Section 3.3.2, the RANS models here considered are largely calibrated with subsonic, incompressible experiments, and they do not reproduce the correct shear layer growth rate without modifications. As our shock is supersonic ($M = 10$), we anticipated a compressibility correction would be important to model the evolution. However, we find that the compressibility corrections have a negligible effect on the simulation evolution in LS74,

MS13, W88, and W06. We do not test GS11 without $\tau_{\rm KH}$, as this could affect the calibration; and we do not test C06, as there is no straightforward way to implement a correction. As the results are nearly indistinguishable, we do not present any figures. It is possible that the effects may become important at higher Mach numbers, but we defer this for future studies.

Dependence on initial conditions

The RANS turbulence models considered here are known to be sensitive to initial conditions, particularly the W88 model (Wilcox, 2008). In most astrophysical applications, the prescription for the initial values of k and L is arbitrary. We set the initial value for k relative to the internal energy as $k_0 = k_i\, e_{\rm int}$ and for L relative to the cloud radius as $L_0 = L_i\, R$. Our fiducial simulation uses $k_i = 10^{-2}$ and $L_i = 10^{-2}$ to roughly match the initial conditions of GS11. However, P09 chose non-uniform initial conditions, with varying levels of k between the shock and the cloud. Similar to P09, we test the dependence of the LS74 turbulence model on the initial conditions by performing simulations with varying levels of initial turbulence k_i and length scale L_i, ranging from 10^{-4} to 10^{0} in both quantities. We perform this test at $N_R = 12$, as the increased viscosity decreases the allowed time step size.

Figure 3.11 presents a snapshot of the density-weighted average cloud colour column at $t = 6t_{\rm cc}$ for each combination of k_i and L_i in the LS74 model. We see that even an order of magnitude difference in either quantity produces notable differences in the evolution and mixing. Increasing either k or L increases the turbulent viscosity, to the point where the cloud is completely diffused into the background. This is also evident in Figure 3.12, which shows the time evolution of the mixing fraction $f_{\rm mix}$ in runs with different initial conditions for the LS74 model. Our results agree with earlier findings by P09, in which simulations with low initial turbulence ($k_i = 10^{-6}$ in the shock) showed decreased mixing (as evidenced by e.g, a slower decrease in core mass $m_{\rm core}$ in fig. 15g of P09) compared to simulations with higher initial turbulence ($k_i = 0.13$ in the shock). It is perhaps not surprising that different initial conditions produce different results, as each represents a particular physical state (i.e., more

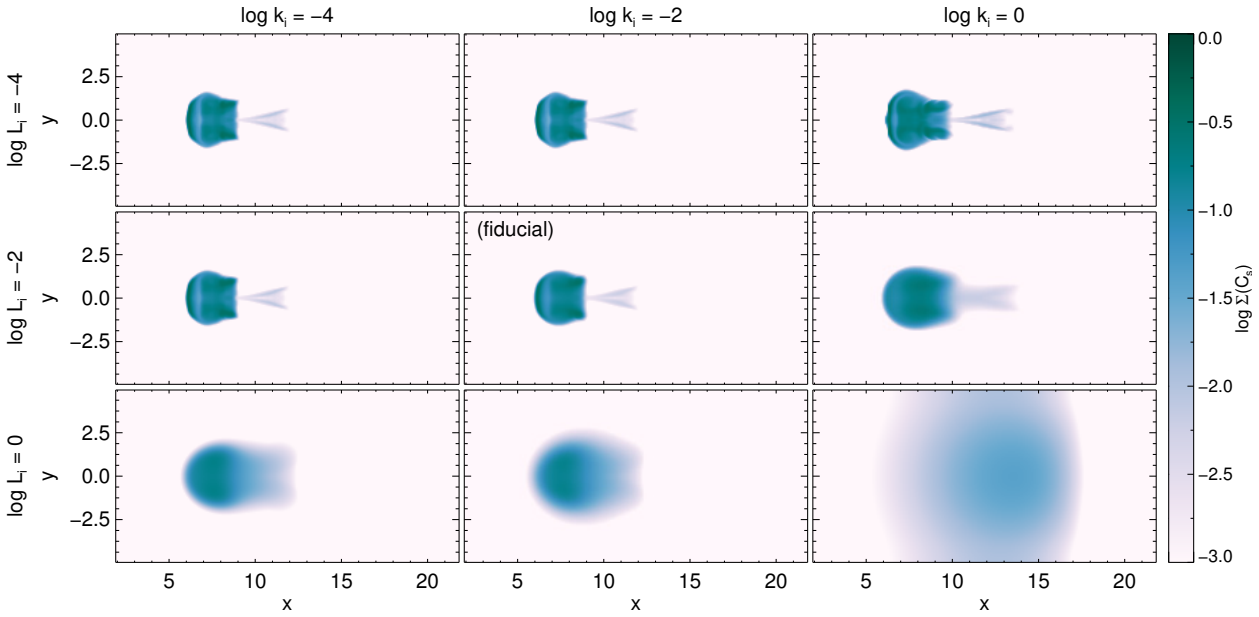

Figure 3.11: Snapshots of the density-weighted cloud column density $\Sigma(C_c)$ at $t = 6t_{\rm cc}$ for different initial conditions with the LS74 model. The columns show varying levels of initial turbulent energy $k_0 = k_i e_{\rm int}$; from left to right, $k_i = 10^{-4}$, 10^{-2}, and 1. The rows show varying initial turbulent length scale $L_0 = L_i R_c$; from top to bottom, $L_i = 10^{-4}$, 10^{-2}, and 1. Increasing either quantity increases the turbulent viscosity and hence the diffusion of the colour field. The units are arbitrary; ϵ_0 can be determined for each model using the relation in Section 3.2.1.

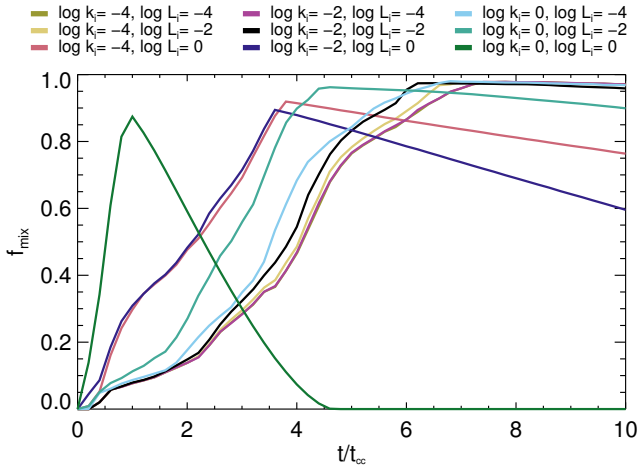

Figure 3.12: Time evolution of the mixing fraction $f_{\rm mix}$ for different initial conditions with the LS74 model. The colours show different combinations of initial turbulent energy k_i and initial turbulent length scale L_i. As the cloud is diffused, the cloud concentration C_c drops below the threshold and $f_{\rm mix}$ decreases.

or less turbulence at varying scales). One should carefully consider the initial conditions when using RANS models in an unsteady flow.

Finally, PP16 concluded that the LS74 k-ε model did not significantly affect the evolution of their three-dimensional shock-cloud simulations. However, this is most likely due to their choice of initial conditions; PP16 used $k_i = 10^{-6}$ and $L_i = 1.6 \times 10^{-4}$ (Pittard, personal communication) in all simulations, corresponding to very low initial levels of turbulence. While the LS74 model has very little effect for small (and probably reasonable) initial values of k and L, we demonstrate that the model can dramatically alter 3D simulations under certain conditions.

Resolution dependence

While 100 cells per cloud radius are necessary to see convergence of global quantities in 2D studies (Klein et al., 1994, P09), the resolution limit may be less strict in 3D. PP16 found that 32–64 cells may be sufficient for global convergence in 3D simulations. Figure 3.13 shows the time evolution of the diagnostic quantities in ILES simulations for resolutions $N_R = 10 - 200$. In agreement with PP16, we observe that globally-averaged quantities (b/a and δv) exhibit only small variation with increasing resolution for $N_R \gtrsim 25$.

However, it is difficult to assess whether or not this represents true convergence. For consistency with previous work, we perform an analysis similar to that described in Appendix A3 of PP16. We calculate the relative difference ΔQ_N between a measurement Q at a given resolution N and the same measure at a reference resolution $N_{\rm ref}$ (typically the highest resolution), given by eq. A1 of PP16 as

$$\Delta Q_N = \frac{|Q_N - Q_{N_{\rm ref}}|}{|Q_{N_{\rm ref}}|}. \tag{3.5.9}$$

Figure 3.14 shows the relative difference as a function of simulation resolution N_R for various diagnostic quantities at $t = 3t_{\rm cc}$. We compare results using $N_{\rm ref} = 100$ (as in PP16) and $N_{\rm ref} = 200$. We note that our axial direction is x, whereas in PP16 the axial direction

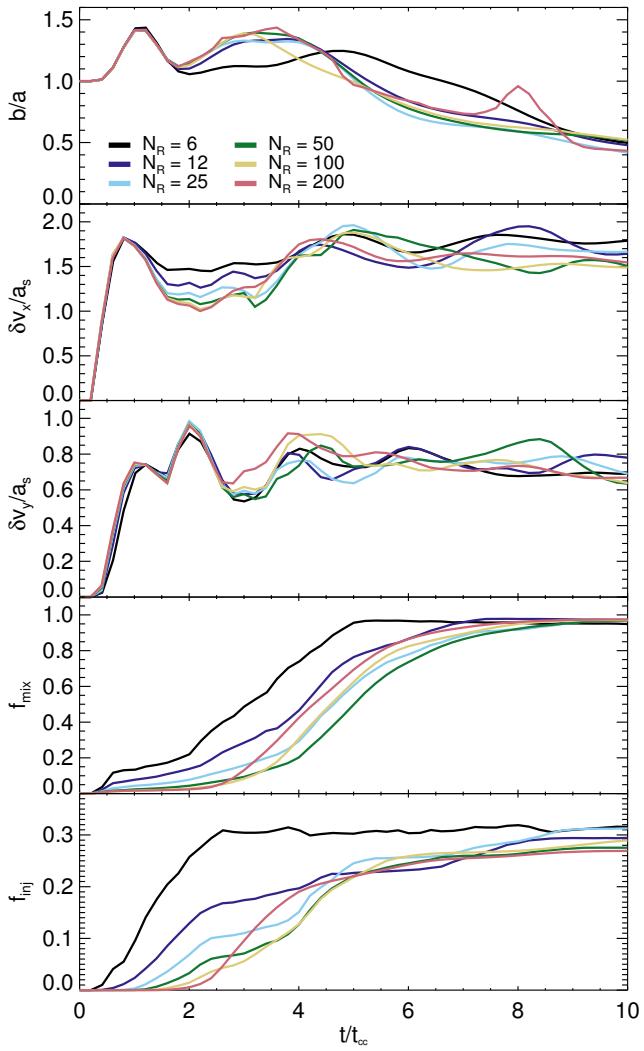

Figure 3.13: Similar to Figure 3.9, but for different simulation resolutions (measured in cells per cloud radius N_R) with no turbulence model (ILES). We observe only small variance in the evolution of global quantities (axis ratio b/a and velocity dispersions δv) for $N_R \gtrsim 25$. The mixing estimates ($f_{\rm mix}$ and $f_{\rm inj}$) decrease with increasing resolution up to $N_{\rm R} = 50$, but then increase again with increasing resolution.

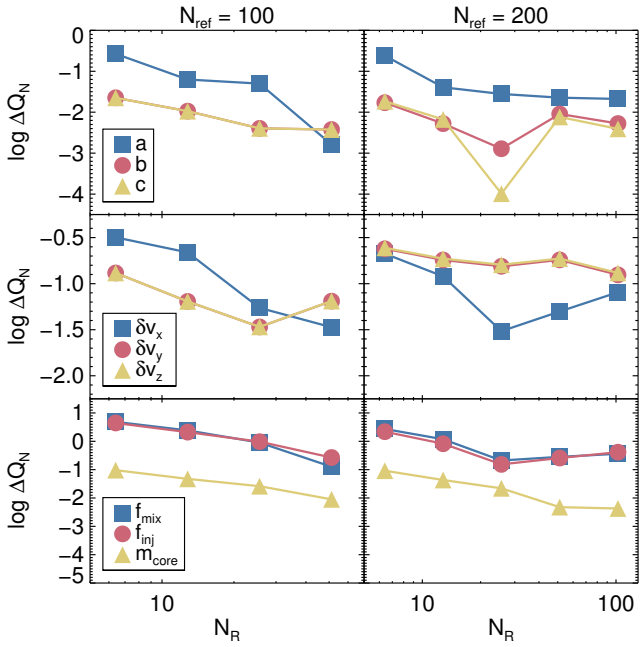

Figure 3.14: Estimates of the relative difference ΔQ_N as a function of resolution for global quantities (top row: effective radii; middle row: rms velocities) and mixing estimates (bottom row: mixing, injection, and core mass) at $t = 3t_{\rm cc}$ in the ILES simulations. The left column uses $N_R = 100$ as the reference resolution, while the right column uses $N_R = 200$. As in fig. A13 of PP16, we see decreasing relative difference with increasing resolution when $N_R = 100$ is used as the reference, which appears to indicate convergence. However, when $N_R = 200$ is used as the reference, there is no obvious sign of convergence. We attribute this to the partial resolution of the turbulent cascade for $N_R \gtrsim 50$.

is z; hence our quantity a should be compared to c in e.g., fig. A13 of PP16, and likewise our δv_x to their δv_z. For further comparison with PP16, we also calculate ΔQ_N for the core mass, $m_{\rm core}$, defined as

$$m_{\rm core} = \int_{C_c \geq 0.5} \rho C_c dV. \tag{3.5.10}$$

We finally note that our initialization of the cloud colour field is slightly different than in PP16; we use a constant value of $C_c = 1$ for $r \leq r_b$, while PP16 used a spatially varying C_c that decreased with increasing radius within the cloud.

If we use $N_R = 100$ as our reference resolution (left column of Figure 3.14), we find good agreement with PP16. The relative difference decreases with increasing resolution for most quantities, suggesting convergence. The only quantities with increasing difference are the velocity dispersions along axes perpendicular to the flow (δv_y and δv_z), which are not shown in fig A13 of PP16. However, the trend is less certain if we use our highest resolution simulation with $N_R = 200$ as the reference. There is no longer any sign of convergence, particularly in the mixing measures.

This is surprising given previous studies of the shock-cloud interaction. Xu & Stone (1995) found little variance in $f_{\rm mix}$ up to $N_R = 50$ in hydrodynamical shock-cloud interactions. While similar magneto-hydrodynamical simulations by SSS08 did not show convergence in $f_{\rm mix}$ up to $N_R \approx 120$, the authors predicted that, in simulations without an explicit viscosity, $f_{\rm mix}$ should continue to decrease with increasing resolution and tend to zero at infinite resolution. In examining the time evolution in Figure 3.13, we do not observe either trend. While we find that $f_{\rm mix}$ does show a decreasing trend up to $N_R = 50$, $f_{\rm mix}$ actually increases with increasing resolution beyond this point. A similar result is observed in fig. A8a of PP16; the mixing (as measured by $m_{\rm core}$) decreases with increasing resolution up to $N_R = 64$, at which point increased mixing (indicated by a faster decrease in $m_{\rm core}$) is observed for $N_R = 128$.

These results suggest that for resolutions $N_R \gtrsim 50$, mixing in the "inviscid" hydrodynamical shock-cloud simulation starts to be dominated by turbulent diffusion rather than

numerical diffusion. If the correlation time of the turbulence is short compared to the numerical diffusion time, the turbulent viscosity will dominate the diffusion (see the Appendix of Heitsch et al., 2004). At low resolutions ($N_R \leq 50$), the numerical viscosity dominates the dynamics and affects the growth of instabilities. As the resolution increases up to $N_R = 50$, numerical diffusion decreases, yet the turbulent cascade is not yet sufficiently resolved to show "true" turbulent mixing, i.e., mixing rates independent of the numerical diffusion. The mixing is therefore at a minimum near this resolution, which could explain the apparent "convergence" observed in Figure 3.14 when $N_R = 100$ is used as the reference.

For $N_R \gtrsim 50$, the numerical viscosity is reduced to the point that the RT and KH instabilities can grow at the cloud surface and seed further turbulent motions. This is evident in Figure 3.15, which shows a snapshot of the cloud column density at $t = 6t_{\rm cc}$ for varying simulation resolution. At high resolution, the leading edge of the cloud is saturated with RT fingers, and the shear at the cloud edge generates KH rolls that spawn additional vortices in the cloud wake. The turbulent cascade that develops is now largely resolved; the corresponding Reynolds number is large, and the mixing is increased.

The continued increase in mixing from $N_R = 100$ to $N_R = 200$ in our fiducial simulation suggests that the turbulent cascade is still not fully resolved at this point. It is unclear whether the mixing would continue to increase with increasing resolution. As our simulations are performed on a fixed grid with no mesh refinement, extending our simulations beyond $N_R = 200$ is not feasible given the computational burden (see 3.5.1).

We are also unable to perform simulations with $N_R > 25$ when using a turbulence model, due to the stability requirement that $dt \lesssim (\Delta)^2$. P09 found that the LS74 model reduced the convergence requirements in 2D, but PP16 found the model had little effect in 3D. As noted in Section 3.5.2, this may be a consequence of the low level of initial turbulence used in PP16. In our resolution tests up to $N_R = 25$, we find no significant benefit from the turbulence models.

Figure 3.16 compares the time evolution of the mixing estimates for the ILES model

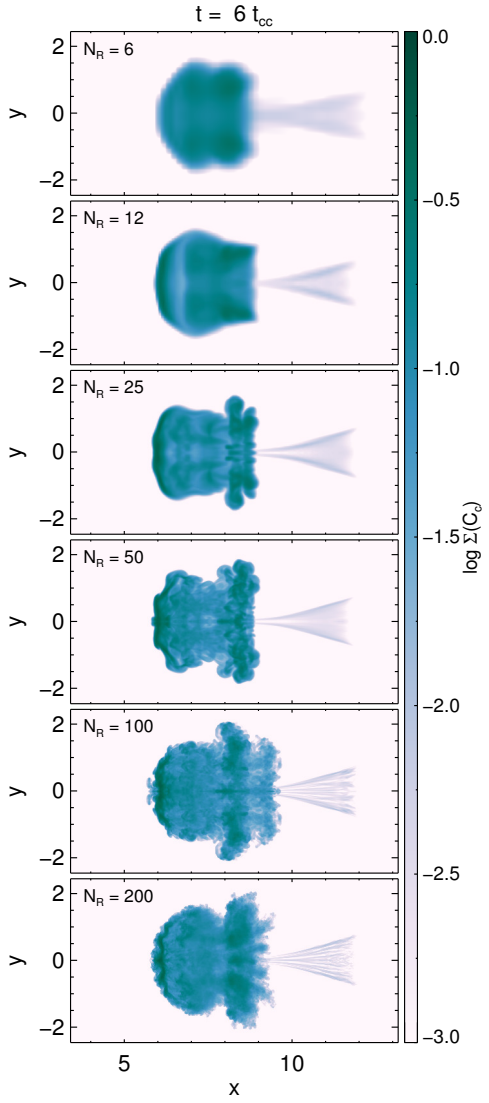

Figure 3.15: Snapshots of the density-weighted cloud column density $\Sigma(C_c)$ at $t = 6t_{\rm cc}$ for different simulation resolution with the inviscid (ILES) model. The resolution increases from top to bottom, from $N_R = 6$ up to $N_R = 200$. Above $N_R = 50$, the reduced numerical viscosity allows the growth of KH instabilities and enhances the mixing. The units are arbitrary.

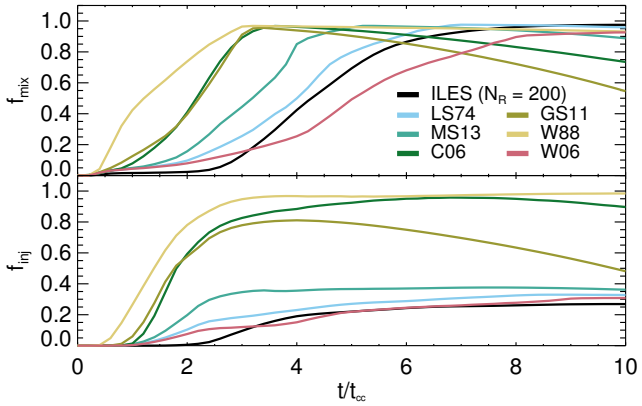

Figure 3.16: Similar to Figure 3.9, but only the mixing estimates are shown for the highest resolution ILES simulation ($N_R = 200$) and the turbulence models ($N_R = 25$). All models other than W06 show increased mixing relative to the ILES result, and LS74 and W06 show the best agreement.

at $N_R = 200$ with the turbulence models at $N_R = 25$. Despite the increased mixing at $N_R = 200$, all turbulence models other than W06 still indicate more mixing than observed. Yet if the ILES mixing continues to increase at higher resolutions, as the trend suggests, it may be that the turbulence models effectively predict the "correct" mixing.

Dependence on numerical methods

Figure 3.17 shows the resolution dependence of the mixing estimates at $t = 6t_{\rm cc}$ for various combinations of integrators, Riemman solvers, and reconstruction accuracy. Our fiducial simulation uses the CTU integrator with 3rd order reconstruction of the characteristic variables and the HLLC Riemann solver (denoted CTU_3_HLLC). We also test second order reconstruction (CTU_2_HLLC); the Roe Riemann solver (Roe, 1981) with H-correction (Stone et al., 2008) (CTU_3_Roe); and the Van Leer (VL) integrator (Stone & Gardiner, 2009) with second order reconstruction in the primitive variables (VL_2p_HLLC). We find that changing any of these algorithms in the Godunov scheme can alter the degree of mixing, especially the Riemann solver. The results obtained with the Roe solver are almost a factor of two below the fiducial results; furthermore, it does not show the trend of increasing $f_{\rm mix}$ from $N_R = 50$ to $N_R = 100$ as seen in the other runs. The dependence of ILES mixing on

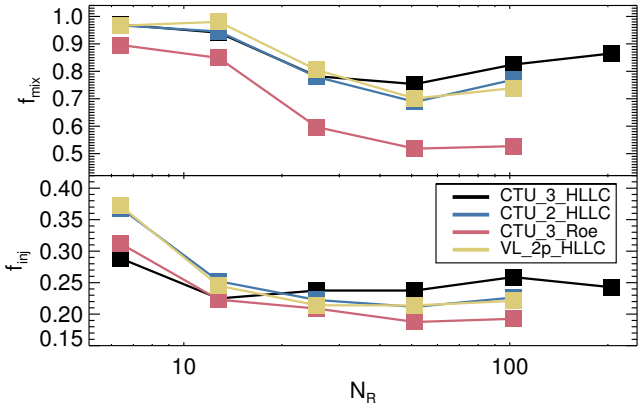

Figure 3.17: Estimates of the mixing fraction $f_{\rm mix}$ and injection efficiency $f_{\rm inj}$ at $t = 6t_{\rm cc}$ as a function of resolution, indicated by the number of cells per cloud radius N_R. Results are shown for different algorithms in the Godunov scheme; we test the effect of the integrator (CTU, VL), the order of reconstruction [3, 2, 2p], and Riemann solver (HLLC, Roe). The Riemann solver has the greatest effect, reducing the mixing estimates and failing to show an increase in mixing for $N_R > 50$.

the numerical algorithm underscores the utility of a turbulence model.

3.6 Discussion

In an effort to understand previous shock-cloud simulations, we have limited our exploration to RANS turbulence models. However, LES models are probably more appropriate for most astrophysical applications, including the shock-cloud interaction. The RANS approach tends to diffuse the small scale structure in the simulation, yet these are often the scales of greatest interest in astrophysics applications (e.g., star formation). In contrast, the resolved dynamics are largely unaffected in LES, and the filtering approach is ideal for unsteady flows. Despite these differences in formulation, the methods of LES are remarkably similar to RANS; the models have similar equations with similar closures, such as eddy-viscosity and gradient-diffusivity. The simplest LES model is the Smagorinsky model (Smagorinsky, 1963), which is essentially a zero-equation mixing-length model. The LES model of Schmidt & Federrath (2011) is a one-equation model; k is followed with a transport equation, while the turbulent length scale L is simply replaced by the grid scale spacing Δ. LES models also suffer the same calibration issues as RANS. Schmidt & Federrath (2011) calibrated their

model using high-resolution ILES simulations of turbulence, but it is difficult to determine if this approach is valid (see Section 3.5.2 and Figure 3.15).

We have only tested two-equation models. Models with fewer equations, such as the one-equation Spalart-Allmaras model (Spalart & Allmaras, 1992), are easy to implement but do not perform well in situations with inhomogeneous or decaying turbulence. However, models with two or fewer equations make use an isotropic eddy-viscosity. This assumption of isotropy severely limits the accuracy of these models in regions of high vorticity. Anisotropic models, such as the seven-equation Reynolds-Stress-Transport model (Wilcox, 2008), independently follow the six components of the turbulent stress tensor plus a dissipation equation. This approach is highly accurate, but the associated computational cost is often prohibitive. One compromise may be the use of a non-linear eddy-viscosity relation, such as that used in Schmidt & Federrath (2011). All of the RANS models considered here use linear eddy-viscosity relations, but the additional complexity of the non-linear relation improves results in complex flows without the need for additional stress transport equations (Gatski & Jongen, 2000).

We also note that the assumption of isotropy is incorrect in magnetized turbulence (Goldreich & Sridhar, 1995), as typically encountered in astrophysical applications. Eddies are stretched along the field lines, and the anisotropy is scale-dependent and increases toward smaller-scales (Cho & Lazarian, 2003). It is unclear if an anisotropic RANS model could be developed for magnetohydrodynamics (MHD); however, such models could be developed in the LES framework (Miesch et al., 2015). Indeed, closures for the MHD LES equations have been proposed (Vlaykov et al., 2016) but such methods have yet to be thoroughly validated.

One potential benefit of a turbulence model is the proper modeling of the RT instability (Dimonte et al., 2004). However, the buoyant turbulence models here considered seem to perform poorly in complex flows and generate excessive turbulence. Critically, the models have not been validated for use in supersonic, highly compressible turbulence, which is exactly the regime of interstellar gas dynamics. While compressibility corrections can be

used, simulations have demonstrated that they are physically incorrect (Vreman et al., 1996).

Finally, we note that we are limited in our use of turbulence models by an explicit time integration method – maintaining stability requires $dt \propto (\Delta)^2$. Implicit formulations are possible (e.g. Huang & Coakley, 1992) but the associated computational cost may be significant due to coupling between the turbulent variables.

3.7 Conclusions

We have developed a common framework for two-equation Reynolds-Averaged Navier-Stokes (RANS) turbulence models in the Athena hydrodynamics code. All models use a linear eddy-viscosity relation based on resolved dynamics to add turbulent diffusivity. We have implemented six RANS turbulence models: the k-ε models of LS74 and MS13; the k-L models of C06 and GS11; and the k-ω models of W88 and W06.

We have verified the models with the subsonic shear mixing layer. The models can only reproduce the correct mixing layer growth rate for certain definitions of the layer width δ (Figure 3.2), and the different definitions are not directly related. We have also extended the simulations into the supersonic regime, up to convective Mach numbers of 10, where compressibility corrections are needed to reduce the growth rate of the mixing layer in accord with experiment (Figure 3.3). Three common "compressibility corrections" from the literature (S89, Z90, and W92) perform very similarly and provide agreement with experimental results up to $M_c \approx 5$. The stress tensor modification implemented by GS11 provides similar results up to $M_c \approx 1$, but beyond this the model grows too slowly.

Three of the models tested (C06, GS11, and MS13) include buoyant effects (Rayleigh-Taylor and Richtmeyer-Meshkov instabilities). For these models, we use a simple stratified medium subject to constant acceleration to test the growth of the RT boundary layer. The model of GS11 shows the best agreement with experimental growth rates (Figure 3.5), while C06 grows too slowly and MS13 diverges at late times.

We then use the RANS models to simulate a generic astrophysical shock-cloud interaction. We follow the interaction in three dimensions for up to 10 cloud crushing times by implementing a co-moving grid. By using a consistent initial condition, we are able to compare global quantities as well as estimates of the mixing and injection returned by different turbulence models. We also generate an appropriate comparison by ensemble-averaging results from high-resolution inviscid simulations with grid-scale turbulence. We find that:

1. The k-ε models of LS74 and MS13 and the k-ω model of W06 generate the least turbulence and corresponding lowest numerical viscosity.These models show the best agreement with the reference inviscid turbulence (TILES) result (Figure 3.10) at the fiducial resolution ($N_R = 25$).

2. The k-L models of C06 and GS11 generate excessive turbulence within the cloud, leading to expansion, rapid disruption, and elevated mixing compared to the TILES result (Figure 3.9). The W88 k-ω model generates excessive turbulence within the shock front, which also leads to enhanced disruption. Overall, the W88 and C06 models show the least agreement with the reference results (Figure 3.10).

3. Compressibility effects play a small role in the shock-cloud interaction, at least at the Mach number considered here ($M = 10$), as the compressibility corrections do not noticeably alter the simulation evolution or mixing estimates.

4. In agreement with previous work by P09, we show that the turbulence models are highly sensitive to the initial conditions (Figure 3.12). For large initial values of k or L, the RANS models smooth the resolved dynamics beyond utility (Figure 3.11); for small initial values, the RANS models have negligible effects.

5. Globally-averaged quantities vary only slightly with increasing resolution at resolutions higher than 25 cells per radius (Figure 3.13). While this agrees with previous work up to 100 cells per radius (PP16), we find that beyond this point turbulent mixing begins

to be resolved [see also 6] and thus alters the dynamics, preventing true convergence (Figure 3.14).

6. Estimates of the mixing decrease with increasing resolution up to 50 cells per radius (Figure 3.13), but beyond this point the mixing increases, up to a resolution of 200 cells per radius – the current limit of our computational resources. This suggests that mixing in inviscid simulations does not trend toward zero at infinite resolution (Figure 3.14) but rather that the turbulent diffusivity becomes dominant when the numerical viscosity is sufficiently low.

7. The degree of mixing in the highest-resolution inviscid simulation ($N_R = 200$) agrees best with the predictions of the LS74 turbulence model (Figure 3.16), but it is unknown what will occur at higher resolution or in a different application. Furthermore, the choice of numerical method (particularly the Riemann solver) can shift the mixing fraction in ILES simulations by nearly a factor of two (Figure 3.17).

While the RANS turbulence models perform adequately in simple, specific test cases, it remains difficult to assess their veracity in complex dynamical applications. Further work toward understanding mixing in ILES simulations is necessary if proper calibrations are to be achieved.

CHAPTER 4: ENRICHMENT OF THE PRE-SOLAR CLOUD BY SUPERNOVA DUST GRAINS[1]

4.1 Introduction

The presence of short-lived radioisotopes (SLRs) in meteorites has been interpreted as evidence that the early solar system (ESS) was exposed to a supernova shortly before or during its formation. A primary source of SLRs is massive, evolved stars ($\geq 8M_{\odot}$). When a massive star ends its life, it explodes as a supernova and expels SLRs into the interstellar medium (ISM). The SLRs can then be incorporated into newly forming stars. It has long been suggested that the solar System was born near such an event (Cameron & Truran, 1977). However, the short half-life of these isotopes provides strong constraints on the proximity of the massive stars – the radioactive material must rapidly reach the pre-solar cloud to prevent significant decay, yet the material must also be traveling slow enough that the impact does not shred the cloud. This delicate balance has proved difficult to achieve in hydrodynamic simulations, as slowing the SN gas sufficiently suppresses the enrichment to several orders of magnitude below observed values.

As discussed in Sections 1.1.1 and 3.1, simulations of SLR enrichment in the 'triggered formation' scenario find injection efficiencies compatible with the lowest estimates for ESS abundances (Takigawa et al., 2008). Enrichment relies on hydrodynamical mixing of the ejecta into the pre-stellar gas, primarily via RT fingers (Boss & Keiser, 2012); as noted in Chapter 3, the turbulent mixing may be underestimated due to insufficient resolution.

Another possible solution to the mixing barrier problem is to concentrate the SN ejecta

[1]Portions of this chapter previously appeared as an article in Monthly Notices of the Royal Astronomical Society. The original citation is as follows: Goodson, M. D., Luebbers, I., Heitsch, F., & Frazer, C. C. "Chemical enrichment of the pre-solar cloud by supernova dust grains," MNRAS **462**, 2777-2791 (2016).

into dense clumps that can breach the cloud surface. The inner ejecta of Type II SNe are found to be clumpy and anisotropic in both observations (Grefenstette et al., 2014; Boggs et al., 2015) and simulations (Wongwathanarat et al., 2015). Pan et al. (2012) explore injection and mixing of clumpy SN ejecta into molecular clouds. The authors find that an over-dense clump can penetrate up to 1 pc into the target cloud, leaving a swath of enriched gas in its wake. Depending on the degree of clumpiness, the resulting enrichment can be comparable to ESS abundances.

As an alternative, Goodson et al. (2016b) explores the injection of SLRs via supernova dust grains as a way to overcome the mixing barrier. We numerically model the interaction of a supernova remnant containing SLR-rich dust grains with a nearby molecular cloud. We modify the Athena code to include dust drag forces and destruction (both thermal and non-thermal sputtering). We conclude from our simulations that sufficiently large ($a \gtrsim 1$ μm) dust grains can rapidly penetrate the cloud surface and deposit SLRs within the cloud, long before any gas can hydrodynamically mix at the cloud surface. Nearly half of all incident dust grains sputter or stop within the cloud, enriching the dense (eventually star-forming) gas. Our results suggest that dust grains offer a viable mechanism to deposit SLRs in dense star-forming gas and may be the key to reproducing the canonical solar system SLR abundances.

4.1.1 Supernova dust grains

The ejecta from both stellar winds and SNe have been predicted to condense and form dust grains (Clayton, 1979; Elmegreen, 1981; Kozasa et al., 1989). This prediction is supported by observations that find some SNe produce large amounts of dust ($\gtrsim 0.1$ M$\odot$) soon after explosion (Indebetouw et al., 2014; Matsuura et al., 2015). In addition, meteorites contain pre-solar grains that originated in massive stars, including SNe (Clayton & Nittler, 2004). Numerous authors (Clayton, 1975; Ouellette et al., 2005; Gaidos et al., 2009) have suggested that these dust grains will contain SLRs, and in fact some pre-solar grains show

evidence for *in situ* decay of ^{26}Al (Groopman et al., 2015). If the dust grains survive transport to the pre-solar cloud, they can dynamically decouple from the stalled shock front and penetrate into the dense gas, possibly delivering SLRs (Elmegreen, 1981; Foster & Boss, 1997).

Ouellette et al. (2010) have examined the role of dust grains in enrichment, considering injection into an already-formed proto-planetary disc. Although the disc's small cross-section places strong constraints on the SN distance, the authors found that over 70 per cent of dust grains with radii greater than 0.4 μm can survive the passage into the inner disc where they are either stopped or destroyed. Both fates contribute SLRs to the forming star, suggesting dust grains may favorably enhance enrichment. However, injection at the disc phase may be too late; CAIs containing SLRs probably formed within the first 300,000 years of solar system formation (Young et al., 2005), prior to the proto-planetary disc phase.

Injecting dust grains at the pre-stellar core phase may be more difficult. For grains impacting a dense pre-stellar core of number density $n \gtrsim 10^5$ cm^{-3}, only grains with radii $a \geq 30$ μm are able to penetrate the stalled shock front and deposit SLRs into the core (Boss & Keiser, 2010). 30 μm is greater than either simulated (Sarangi & Cherchneff, 2015) or meteoritic (Clayton & Nittler, 2004) SN grain radii (typically $a \lesssim 1$ μm). Therefore, if injection via dust grains is to be a viable scenario, it must occur at an even earlier phase.

Enriching the pre-solar molecular cloud prior to core formation has been suggested by several authors (Gaidos et al., 2009; Gounelle et al., 2009; Young, 2014) but remains largely untested with simulations. In this scenario, one to several massive stars, possibly across multiple generations, contribute SLRs to a large star-forming region. The solar system then forms from the enriched gas, eliminating the need for injection into a dense core. To our knowledge, the only numerical simulations of this scenario are presented by Vasileiadis et al. (2013), with a follow-up by Kuffmeier et al. (2016). The authors follow the enrichment of a massive ($\gtrsim 10^5$ M$\odot$) star-forming region over 20 Myr. A turbulent periodic box is allowed to evolve subject to star formation and SN feedback. The combined effect of numerous

explosions leads to an overall enrichment of ^{26}Al and ^{60}Fe in star-forming gas. The authors used passive particles to track SLRs, and they relied on numerical diffusion to mimic the mixing between SN ejecta and cold gas. While the resulting enrichment is broadly consistent with observed ESS values, a more detailed understanding of the injection mechanisms may be of interest.

4.1.2 Motivation

We attempt to bridge the gap between the small-scale injection scenario of Boss et al., and the global, large-scale approach of Vasileiadis et al., by studying the interaction of a single SN remnant with a large, clumpy molecular cloud. We focus on the details of the injection mechanism, investigating in particular the role of SLR-rich dust grains. We use hydrodynamical simulations to follow the evolution of the gas and dust over 0.3 Myr. The dust grains are decelerated by drag forces and destroyed by thermal and non-thermal sputtering, releasing SLRs into the gas phase. We estimate the amount of SLRs injected into the cloud and determine the dust grain radii needed for successful injection to occur.

We outline the numerical methods, including initial conditions and dust grain physics, in Section 4.2. We describe measures and analytic estimates for the injection efficiency in Section 4.3. We present the results of our simulations in Section 4.4 and discuss the implications for enrichment scenarios in Section 4.5. Finally, we summarize our conclusions in Section 4.6.

4.2 Methods

We use Athena to solve Eqs. 2.1.1–2.1.6. We do not include magnetic fields; therefore $B = 0$. We modify Eqs. 2.1.3 and 2.2.1 to include radiative heating and cooling (see Section

4.2.2):

$$\frac{\partial E}{\partial t} + \nabla \cdot [(E+P)\mathbf{u}] = n(\Gamma - n\Lambda) \quad (4.2.1)$$

$$\frac{\partial e}{\partial t} + \nabla \cdot (e\mathbf{u}) = -P\ \nabla \cdot \mathbf{u} + n(\Gamma - n\Lambda), \quad (4.2.2)$$

with the the gas number density $n \equiv \rho/(\mu m_{\rm H})$, the mass of hydrogen $m_{\rm H}$, a mean atomic weight $\mu = 1$, a heating rate Γ, and a volumetric cooling rate Λ. We also evolve several passive tracer fields:

$$\frac{\partial \rho C_{\rm c}}{\partial t} + \nabla \cdot (\rho C_{\rm c}\mathbf{u}) = 0 \quad (4.2.3)$$

$$\frac{\partial \rho C_{\rm s}}{\partial t} + \nabla \cdot (\rho C_{\rm s}\mathbf{u}) = 0 \quad (4.2.4)$$

$$\frac{\partial \rho_{\rm d}}{\partial t} + \nabla \cdot (\rho_{\rm d}\mathbf{u}) = 0 \quad (4.2.5)$$

using color field $C_{\rm c}$ to follow cloud material, color field $C_{\rm s}$ to follow gas-phase SN ejecta, and four passive density fields $\rho_{\rm d}$ to track sputtered particle mass (see Section 4.2.3).

We use the directionally unsplit van Leer (VL) integrator (Stone & Gardiner, 2009) with second order reconstruction in the primitive variables (Colella & Woodward, 1984) and the HLLC Riemann solver (Toro, 2009). Simulations are performed on Cartesian grids in three dimensions. We use an adiabatic equation of state with the ratio of specific heats $\gamma = C_{\rm p}/C_{\rm V} = 5/3$. Heating and cooling are included via composite curves (see Section 4.2.2). As the cooling breaks the total energy conservation, we find it necessary to include first-order flux correction (Lemaster & Stone, 2009) as well as internal energy fallback (see Section 2.2.1) to maintain positive states. Gravity, magnetic fields, and thermal conduction are not included. A summary of modifications made to Athena is given in Section 2.2.

Table 4.1: Summary of model parameters. Fiducial values are given in bold where necessary.

Parameter	Definition	Values
n_0	Ambient number density (cm^{-3})	1
T_0	Ambient temperature (K)	4910.58
R_c	Cloud radius (pc)	8.8
n_c	Cloud number density (cm^{-3})	$0.1 n_{cl} = 42.33$
T_c	Cloud temperature (K)	116.02
R_{cl}	Clump radius (pc)	0.05 $R_c = 0.44$
n_{cl}	Clump number density (cm^{-3})	423.25
T_{cl}	Clump temperature (K)	11.60
ϕ	Cloud volume filling factor	0.1, 0.3, **0.5**, 0.7, 0.9
N_R	Number of cells per cloud radius	12, 25, **50**, 100
E_{SN}	SN explosion energy (erg)	10^{51}
M_{ej}	SN ejected mass (M$\odot$)	10
R_{SNR}	SN remnant initial radius (pc)	4.6
d	Distance from SN center to nearest cloud edge (pc)	17.6
ρ_d	Dust grain density (g cm^{-3})	3.0
a	Dust grain radius (μm)	10, 1, 0.1, 0.01
N_p	Number of particles of each radius	10^3, 10^4, $\mathbf{10^5}$

4.2.1 Setup and initial conditions

We initialize a spherical gas cloud in a uniform ambient medium. We use a single fluid approximation with a mean atomic weight of $\mu = 1$, treating all the gas as neutral hydrogen. The background is in thermal equilibrium with temperature $T_0 \approx 4900$ K and number density $n_0 = 1$ cm^{-3}, consistent with average values for the diffuse ISM (McKee & Ostriker, 1977). The simulation domain extends from -53 to +35 pc in x and from -22 to +22 pc in y and z. Our fiducial simulation (run F) has a resolution of $\delta_x = \delta_y = \delta_z \approx 0.17$ pc, corresponding to roughly 50 cells per cloud radius ($N_R = 50$). Table 4.1 summarizes our simulation parameters and values.

Target molecular cloud

The target molecular cloud is stationary and centerd at the origin with radius R_c = 8.8 pc. To approximate the substructure observed in molecular clouds, we model the cloud as a distribution of small spherical clumps of number density $n_{cl} \approx 420$ cm^{-3} and size

$R_{\rm cl} = 0.05\ R_{\rm c} = 0.44$ pc, embedded in an intercloud medium (ICM) of number density $n_{\rm c} = 0.1\ n_{\rm cl}$. The clumps are generated randomly within the cloud radius $R_{\rm c}$ up to the desired volume filling factor $\phi = 0.5$. The clumps can overlap, but the density is not cumulative. The density profiles of both the cloud and the individual clumps are smoothed at the edges, and both the cloud and clumps are in pressure equilibrium with the background at $P/k_{\rm B} \approx 4900$ K cm^{-3}. The clumps have a temperature $T_{\rm cl} \approx 12$ K, which also guarantees thermal equilibrium. The ICM is slightly warmer ($T_{\rm c} \approx 120$ K) and is not in strict thermal equilibrium, but the subsequent cooling is negligible and does not affect the dynamics.

The cloud edge is smoothed using the profile

$$n(r) = n_0 + \frac{n_{\rm c} - n_0}{1 + (r/R_{\rm c})^{k_{\rm n}}}, \tag{4.2.6}$$

where r is the radius from the origin and $k_{\rm n}$ controls the steepness of the profile. We use $k_{\rm n} = 20$ to give a steep profile. Each clump is given a similar profile by letting $n_0 \to n_{\rm c}$, $n_{\rm c} \to n_{\rm cl}$, and $R_{\rm c} \to R_{\rm cl}$. To trace cloud material, the passive color field $C_{\rm c}$ is set to unity where $n \geq n_{\rm c}$ and zero otherwise (Shin et al., 2008).

Supernova remnant

We initialize the supernova remnant (SNR) at the start of the energy-conserving phase. The shock front has expanded to a radius $R_{\rm SNR} = (3M_{\rm ej}/(4\pi\rho_0))^{1/3}$ after time $t_{\rm SNR} \approx [R_{\rm SNR}(1.90E_{\rm SN}/\rho_0)^{-1/5}]^{5/2}$, where $M_{\rm ej}$ is the mass ejected from the SN and $E_{\rm SN}$ is the total energy of the SN explosion. We set $M_{\rm ej} = 10$ M$\odot$ and $E_{\rm SN} = 10^{51}$ erg, resulting in $R_{\rm SNR} \approx 4.6$ pc and $t_{\rm SNR} \approx 1000$ yr. We numerically calculate profiles for the density, radial velocity, and pressure based on the Sedov–Taylor (ST) blast-wave solutions (Taylor, 1950; Sedov, 1959) and interpolate these quantities on to the computational grid using a cubic spline. Athena uses a finite-volume method; hence if we sample only the cell-centerd location (as is usually done), the resulting SNR will suffer distortion from grid effects. We find it necessary to sub-sample 8^3 support points within each cell to construct the volume-averaged

cell-centerd conserved variables.

The SNR is centerd at a distance $d = 2\ R_{\rm c} \approx 18$ pc from the near edge of the cloud along the negative x-axis. This is broadly consistent with the separation distance of central stars in OB associations from bordering molecular gas, such as in Cepheus OB2 (Patel et al., 1998). For our target (cloud) parameters, the 'radioactivity distance' (equation 2, Looney et al., 2006) for uniform ^{26}Al enrichment to the initial solar system abundance is (given uncertainties in SN yield) between 10 and 20 pc. As our distance is at the upper end of this range, our enrichment estimates should be considered lower limits, as decreasing the separation would reduce the geometric dilution (see Section 4.3.2).

To follow the SN gas-phase ejecta, we initialize the passive color field $C_{\rm s}$ to unity within $R_{\rm SNR}$ and zero elsewhere. For the dust-phase ejecta, we randomly place $N_{\rm p} = 10^5$ particles of each of the four radius groups (see Section 4.2.3) within 0.9 $R_{\rm SNR}$, for a total of 4×10^5 particles. The particle input radius is truncated to prevent interpolation errors at the discontinuity. Particles are initialized with a radial velocity determined from the ST solution.

4.2.2 Thermal physics

On the time and distance scales considered here, the dynamics of the SNR should not be strongly affected by radiative cooling. Cioffi et al. (1988) and Blondin et al. (1998) have estimated the time and location for SNR transition from the Sedov–Taylor phase to the radiative phase. For our SN parameters ($E_{\rm SN} = 10^{51}$ erg, $n_0 = 1$ cm^{-3}), the transition radius is approximately 19 pc, slightly further than the distance from the SN to the cloud surface. However, radiative cooling is expected to strongly affect the dynamics of the shock-cloud interaction. Melioli et al. (2005) have shown that cooling reduces the fragmentation and destruction of the cloud, and Boss et al. (2008) find cooling by molecular species is essential to successfully inject SLR material into the pre-solar cloud. It is therefore critical to include radiative heating and cooling effects.

The temperatures in our simulation span over eight orders of magnitude, from the hot

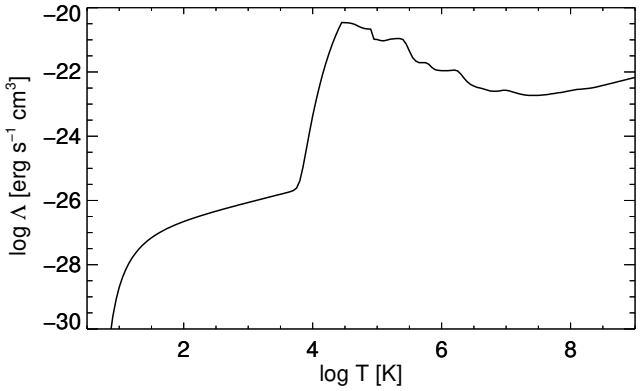

Figure 4.1: Volumetric cooling rate $\Lambda(T)$ (solid line) as a function of temperature T from 3 to 10^9 K. This composite cooling curve is constructed by blending three cooling functions from the literature: for $T < 10^4$ K, a modified version of equation (4) from Koyama & Inutsuka (2001); for 10^4 K $< T < 10^{8.5}$ K, the CIE rates from Sutherland & Dopita (1993); and for $T > 10^{8.5}$ K, the free–free rate of equation (5.15b) in Rybicki & Lightman (1985).

SN ejecta ($T \gtrsim 10^9$ K) to the cold molecular gas ($T \lesssim 10$ K). To cover this temperature range, we combine three standard composite cooling curves into a single cooling function, shown in Fig. 4.1. For temperatures $T < 10^4$ K, we use a modified version of equation (4) in Koyama & Inutsuka (2001):

$$\Lambda_{\rm KI}(T) = 2 \times 10^{-26} \left\{ 10^7 \exp \frac{-118400}{T + 1000} + 0.014 \sqrt{T} \exp \frac{-22.75}{\max[1.0, (T - 4.0)]} \right\} \text{ erg s}^{-1} \text{ cm}^3. \quad (4.2.7)$$

This is a fit to the cooling rates of Wolfire et al. (1995). For temperatures 10^4 K $< T < 10^{8.5}$ K, we use the collisional ionization equilibrium (CIE) cooling rates for solar metallicity given in table 6 of Sutherland & Dopita (1993). For temperatures $T > 10^{8.5}$ K, we use the free–free cooling rate given by equation (5.15b) in Rybicki & Lightman (1985):

$$\Lambda_{\rm RL}(T) = 1.42554 \times 10^{-27} \; g \; \sqrt{T} \text{ erg s}^{-1} \text{ cm}^3, \quad (4.2.8)$$

with a Gaunt factor $g = 1.5$. The transition between regimes is smoothed with a hyperbolic tangent function. For heating, we use $\Gamma(T) = 2 \times 10^{26}$ erg s^{-1} below 10^4 K and smoothly

transition to $\Gamma(T) = 0$ above 10^4 K.

Heating and cooling are implemented as source terms for the total energy (and internal energy). The cooling time-scale is typically much shorter than the hydrodynamical time-step; we therefore use an iterative explicit method (adaptive Runge–Kutta–Fehlberg) to integrate the source terms in time. The update is performed each time step via operator splitting.

4.2.3 Dust grains

Dust grains are modelled using Lagrangian tracer particles, where each simulated particle represents a collection of dust grains with similar properties and motions. Trajectories of the particles are integrated using the fully implicit method of Bai & Stone (2010), which we have incorporated into the VL integrator in Athena. In a Cartesian coordinate system, Athena solves an equation of motion for each particle given by

$$\frac{d\mathbf{v_i}}{dt} = -\frac{\mathbf{v_i} - \mathbf{u}}{t_{\rm stop}}, \tag{4.2.9}$$

with $\mathbf{v_i}$ the velocity vector of particle i, $\mathbf{u}$ the local gas velocity vector, and $t_{\rm stop}$ the particle stopping time due to gas drag. Neglecting grain charges and assuming only pure hydrogen gas, the (collisional) drag law is given by (Draine & Salpeter, 1979)

$$\frac{dv_i}{dt} \approx -\frac{2\pi a^2 n k_{\rm B} T G_0(s)}{(4/3)\pi \rho_{\rm d} a^3}, \tag{4.2.10}$$

with

$$G_0(s) \approx \frac{8s}{3\sqrt{\pi}}(1 + \frac{9\pi}{64}s^2)^{1/2} \tag{4.2.11}$$

and

$$s \equiv (\frac{m_{\rm H}\mathbf{v}_{\rm rel}^2}{2k_{\rm B}T})^{1/2}, \tag{4.2.12}$$

where a is the dust grain radius, $k_{\rm B}$ is the Boltzmann constant, T is the temperature of the gas, n is the gas number density, $\rho_{\rm d}$ is the internal density of the dust (which we treat as

constant at $\rho_{\rm d} = 3.0$ g cm^{-3}), $m_{\rm H}$ is the mass of hydrogen, and $\mathbf{v}_{\rm rel} \equiv \mathbf{v_i} - \mathbf{u}$ is the relative velocity difference between the dust and gas. The stopping distance is evaluated as

$$t_{\rm stop} = \frac{\sqrt{\pi}}{2\sqrt{2}} \frac{a\rho_{\rm d}}{n\sqrt{m_{\rm H} k_{\rm B} T}} (1 + \frac{9\pi m_{\rm H}}{128 k_{\rm B} T} \mathbf{v}_{\rm rel}^2)^{-1/2}. \tag{4.2.13}$$

The gas properties (n, T, $\mathbf{u}$) at each particle's location are calculated from nearby grid points using a triangular-shaped cloud (TSC) interpolation scheme (Hockney & Eastwood, 1988). There is no momentum feedback from the particles on the gas.

Dust grain sizes

The drag force and the sputtering rates depend on the dust grain radius a. Since the size distribution of grains formed in SN ejecta is still a matter of debate (Clayton & Nittler, 2004; Bianchi & Schneider, 2007; Nozawa et al., 2007; Sarangi & Cherchneff, 2015; Marassi et al., 2015), we follow the approach of Ouellette et al. (2010) and implement an initial 'distribution' of four radii: $a = 10$, 1, 0.1, and 0.01 μm. Each radius group is initialized with the same number of particles ($N_{\rm p} = 10^5$), and the sputtered mass from each radius group is tracked using a separate passive scalar field ($\rho_{\rm d}$, see Section 4.2.3).

Sputtering

The dust grains will be eroded by both thermal and non-thermal (kinetic) sputtering. We use sputtering rates estimated from the results of Nozawa et al. (2006), neglecting the slight differences in sputtering rate due to dust composition.

Non-thermal sputtering results from high-speed collisions of a dust grain with gas molecules and depends on the magnitude of the relative velocity $|\mathbf{v}_{\rm rel}|$ between the gas and the dust. For simplicity, we adopt the polynomial fit of Ouellette et al. (2010, eqs. 13,14)[2] to the

[2]Note that Ouellette et al. (2010) contain a typographical error in the definition of x; cm s^{-1} should be km s^{-1}.

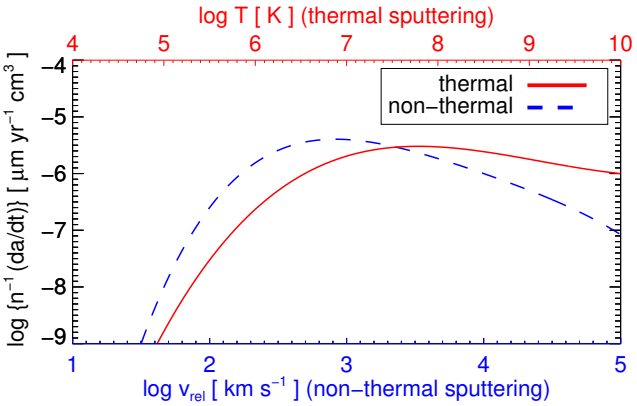

Figure 4.2: Polynomial fits to the thermal (solid red line) and non-thermal (dashed blue line) sputtering rates, estimated from fig. 2 of Nozawa et al. (2006). The non-thermal sputtering varies with the relative velocity $|\mathbf{v}_{\rm rel}|$ between the dust and the gas (bottom axis), and the thermal sputtering varies with the gas temperature T (top axis). Both rates depend on the gas number density n and are given in volumetric units (μm yr^{-1} cm^3).

non-thermal (kinetic) sputtering rates of Nozawa et al. (2006, fig. 2b):

$$y_{\rm k} = -0.1084 x_{\rm k}^4 + 1.7382 x_{\rm k}^3 - 10.5818 x_{\rm k}^2 + 28.1292 x_{\rm k} - 32.7024 \tag{4.2.14}$$

with $x_{\rm k} = \log_{10}(|\mathbf{v}_{\rm rel}|/1 \text{ km s}^{-1})$ and

$$(\frac{da}{dt})_{\rm k} = -10^{y_{\rm k}} \, (\frac{n}{1 \text{ cm}^{-3}}) \, \mu\text{m yr}^{-1}, \tag{4.2.15}$$

with the velocity difference between the dust and the gas $|\mathbf{v}_{\rm rel}|$ in km s^{-1}, and the gas number density n. Fig. 4.2 shows the volumetric non-thermal sputtering rate $n^{-1}(da/dt)$ (solid blue line) as a function of the relative velocity $|\mathbf{v}_{\rm rel}|$ (bottom axis).

Thermal sputtering is due to the thermal motion of the gas and depends on the temperature T. Similar to the procedure used by Ouellette et al. (2010) for the non-thermal sputtering rate, we generate an average fit to the thermal sputtering rates of Nozawa et al. (2006, fig. 2a) with the polynomial

$$y_{\rm t} = -0.001911 x_{\rm t}^4 + 0.12275 x_{\rm t}^3 - 2.4011 x_{\rm t}^2 + 18.6752 x_{\rm t} - 56.2785 \tag{4.2.16}$$

with $x_{\rm t} = \log_{10}(T/1\ {\rm K})$ and

$$(\frac{da}{dt})_{\rm t} = -10^{y_{\rm t}}\ (\frac{n}{1\ {\rm cm}^{-3}})\ \mu{\rm m\ yr}^{-1}. \tag{4.2.17}$$

Fig. 4.2 also shows the volumetric thermal sputtering rate $n^{-1}\ (da/dt)$ (dashed red line) as a function of the temperature T (top axis).

We treat thermal and kinetic sputtering independently, adding the contributions to determine the erosion. However, the thermal motions of the gas will skew the relative velocity difference between the dust and the gas, particularly at high temperatures. We note that the more detailed treatment of Bocchio et al. (2014) leads to slightly lower sputtering rates in the high temperature regime, suggesting that our sputtering rates are overestimated and hence our injection efficiencies should be considered lower bounds in this regard.

The erosion rates (equations 4.2.15 and 4.2.17) are applied at first order via operator splitting. A particle is assumed to be completely destroyed when its radius decreases to $10^{-4}\ \mu$m. As the particles are eroded, they release SLRs back into the gas phase. To continue tracking the sputtered SLRs in gas phase, we deposit the sputtered dust mass into a passive density field ${\rho_{\rm d}}$[3]. This field is initially set to zero and is advected with the gas. Each initial grain radius group has its own unique passive density field. The mass is distributed into nearby cell-centered field locations using the same TSC interpolation scheme used to determine gas properties (Hockney & Eastwood, 1988).

At each time-step, the mass lost by each particle is given by

$$\Delta M_{\rm p} = \frac{4\pi\rho_{\rm p}}{3}[a^3 - (a - \Delta a)^3], \tag{4.2.18}$$

where a is the current grain radius, $\Delta a = [(da/dt)_{\rm k} + (da/dt)_{\rm t}]\ dt$ is the total change in radius due to both non-thermal and thermal sputtering, $M_{\rm p}$ is the mass of each particle, and

[3]Note that this is a passive density rather than a concentration (i.e., color) field. The density is a conserved quantity, whereas the concentration is not.

$\rho_{\rm p}$ is the density of each particle. It is important to note that $\rho_{\rm p} \neq \rho_{\rm d}$, as each particle in Athena represents a collection of many individual dust grains. As the density of each dust grain is fixed at $\rho_{\rm d} = 3.0$ g cm^{-3}, the exact number of dust grains per particle depends on the dust mass and the number of particles used; e.g. for 1 M$\odot$ of 1 μm dust distributed in 10^5 particles, each particle represents $\sim 10^{39}$ dust grains. For simplicity, we normalize such that each particle has an initial mass of unity. Hence, if every particle of a given radius group is completely destroyed, the total mass of the passive density field is $N_{\rm p}$. With this simplification, $\rho_{\rm p} = 3/(4\pi a_0^3)$, where a_0 is the original radius of the particle, and

$$\Delta M_{\rm p} = \frac{a^3 - (a - \Delta a)^3}{a_0^3}. \tag{4.2.19}$$

Verification of dust dynamics and sputtering

We have modified the Lagrangian tracer particles in Athena to include the drag force given by Eq. 4.2.13 and the sputtering rates given by Eqs. 4.2.15 and 4.2.17. We verify the dynamics and destruction in a simple test case. A particle representing each radius group is initialized at $x = 0$ with $v_{\rm rel} = 500$ km s^{-1} in a uniform medium of density $n = 10$ cm^{-3} and temperature $T = 10^5$ K. For $a = 10$, 1, 0.1, and 0.01 μm, the stopping times are 1.50×10^5, 1.5×10^4, 1.5×10^3, and 1.5×10^2 years, respectively. Figure 4.3 compares the evolution of the position, velocity, and radius of the four particles in Athena to the exact solution. Overall, the implementation in Athena performs well, with an rms error in the position of 1.4×10^{-2} for the largest particles. The rms error increas with decreasing radius, up to 0.84 for the smallest grains, but these grains are less important for enrichment as they stop rapidly and carry the least SLR mass.

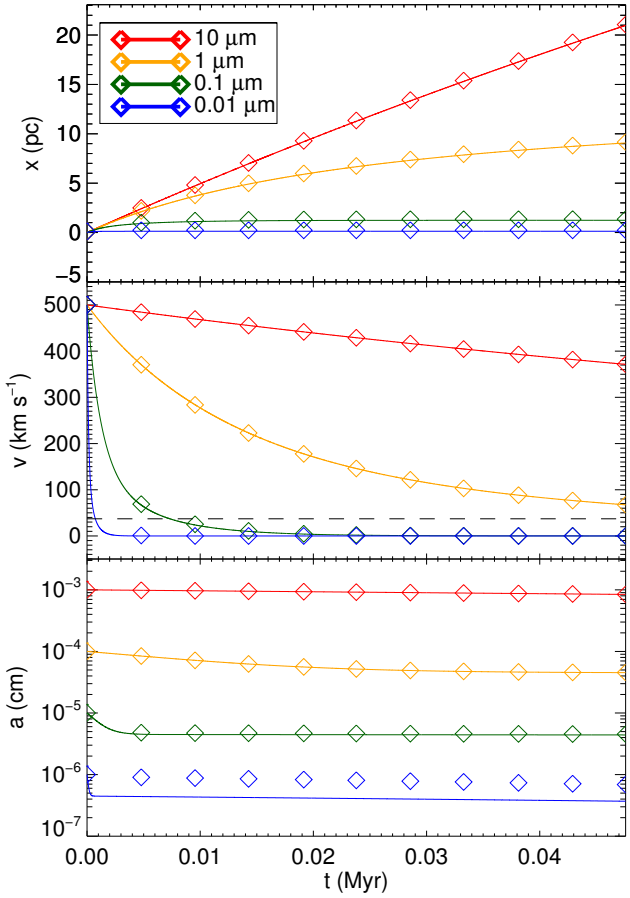

Figure 4.3: Time evolution of the position x, velocity v, and radius a of dust particles in a simple test case. The dust radius is indicated by color. The exact solution is given by the solid line, and results from Athena are overlaid as open squares. Overall, our implementation in Athena follows the dynamics and sputtering to high accuracy; only the smallest ($a = 0.001\mu$m) grains show disagreement, but as these grains have little mass and are rapidly stopped they contribute very little to the enrichment.

4.3 Enrichment estimates and measures

4.3.1 Dust production

We are interested in enriching a molecular cloud with SLRs from a nearby SN. The quantity of SLRs produced by a SN varies with progenitor mass (Chieffi & Limongi, 2013), and any estimate is dominated by uncertainties in reaction rates (Iliadis et al., 2011) and progenitor models (Woosley & Heger, 2007). Of this amount, some fraction will condense into dust grains of various sizes (Sarangi & Cherchneff, 2015; Marassi et al., 2015). Furthermore, the dust grains that form behind the SNR forward shock will subsequently be processed by the reverse shock (Bianchi & Schneider, 2007; Nozawa et al., 2007; Biscaro & Cherchneff, 2016; Bocchio et al., 2016). Calculations of dust grain processing in the reverse shock predict survival rates of 0–100 per cent, depending on the grain size, grain composition, and local gas density (Nozawa et al., 2007; Bianchi & Schneider, 2007; Silvia et al., 2010, 2012). Additionally, inhomogeneities in the SNR produce small clumps of higher density that may shield the forming dust grains from destruction (Biscaro & Cherchneff, 2014, 2016; Micelotta et al., 2016). For simplicity, we assume a homogeneous SNR and background medium. Because we begin our simulations at the end of the free-expansion phase, we neglect processing by the reverse shock. We therefore assume at least some amount of dust has survived and is still well-coupled to the gas, consistent with 1D simulations (Biscaro & Cherchneff, 2016; Bocchio et al., 2016). Our calculations are normalized such that the condensation efficiency and survival rate do not affect the evolution.

4.3.2 Geometric dilution

As the SNR expands, the ejecta become distributed over a larger surface area. For a spherical target of radius R, at a distance d from the SNR center, the fraction of the total

ejecta incident on the target cross-section is

$$\eta_{\rm geom} = \frac{\pi R^2}{4\pi d^2}. \tag{4.3.1}$$

For our fiducial set-up, $d \approx 18$ pc and $R \approx 9$ pc; then $\eta_{\rm geom} \approx 0.06$. This factor is used to normalize our injection efficiency η (see Section 4.3.3).

4.3.3 Injection efficiency

The mixing of incident material with a target has been the subject of much previous numerical work, both in the context of the standard shock-cloud interaction (Xu & Stone, 1995; Shin et al., 2008; Pittard et al., 2009) and in solar system enrichment (Boss & Keiser, 2012; Ouellette et al., 2010). Defining a good measure of the mixing is difficult and depends on the context. We therefore quantify the mixing in two ways.

For the shock-cloud interaction, the mixing fraction is typically defined by the dilution of cloud material into ambient material, using the cloud color field ($C_{\rm c}$). Conversely, we are interested in the mixing of incident 'shock' material (SN ejecta) into the cloud. We therefore define the color-based injection efficiency $\eta^{\rm c}$ as the total mass of SN ejecta in cells containing at least 10 per cent cloud material (i.e. $C_{\rm c} \geq 0.1$), normalized by the initial ejecta mass and the incident ejecta fraction ($\eta_{\rm geom}$). If all of the ejecta incident on the cloud cross-section are 'injected' into the cloud, $\eta = 1$.

In the context of solar system enrichment, we are most interested in enriching the densest (potentially star-forming) regions of the target cloud. Both Boss & Keiser (2012) and Ouellette et al. (2010) consider ejecta to be 'injected' above an absolute density threshold. We therefore calculate an alternate injection efficiency, $\eta^{\rm d}$, defined as the total mass of SN ejecta in cells with density greater than the ICM density (i.e. $n > n_{\rm c}$), also normalized by the incident mass fraction ($\eta_{\rm geom}$). This measure only probes the dense clumps; thus if $\eta^{\rm d} \ll \eta^{\rm c}$, most of the ejecta are in diffuse cloud material.

For both measures, we use $\eta_{\rm g}$ for the gas-phase injection and $\eta_{\rm d}$ for general dust grain

injection (note that $\eta_{\rm d}$ and $\eta^{\rm d}$ are different quantities). We further determine the dust injection for each radius group, using η_{10}, η_1, $\eta_{0.1}$, and $\eta_{0.01}$ for the $a = 10$, 1, 0.1, and 0.01 μm dust grains, respectively.

The gas injection efficiency is defined as the mass ratio of 'injected' gas phase SN ejecta (as traced by the passive color field $C_{\rm s}$) to the initial amount of gas-phase SN ejecta that is incident on the cloud surface:

$$\eta_{\rm g} \equiv \frac{\int_V (\rho C_{\rm s})_{\rm injected}}{\eta_{\rm geom} \int_V (\rho C_{\rm s})_{t=0}}, \tag{4.3.2}$$

where 'injected' material is defined using either the cloud color field ($C_{\rm c} > 0.1$) or the density ($n > n_{\rm c}$).

For the dust grain injection efficiency, we must include both sputtered material (traced by the passive density field $\rho_{\rm d}$) and intact grain material. Further, we only consider dust grains that have been stopped, i.e. decelerated to a relative velocity less than 10 per cent of the local sound speed. For each initial radius group, the dust grain injection efficiency is calculated as the mass ratio of both stopped and sputtered material to the initial total particle mass incident on the cloud surface (which we have normalized to be the number of particles $N_{\rm p}$):

$$\eta_{\rm d} \equiv \frac{[\sum^{N_{\rm p}} (M_{\rm p})_{v_{\rm rel} \leq 0.1 c_{\rm s}} + \int_V (\rho_{\rm d})]_{\rm injected}}{\eta_{\rm geom} \sum^{N_{\rm p}} (M_{\rm p})_{t=0}}. \tag{4.3.3}$$

The unknown quantities discussed in Section 4.3.1 (e.g. SLR yield, dust production, dust destruction) can then be included when estimating final SLR abundances. Note that we do not account for radioactive decay during transit. The half-life of ^{26}Al is $t_{1/2} \approx 0.7$ Myr. For our fiducial SNR, the shock impacts the cloud after roughly 0.03 Myr; therefore only ~ 3 per cent of the total ejected ^{26}Al will have decayed by that time. Over the full duration of our simulation (0.3 Myr), ~ 25 per cent of the ^{26}Al will have decayed. The short half-life of ^{26}Al underscores the need for both rapid transport and incorporation into the molecular cloud.

4.4 Results

4.4.1 Dynamical evolution

We follow the evolution of the SN remnant and its interaction with the pre-solar molecular cloud for 0.3 Myr. Fig. 4.4 shows the first 0.03 Myr of time evolution of the fiducial simulation (run F). As the ST solution is initialized with both kinetic and thermal energy, the pressure discontinuity at the edge of the SNR launches a shock wave (forward shock) into the ambient medium. Because the gas-phase ejecta are traced with a passive color field ($C_{\rm s}$), they instead follow the contact wave, which lags behind the forward shock. The dust grains begin with the ejecta velocity and therefore initially travel with the expanding gas, experiencing no drag or non-thermal sputtering. However, the high temperatures in the SNR cause significant thermal sputtering. Fig. 4.5 shows the ratio of sputtered mass to total mass for each grain radius group over time. At early times, thermal sputtering dominates and erodes nearly 80 per cent of the smallest ($a = 0.01$ μm) grains.

As the remnant expands into the ambient medium, the forward shock accumulates more material, eventually slowing and cooling into a dense shell. The smallest grains ($a = 0.01$ μm) remain well-coupled to the inner gas ejecta. Slightly larger ($a = 0.1$ μm) grains outpace the inner ejecta but stall in the dense forward shock. The relative velocity difference then generates non-thermal sputtering, which contributes almost equally to the destruction of the 0.1 μm grains (compare the dashed and dash–dotted green lines in Fig. 4.5). Both of the smaller grain groups are almost completely stopped and destroyed by sputtering within the remnant. In contrast, the larger grains ($a \geq 1.0$ μm) remain largely intact and dynamically decouple from the ejecta due to their higher inertia. The large grains also pass through the forward shock and ballistically impact the cloud before the shock arrives. Once in the cloud, the grains rapidly slow and kinetically sputter due to the increased densities and high relative velocities.

The behaviour of the dust grains in the SN remnant agrees well with the results of

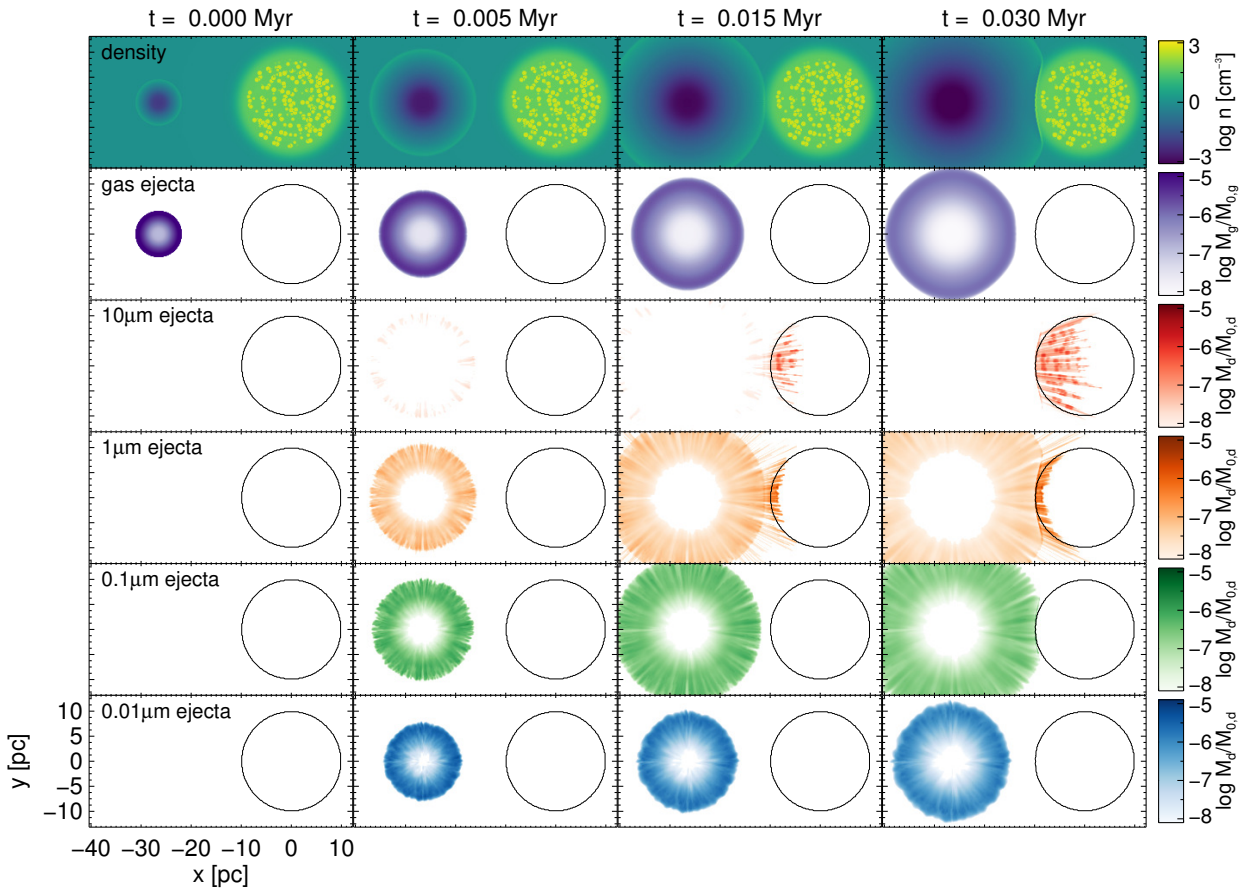

Figure 4.4: Time evolution of our fiducial simulation (run F) at early stages (the first 0.03 Myr). Each image is a mid-plane slice at $z = 0$. The top row shows the total number density n in cm^{-3}. All other rows show the mass fraction of each tracer on a per cell basis relative to the initial tracer mass. The second row is the gas-phase ejecta, traced by the color field C_s. The remaining rows are the sputtered mass of dust grains from each radius group. The black contour traces the cloud boundary, defined where the cloud color field $C_c \geq 0.1$. The particles located within the central midplane slice ($-\delta_z/2 < z < +\delta_z/2$) are overlaid in grey according to their initial radius group. The smallest grains ($a = 0.01$ μm) remain well-coupled to the inner ejecta by the drag force and sputter almost completely before impacting the cloud. The 0.1 μm grains outpace the inner ejecta but stall in the forward shock. The large ($a \gtrsim 1.0$ μm) dust grains decouple and outpace the shock front due to their larger inertia, reaching the cloud and depositing SLRs before the shock impacts the surface. The sputtering of individual particles is visible in the form of radial contrails from the SN center.

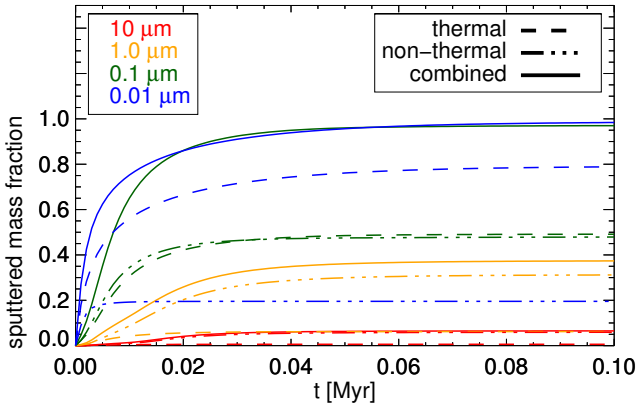

Figure 4.5: Fraction of total particle mass eroded by thermal sputtering (dashed), non-thermal sputtering (dash-dot), and the combination of both (solid) during the first 0.1 Myr of the fiducial simulation (run F). colors indicate the initial radius group (red: 10 μm; orange: 1 μm; green: 0.1 μm; blue: 0.01 μm). The 0.01 μm grains are rapidly and significantly eroded, predominately by thermal sputtering in the hot SNR. Over 20 per cent of the total mass is lost in the first kyr, and nearly 100 per cent in the first 10 kyr. The 0.1 μm grains also experience rapid destruction but with almost equal contributions from both thermal and non-thermal sputtering, and nearly all are destroyed. The larger grains fare better, with roughly 40 and 10 per cent destruction rates for the 1 and 10 μm groups respectively. In both instances, the destruction is dominated by non-thermal sputtering as the grains pass through the shock front and into the cold, dense cloud.

Bocchio et al. (2016). The authors performed 1D simulations of the growth and erosion of dust in SNRs including multiple grain compositions, plasma drag, and detailed sputtering. Despite using simplified dust physics, we obtain very similar results to the evolution of Mg_2SiO_4 presented in fig. 3 of Bocchio et al. (2016): (1) small grains ($a = 0.01$ μm) are highly eroded in the remnant and remain within the ejecta region; (2) slightly larger ($a = 0.1$ μm) grains pass through the ejecta but remain within the forward shock; and (3) the larger ($a = 1.0$ μm) grains are eroded very little and eventually move beyond the forward shock.

Fig. 4.6 shows the evolution of the simulation after forward-shock impact. As noted in Section 4.2.2, the SNR is only just starting to cool when it impacts the molecular cloud surface. The expansion velocity of the shell is still supersonic (~ 350 km s^{-1}) at impact. The hot, diffuse gas encounters a cold, dense wall and deflects around the edges, ablating material. A slower shock is transmitted into the cloud, and the clumpy substructure provides channels and gaps for the gas to enter the cloud. Both the clumpy substructure and the efficient

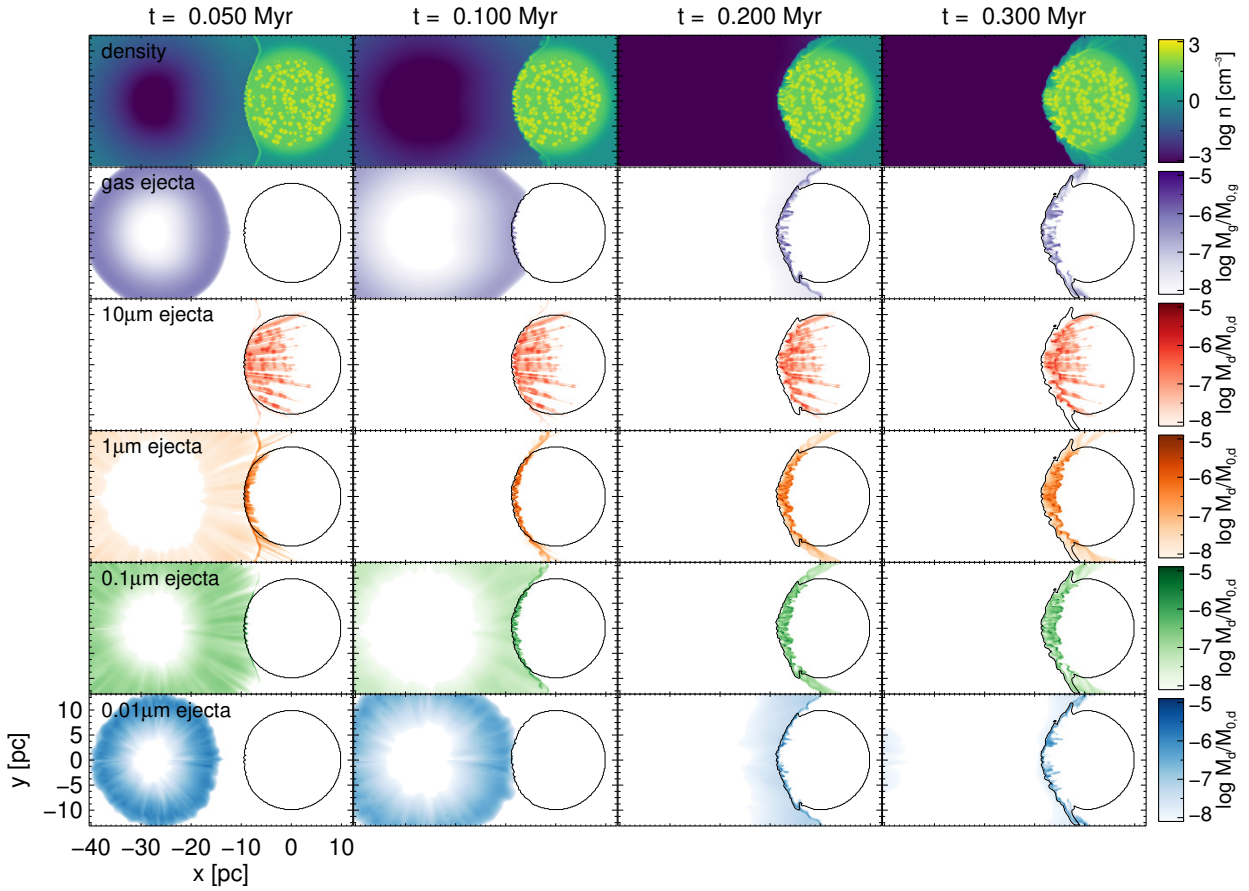

Figure 4.6: Same as Fig. 4.4, but at later stages. The forward shock impacts the cloud within ~ 0.03 Myr, but the inner ejecta does not arrive until $t \sim 0.06$ Myr. The clumpy substructure of the cloud creates channels for the impinging gas to penetrate and mix. At later times, Rayleigh–Taylor instabilities lead to injection of gaseous SLRs through the cloud surface. After 0.3 Myr, nearly all the grains within the cloud have either been stopped or sputtered. Nearly half of the dust grains incident on the cloud are captured, and the largest grains penetrate furthest.

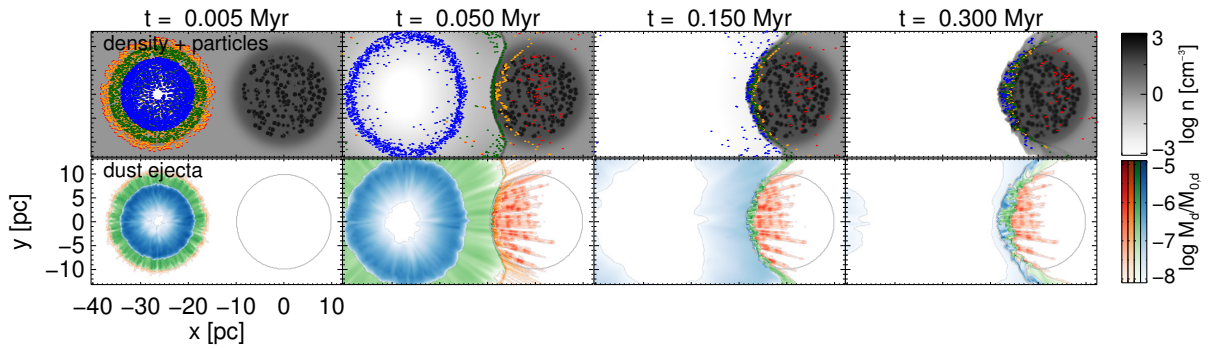

Figure 4.7: Time evolution of the fiducial simulation (run F) illustrating the spatial stratification of the dust grains (top row) and sputtered SLRs (bottom row) due to initial grain radius distribution. As in Figs 4.4 and 4.6, the images are mid-plane slices at $z = 0$. In the top row, particles located from $-\delta/2 \leq z \leq +\delta/2$ are overlaid on a desaturated map of number density. Each dust grain group is color-coded by initial radius (red: 10 μm; orange: 1 μm; green: 0.1 μm; blue: 0.01 μm). The same color scheme holds in the bottom row, now showing the sputtered SLR mass fraction, relative to the initial tracer mass. The grey contour defines the cloud edge. As the simulation proceeds, the dust grains separate spatially based on initial radius, with the larger grains travelling further into the cloud. This stratification could help explain anomalies in observed solar system abundances, such as the low ^{60}Fe/^{26}Al ratio.

radiative cooling prevent the formation of a stand-off shock, which is usually observed in the adiabatic shock–cloud interaction (Nakamura et al., 2006) and could drastically limit the SLR injection (see Section 4.4.6). At late times, the Rayleigh–Taylor instability begins to manifest at the cloud surface, driving fingers into the cloud that will eventually mix and inject SLRs in the gas phase.

In contrast to the hydrodynamical (gas-phase) mixing, the large dust grains rapidly inject SLRs throughout the cloud. Fig. 4.7 shows the evolution of the dust grains, as well as a combined view of the sputtered mass from each initial radius group. The largest ($a = 10$ μm) grains penetrate furthest, sputtering most of their mass in the leading edge of the cloud. The smaller grains have been largely stopped and sputtered before entering the cloud. Still, the SLR contents of the 0.1 μm grains have outpaced the inner ejecta and mix into the dense gas ~ 0.05 Myr earlier. Nearly all grains incident on the cloud are sputtered and stopped within the cloud, i.e. only grains at grazing angles can re-emerge from the cloud interior.

4.4.2 Injection of SLRs

We are interested in the enrichment of the densest (eventually star-forming) gas. Therefore, we analyse the SLR deposition as a function of density (Fig. 4.8). Comparing the dust ejecta to the gas ejecta, the gas ejecta are mostly distributed in the diffuse SNR and background ISM. In contrast, the 10 μm grains deposit a significant fraction of mass into the densest gas, and smaller particles deposit smaller fractions in the dense gas. This effect is further quantified in Fig. 4.9, which compares the injection efficiency η of both dust and gas as a function of time. At late times, the color-based injection efficiency is roughly equivalent for all grain sizes ($\eta^{\rm c} \sim 0.5$), indicating that nearly half the incident material has been mixed into the cloud. However, the density-based injection $\eta^{\rm d}$ decreases with decreasing grain size, to the point that the smallest grains and gas deposit only negligible amounts of ejecta in the densest regions. This agrees qualitatively with Boss & Keiser (2012), who found only a small fraction of incident gas-phase material is injected into a dense pre-stellar core ($\eta^{\rm d}_{\rm g} \approx 0.03$). This indicates that only the large grains are able to enrich the densest gas ($n > n_{\rm c}$). Table 4.2 provides a summary of final injection efficiencies from all simulations performed.

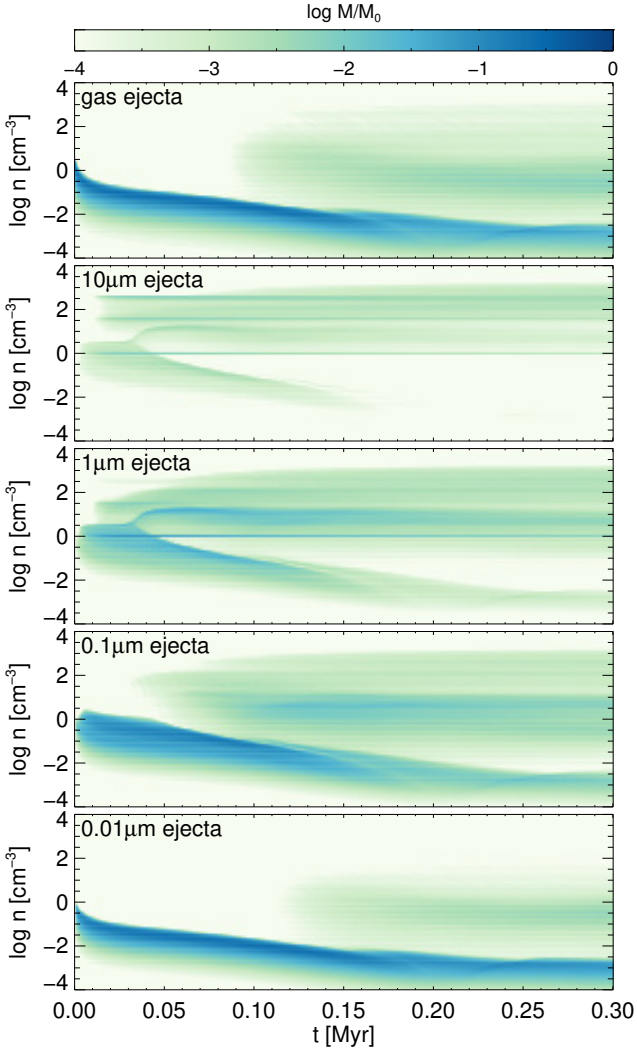

Figure 4.8: Tracer mass fraction binned logarithmically by density across time for the fiducial simulation (run F). The top panel shows the SNR gas tracer ($\rho C_{\rm s}$). The rest of the panels show the mass deposited into gas phase by dust grain sputtering ($\rho_{\rm d}$) for each initial grain size (10, 1, 0.1, and 0.01 μm). While hydrodynamical mixing is largely restricted to later times and low cloud densities (top panel), the large ($a \geq 1$ μm) dust grains enrich higher densities at earlier times. Only the smallest grains do not reach higher densities. The prominent horizontal line at $n = 1$ cm^{-3} corresponds to the ambient medium, while lower densities are located in the diffuse SNR.

Table 4.2: Summary of supernova-blast simulations and results. The parameters ϕ, N_R, and N_p are defined in Tabel 4.1, and definitions of the injection efficiencies η are given in Section 4.3.3.

Run name	ϕ	N_R	$N_{\rm p}$	$\eta_{\rm g}^{\rm c}$	$\eta_{10}^{\rm c}$	$\eta_{1}^{\rm c}$	$\eta_{0.1}^{\rm c}$	$\eta_{0.01}^{\rm c}$	$\eta_{\rm g}^{\rm d}$	$\eta_{10}^{\rm d}$	$\eta_{1}^{\rm d}$	$\eta_{0.1}^{\rm d}$	$\eta_{0.01}^{\rm d}$
F	0.5	50	10^5	0.45	0.39	0.48	0.45	0.46	0.065	0.36	0.37	0.23	0.011
R1	0.5	12	10^5	0.59	0.38	0.42	0.46	0.47	0.083	0.36	0.25	0.13	0.030
R2	0.5	25	10^5	0.49	0.38	0.44	0.43	0.45	0.11	0.36	0.31	0.19	0.048
R4	0.5	100	10^5	0.39	0.39	0.50	0.46	0.34	0.11	0.36	0.42	0.30	0.031
N1	0.5	50	10^4	0.44	0.38	0.47	0.44	0.44	0.066	0.35	0.37	0.23	0.012
N2	0.5	50	10^6	0.45	0.38	0.47	0.44	0.44	0.066	0.35	0.36	0.22	0.011
FT	0.5	50	10^5	0.30	0.41	0.51	0.46	0.29	0.045	0.38	0.41	0.31	0.056
NS	0.5	50	10^5	0.45	0.00	0.0012	0.011	0.029	0.065	0.00	0.0012	0.0096	0.011
NC	0.5	50	10^5	0.00	0.37	0.30	0.00033	0.00	0.00	0.29	0.043	0.000	0.000
F1	0.1	50	10^5	0.46	0.34	0.49	0.45	0.47	0.052	0.23	0.36	0.22	0.0081
F3	0.3	50	10^5	0.45	0.37	0.48	0.45	0.46	0.057	0.32	0.36	0.22	0.0092
F7	0.7	50	10^5	0.43	0.40	0.48	0.44	0.44	0.071	0.38	0.38	0.23	0.012
F9	0.9	50	10^5	0.42	0.40	0.48	0.44	0.42	0.071	0.39	0.39	0.24	0.010

Because the SLRs decay, the enrichment needs to occur rapidly. As seen in both Figs 4.8 and 4.9, the particles are able to deposit SLRs in the cloud ~ 0.1 Myr before gas phase mixing occurs. For all dust grain sizes, the injection of SLRs occurs rapidly, reaching peak values in less than 0.1 Myr. This is contrasted with the gas, which slowly mixes and is still increasing its injection amount when the simulation ends. The gas injection efficiency only becomes comparable to the dust injection efficiencies after 0.2 Myr.

4.4.3 Resolution convergence

As discussed in Chapter 3, the degree of mixing in inviscid simulations is controlled by numerical viscosity. In the three-dimensional shock-cloud interaction, previous work has found that about 32–64 cells per cloud radius (indicated as N_R) are necessary for convergence of global quantities (Pittard & Parkin, 2016), and our fiducial simulation falls within this range ($N_R \approx 50$). However, we find that the small scale mixing does not convergence 3.5.2, as the turbulent cascade begins to be resolved at this point.

Fig. 4.10 compares the fiducial result to simulations performed at both lower and higher resolution (runs R1–R4), up to 100 cells per radius ($1024 \times 512 \times 512$ grid points). The injection efficiency of the larger grains ($a \geq 0.1$ μm) increases only slightly with increasing resolution. In contrast, the injection of smallest grains ($a = 0.01$ μm) and the gas ejecta decreases as the resolution increases. The larger injection efficiencies at lower resolution may be attributable to increased numerical diffusion, leading to increased mixing at the cloud interface. Overall, the trend is sufficiently flat to conclude that our three-dimensional simulations are sufficiently resolved at $N_R = 50$.

In the previous resolution test, we kept the number of particles fixed at $N_\mathrm{p} = 10^5$. We do not expect the particles to be strongly affected by simulation resolution. However, the number of particles used may alter the injection. As the particles are placed randomly within the SNR, a sufficient number of particles are required to eliminate any gaps when the shock wave encounters the cloud surface. We repeat our fiducial simulation varying the number of

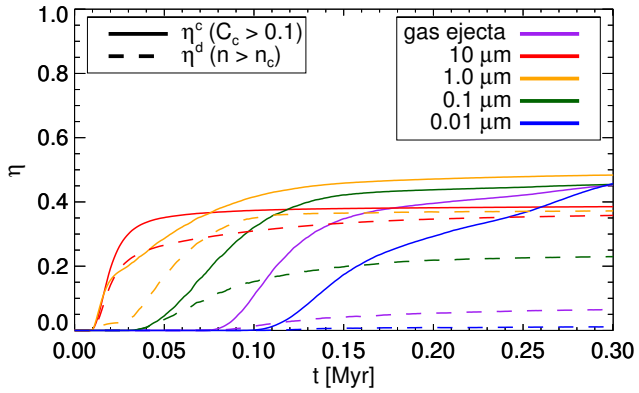

Figure 4.9: Injection efficiency η as a function of time for the ejecta in our fiducial simulation (run F). Injection is measured using the cloud tracer (solid) and density threshold (dashed). Each tracer is color-coded as in Fig. 4.4 (purple: gas; red: 10 μm; orange: 1 μm; green: 0.1 μm; blue: 0.01 μm). The largest grains ($a \geq 1$ μm) arrive within the first 0.01 Myr and rapidly deposit a substantial fraction ($\gtrsim 20$ per cent) of their SLR mass within 0.1 Myr. The intermediate grains ($a = 0.1$ μm) are sputtered and stopped in the forward shock and arrive slightly ahead of the gas. The smallest grains ($a = 0.01$ μm) sputter significantly before entering the cloud, yet injection of SLRs from these grains continues as gas at the leading edge of the cloud is subsequently mixed by Rayleigh-Taylor instabilities. While the color-based injection is approximately the same ($\eta^{\rm c} \gtrsim 0.4$) for all ejecta types, the density-based injection ($\eta^{\rm d}$) decreases with grain radius, indicating most of the smaller grain deposition is in diffuse intercloud gas.

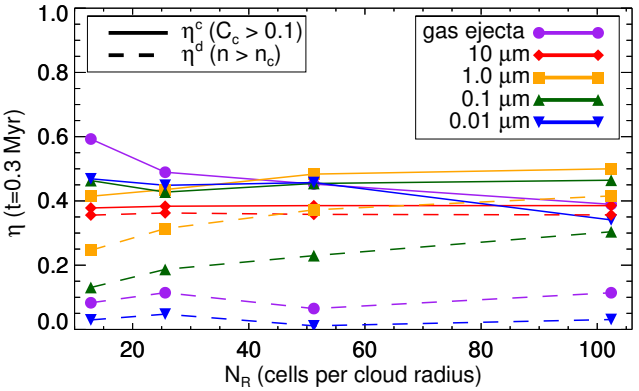

Figure 4.10: Injection efficiencies η as a function of simulation resolution, represented by the cells per cloud radius N_R. η is evaluated at simulation termination ($t = 0.3$ Myr) using the cloud tracer (solid) and density threshold (dashed). Each tracer is color-coded as in Fig. 4.4 (purple: gas; red: 10 μm; orange: 1 μm; green: 0.1 μm; blue: 0.01 μm). The injection efficiency of the largest grains increases slightly for both measures, as the density peaks within the clumps are better resolved and capture more material. Injection decreases for the smallest grains and the gas due to decreased numerical diffusion at the cloud surface.

particles from $N_{\rm p} = 10^4$ (run N1) to $N_{\rm p} = 10^6$ (run N2). We find no significant variation in injection efficiency with particle number (see Table 4.2).

4.4.4 Effect of supernova remnant model

We have also performed a simulation using the standard thermal pulse to initialize the SNR rather than an exact ST solution. In this model (run FT), we inject $E_{\rm SN} = 10^{51}$ erg of thermal energy and $M_{\rm ej} = 10$ M$\odot$ uniformly into a spherical volume of radius 20 cells. With sufficient resolution, this approach has been shown to evolve approximately into the ST solution after only 2 kyr (Kim & Ostriker, 2015) and is therefore often used for its simplicity (Vasileiadis et al., 2013). Because the SNR has no initial kinetic energy, injecting the particles at the start of the simulation would generate non-physical drag. We therefore let the thermal pulse evolve for 3 kyr before injecting the particles, which are then placed in the forward shock with the local gas velocity.

The final state of the simulation is displayed in the second column of Fig. 4.11. Overall, the result obtained using the thermal pulse is almost indistinguishable from the ST model – the shock thickness, velocity, and arrival time are approximately the same, and the injection efficiencies at simulation termination are nearly identical (see Table 4.2). There is a small difference in the dust grains due to the initialization; because we wait 3 kyr to insert the dust in the thermal pulse model, the grains experience less thermal sputtering and arrive later.

4.4.5 Effect of sputtering

We compare the fiducial results to a simulation run without sputtering (run NS). The third column of Fig. 4.11 shows the result at simulation termination. The hydrodynamics and the gas tracer field are not affected by the lack of sputtering, since there is no feedback from the particles to the gas. The drag force depends on the dust grain radius, and therefore the dust dynamics are altered by the lack of sputtering. The largest grains pass almost

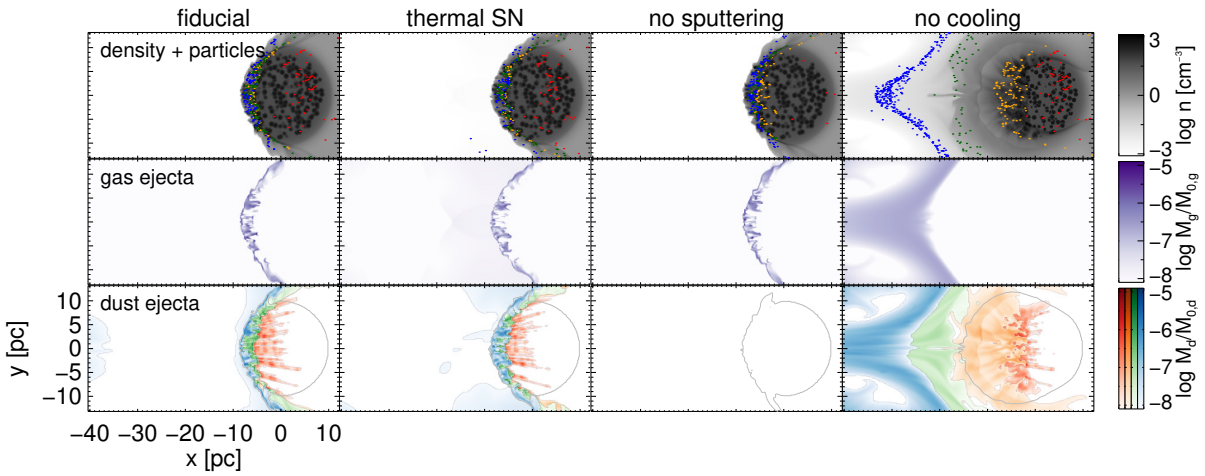

Figure 4.11: Similar to Fig. 4.7, but comparing different simulations at $t = 0.3$ Myr. From left to right, the columns show (a) the fiducial simulation (run F); (b) the SNR initialized as a thermal pulse rather than a ST solution (run FT); (c) no sputtering of dust grains (run NS); and (d) no thermal physics, i.e. purely adiabatic with no heating or cooling (run NC). The middle row shows the gas ejecta tracer field. Comparing the fiducial to the thermal pulse, the initialization of the SNR does not appear to drastically alter the evolution or injection. Without sputtering, there are no SLRs released in gas phase; hence the bottom panel is blank. The 10 μm dust grains are not stopped in the cloud by drag and re-emerge. Without cooling, the impact of the SNR creates a bow shock that deflects incoming gaseous ejecta. The large, intact grains still decouple and penetrate the cloud surface, injecting SLRs.

entirely through the target cloud. The rest of the grains also travel further into the cloud but are eventually stopped by the drag force. Since there is no sputtering, no SLRs are released into the gas phase and the injection is measured solely by the stopped grain criterion (see Section 4.3.3).

4.4.6 Effect of radiative cooling

We compare the fiducial results to a simulation run without radiative heating and cooling (run NC). As seen in the fourth column of Fig. 4.11, the behaviour of the gas is radically altered. As the shock wave impacts the cloud surface, the purely adiabatic equation of state results in the formation of a stand-off shock at the leading edge of the cloud, diverting impinging material and preventing mixing. The gas-phase ejecta and the smaller grains (which are either coupled to the gas or sputtered) do not mix at all with cloud material, and the injection efficiency is essentially zero (see Table 4.2). Cooling lowers the effective adiabatic index of the shock-cloud interaction. As the gas is compressed, the strong radiative losses reduce the shock stand-off distance, allowing mixing of phases and enhancing injection. The larger dust grains are less affected as they are largely intact at impact and still penetrate the cloud surface.

4.4.7 Filling factors

In contrast to previous shock–cloud and SN injection simulations, we include substructure in the target cloud through high-density clumps randomly embedded in an ICM. The fiducial simulation has a cloud volume filling factor of $\phi = 0.5$. We expect the SN shock wave to interact differently as the filling factor is varied. Clumps at the cloud surface provide channels for injection, reducing the need for Rayleigh–Taylor fingers. We examine the effect of varying the filling factor from $\phi = 0.1$ to 0.9 (runs F1–F9); results are given in Table 4.2. Overall, the dust grain injection is largely unaffected by the filling factor. A higher ϕ leads to slightly increased injection efficiency, most notably in the 10 μm grains, as the additional

clumps capture grains on trajectories near the periphery of the cloud.

4.5 Discussion

4.5.1 The Role of dust grains

We investigate the role of SN dust grains in enriching a nearby molecular cloud with SLRs. Our results indicate that dust grains formed in SN ejecta can survive transport through the ISM and significantly enrich neighbouring clouds. We find that sufficiently large grains ($a \geq 1$ μm) decouple from the expanding SN remnant, pass through the shock front and cloud surface, and deposit a significant fraction of their SLR mass into the cloud ($\eta_{\rm d} \gtrsim 0.4$). In particular, large dust grains enrich the dense gas rapidly, preventing significant SLR decay. Smaller grains ($a \leq 0.1$ μm) sputter and stall in the SNR and contribute SLRs predominately through gas-phase mixing. The gas-phase ejecta mix slowly through hydrodynamic and thermal instabilities at the cloud surface.

Our results agree with those of Ouellette et al. (2010) despite using very different targets (molecular cloud versus proto-stellar disc) and SN distances (18 pc versus 0.1–2 pc). The authors found that a considerable fraction ($\eta \gtrsim 0.8$) of grains larger than 1 μm are injected into the target, which compares favorably with our estimates ($\eta_{\rm d} \gtrsim 0.4$). Similarly, the smallest grains ($a = 0.01$ μm) are slowed and completely destroyed. We also find approximate agreement with our estimate for gaseous injection; Ouellette et al. (2010) estimated $\eta_{\rm g} \lesssim 0.01$, while we find $\eta_{\rm g}^{\rm d} \approx 0.1$.

4.5.2 ^{60}Fe/^{26}Al ratio

We observe that the dust drag and sputtering naturally lead to a spatial stratification between grains of different sizes, illustrated in Fig. 4.7. One of the leading arguments against a SN enrichment source is that the SLR abundances in our solar system do not precisely match predicted SN yields. In particular, some estimates of the ratio of ^{60}Fe/^{26}Al in the ESS are orders of magnitude lower than expected in SNe (Tang & Dauphas, 2012),

casting doubt on a SN origin for 26Al (Gounelle, 2015). However, if the primary carriers of ^{60}Fe and ^{26}Al condense into grains of different characteristic radii, these isotopes may not end up in the same dense gas reservoirs. In addition, the ejecta of SNRs are not spatially homogeneous (Grefenstette et al., 2014). Both observational (DeLaney et al., 2010) and simulation (Wongwathanarat et al., 2015) results indicate that iron-group elements may be preferentially ejected in a particular direction. If the pre-solar cloud was not in this narrow window, it would receive far less ^{60}Fe than predicted, and a SN may still be the injection source.

4.5.3 Other considerations

We do not consider the evolution of the SN progenitor prior to explosion. The progenitor's stellar wind and ionizing radiation will shape the circumstellar environment, resulting in a stratified medium ($\rho \propto r^2$) rather than a uniform medium. This density gradient will affect the transit of the shock wave and grains through the intervening gas. Furthermore, the stellar wind will contain dust grains that may also be enriched with certain SLRs, such as ^{26}Al, produced during main sequence and post-main sequence evolution (Limongi & Chieffi, 2006; Palacios et al., 2005). These enriched dust grains will be swept up by the passage of the subsequent SNR and may further enhance SLR enrichment (Gounelle & Meynet, 2012).

We consider only one set of parameters for the SN (explosion energy $E_{\rm SN} = 10^{51}$ erg and ejected mass $M_{\rm ej} = 10$ M$\odot$) at a single distance ($d = 18$ pc). The SN parameters are somewhat constrained and only slightly affect the initial condition. The SN distance is limited by the estimated SLR yield of SNe, the geometric dilution of ejecta, and the radioactive decay of SLRs. As noted in Section 4.2.1, our chosen separation is at the upper limit of the 'radioactivity distance' for ^{26}Al enrichment (Looney et al., 2006). Reducing the distance from the SN to the pre-solar cloud may increase injection due to decreased geometric dilution, increased shock speed at impact, decreased time for radioactive decay of SLRs, and decreased sputtering. Therefore our estimates may be considered a lower limit in

this regard.

We also only consider a single SN. However, most massive stars form in clustered environments, e.g. OB associations (Lada & Lada, 2003), and in multiple systems (Zinnecker & Yorke, 2007). Indeed, it is likely that multiple SNe over one or more generations contributed SLRs to the pre-solar cloud (Vasileiadis et al., 2013; Young, 2014).

Cloud morphology may also play a considerable role in gas injection. We introduce static, clumpy substructure in the target cloud. The substructure prevents a symmetric stand-off shock from forming after impact and provides diffuse channels for injection through the dense filaments. The break-up of the shock also generates turbulence and mixing. We have neglected dynamical perturbations (velocity substructure); however, molecular clouds are probably turbulent (Elmegreen & Scalo, 2004), and introducing turbulence could further enhance the mixing at the cloud surface and increase injection of the smaller grains and gas.

We do not include gravity in our simulations. The potential effect of gravity can be estimated by comparing the local free-fall time $t_{\rm ff} = [3\pi/(32G\rho)]^{1/2}$ to the simulation time. For the dense clumps with $n_{\rm cl} \approx 400$ cm^{-3}, $t_{\rm ff} \approx 2$ Myr – much longer than the time-scales considered here (0.3 Myr). However, we note that compression by the SN shock wave, as well as fragmentation due to thermal instability, will create higher densities and may trigger collapse. Due to the global nature of our simulation, we are limited to measuring injection efficiencies at large scales within the cloud. Following the enrichment and mixing down to individual pre-stellar cores (sub-parsec scale) will require gravity and additional resolution (possibly through mesh refinement). While the densest gas is harder to penetrate, collapsing cores could receive SLRs by accreting enriched diffuse gas during collapse (Kuffmeier et al., 2016).

In our dust drag law, we consider only neutral grains and ignore the Coulomb drag force [second term in equation 4 of Draine & Salpeter (1979)]. However, dust grains will be charged by collisions with ions (Draine & Salpeter, 1979). The Coulomb term will become large when the relative velocity approaches the sound speed and may significantly affect the

grain dynamics at low relative velocities. Within the SNR, the dust-to-gas relative velocity is low and the gas temperature is high; hence the Coulomb (plasma) drag may be several times larger than the collisional drag (fig. 2, Bocchio et al., 2016). Reducing the dust grain velocities may reduce the injection, and therefore our estimates of enrichment may be upper limits. Charged grains will also interact with any magnetic fields present in the gas, which we neglect. Within the SN ejecta, the dust grains may be largely unaffected by magnetic effects, as there is observational and numerical evidence that the field is radially aligned (Dunne et al., 2009; Reynoso et al., 2013; Inoue et al., 2013). However, the field orientation may shift at the SN shock front; as noted by Foster & Boss (1997), gas–grain de-coupling may be suppressed or even prevented by fields in the shock front, which could drastically reduce the enrichment. Magnetic effects could also alter the grain dynamics within the target cloud. The average magnetic field increases with column density in dense molecular gas (Crutcher, 2012); hence the effect on grains also increases near star-forming clumps. Future work on the subject should consider the combined effects of grain charging, Coulomb drag, and magnetic fields.

4.6 Conclusions

A nearby supernova (SN) remains a possible candidate as the source of short-lived radioisotopes (SLRs) in the early solar system (ESS). The main challenge in this "direct injection" scenario is overcoming the impedance mismatch between the hot, diffuse supernova remnant (SNR) gas and the cold, dense pre-solar gas, as demonstrated amply in the literature (Boss & Keiser, 2012; Gritschneder et al., 2012; Pan et al., 2012). We explore whether dust grains formed from the SN ejecta and carrying SLRs can overcome the mixing barrier and enrich dense (potentially star-forming) gas. Using hydrodynamical simulations, we model the interaction of a SNR carrying dust grains with the pre-solar molecular cloud. We follow dust grains of varying initial radius ($a = 0.01$–10 μm) subject to drag forces and sputtering. We find the following points:

1. Sufficiently large dust grains ($a \geq 1$ μm) entrained in the SN ejecta will decouple from the shock front and survive entry into the molecular cloud. They will then be either completely stopped or sputtered, enriching the dense gas with SLRs within 0.1 Myr of the SN explosion.

2. Smaller dust grains ($a \leq 0.1$ μm) formed in the SN ejecta will be either stopped or sputtered before impacting the molecular cloud. The sputtered SLRs will contribute to the enrichment through subsequent gas-phase mixing.

3. Gas-phase SN ejecta will enrich the leading edge of molecular cloud only after instabilities develop at the cloud surface. The degree of mixing depends strongly on the inclusion of radiative cooling.

While it is still unknown what fraction of dust grains survive passage by the reverse shock and emerge from the SNR, we show that any surviving dust will contribute favorably to the typical SN enrichment scenario. Indeed, if a significant amount of large ($a \gtrsim 1$ μm) grains survive, dust may be the dominant source of SLR enrichment in nearby molecular clouds. Most notably, the dust grain enrichment occurs rapidly, in contrast with the typical gas-phase mixing which relies on the growth of hydrodynamical instabilities at the cloud surface. A shorter time delay between production and injection of the SLRs prevents substantial radioactive decay. Finally, if the various SLRs condense into different-sized dust grains, drag and sputtering will lead to a spatial stratification of SLRs within the pre-solar cloud. This could explain the large discrepancy in the ^{60}Fe/^{26}Al mass ratio between SN predictions and meteoritic measurements. We conclude that dust grains can be a viable mechanism for the transport of SLRs into the pre-solar cloud.

CHAPTER 5: DEUTERIUM FRACTIONATION OF MASSIVE PRE-STELLAR CORES[1]

5.1 Introduction

Massive stars played a central role in enriching the early solar system with SLRs, yet the physical processes and conditions involved in massive star formation remain uncertain (Tan et al., 2014). The relative rarity of massive stars and thus their typical large distances from us, along with their deeply embedded formation environments, make it difficult to observe details of the massive star formation process. The timescale for the formation of massive stars could constrain the enrichment of nearby low-mass systems (such as the solar system); a significant delay between molecular cloud formation and the onset of star formation would decrease the likelihood of local enrichment. In Goodson et al. (2016a), we explore the timescale and physical conditions of massive star formation with 3D magnetohydrodynamical observations. We include an approximate deuterium chemistry model to enable comparisons with recent observations of deuteration in massive, pre-stellar cores (Kong et al., 2016).

5.1.1 Massive Star Formation

There are two main theories for massive star formation: 1) Core Accretion models, e.g., the Turbulent Core Accretion model (McKee & Tan, 2003, hereafter MT03), which assumes near-virialized starting conditions for relatively ordered collapse; and 2) the Competitive Accretion model (Bonnell et al., 2001), which posits fragmentation and subsequent accretion by multiple stars from a turbulent, globally collapsing medium. Distinguishing these two

[1]Portions of this chapter previously appeared as an article in The Astrophysical Journal. The original citation is as follows: Goodson, M. D., Kong, S., Tan, J. C., Heitsch, F., & Caselli, P. "Structure, Dynamics, and Deuterium Fractionation of Massive Pre-Stellar Cores," The Astrophysical Journal, 833:274 (18pp), 2016 December 20.

scenarios relies on disentangling the numerous physical processes involved, such as turbulent motions, magnetic fields, and feedback.

Numerical modeling is one means to extricate the various processes. Previous simulations of massive star formation have focused on the role of turbulence, magnetic fields, and radiation in clump fragmentation. Girichidis et al. (2011) investigated the fragmentation of hydrodynamic clumps, examining the effect of the initial density profile and turbulent driving. The authors found that single massive stars are more likely to form from centrally-concentrated initial conditions, while the details of the turbulence are relatively unimportant. Numerous authors (Krumholz et al., 2007, 2010; Peters et al., 2011; Cunningham et al., 2011; Commerçon et al., 2011; Myers et al., 2013) have demonstrated that radiative feedback from protostars inhibits fragmentation of the clump. Magnetohydrodynamics (MHD) simulations both neglecting radiation (Hennebelle et al., 2011; Seifried et al., 2011, 2012) and with radiation (Peters et al., 2011; Commerçon et al., 2011; Myers et al., 2013) indicate that even a weak magnetic field suppresses clump fragmentation, and increasing the field strength further reduces the fragmentation.

In all of the aforementioned MHD numerical studies, the magnetic field strength is initially super-critical, i.e., the field cannot prevent gravitational collapse. The central pre-stellar core contracts rapidly, forming a protostar within one to two free-fall times. Yet the timescale of core collapse remains an open question. In the Competitive Accretion model, cores form and rapidly collapse on the order of the free-fall time. In the Turbulent Core model, the cores persist longer – at least one dynamical time – possibly supported by magnetic fields and turbulence near virial balance. Indeed, some observed cores exhibit supersonic linewidths consistent with virial balance (Tan et al., 2013; Kong et al., 2017). Yet, velocity dispersions due to virial equilibrium or energy equipartition (consistent with free-fall) differ only by a factor of $\sqrt{2}$ (Vázquez-Semadeni et al., 2007). Therefore, even a clear distinction between virial equilibrium and free-fall collapse based on velocity dispersion seems difficult. However, we note that where they have been measured, observed infall speeds

generally seem to be small, i.e., $\sim 1/3$ of the free-fall velocity (Wyrowski et al., 2016).

5.1.2 Deuteration as a Chemical Clock

An alternative means to probe the age and state of starless cores is using chemical tracers, in particular deuterated molecules. In sufficiently dense ($n_{\rm H} > 10^5$ cm^{-3}), cold ($T < 20$ K) environments, CO freeze-out opens a pathway for ion-neutral reactions that increase the deuterium fraction, i.e., the ratio of deuterated to non-deuterated species, $D_{\rm frac}$. For a full review of deuteration processes, see Ceccarelli et al. (2014). Observationally, deuterated molecules are excellent probes of pre-stellar gas. Caselli et al. (2001) traced low-mass star forming regions with N_2D^+ and DCO^+, finding deuterium fractions $D_{\rm frac} \gtrsim 0.1$, several orders of magnitude above the cosmic deuterium ratio (D/H $\sim 10^{-5}$). Similarly, Tan et al. (2013, hereafter T13) identified high-mass star-forming regions in infrared dark clouds (IRDCs) with the same deuterated molecules. Kong et al. (2016, hereafter K16) has subsequently estimated the deuterium fraction of N_2H^+ in these regions to be of comparable values to those in low-mass pre-stellar cores ($D_{\rm frac}^{\rm N_2H^+} \equiv N_2D^+/N_2H^+ \gtrsim 0.1$) (see also Fontani et al., 2011).

As deuteration is expected to begin only when pre-stellar core conditions are satisfied, the deuterium fraction may be a useful estimator of core age. Kong et al. (2015, hereafter K15) developed a time-dependent astrochemical network to model the evolution of deuterium-bearing molecules. The authors followed the chemistry in a single zone with fixed physical conditions or with simple density evolution. Under typical core conditions, the K15 models suggest that the deuteration process is slow, with up to ten free-fall times required to reach the observed values of $D_{\rm frac}^{\rm N_2H^+}$.

Moving beyond single-zone chemical models is a difficult task, as the complex reaction network requires extensive computational resources. Pagani et al. (2013) coupled the deuterium network of Pagani et al. (2009) with a 1D spherically-symmetric hydrodynamic calculation. The simulations followed deuteration in 200 radial zones during collapse of a

low-mass pre-stellar core from a uniform, static state. In disagreement with K15, Pagani et al. (2013) determined that fast collapse is preferred, as steady-state abundances determined from the model were typically much higher than observed. However, the models of Pagani et al. (2009) and Pagani et al. (2013) begin with very high initial depletion factors, which greatly shortens the deuteration timescale. A full discussion and comparison is presented in K15, but it is worth noting that, given similar initial conditions, the models of K15 agree with Pagani et al. (2009) to within a factor of 3.

If large-scale magnetic fields are present, the assumption of radial symmetry during collapse will not hold, as flux-freezing prevents significant collapse in directions perpendicular to the field. Further, the turbulent motions within the core are not fully captured in 1D simulations. Indeed, the chemical evolution may be altered by non-linear effects such as density fluctuations and turbulent diffusion. Implementing a full chemical network in high-resolution 3D simulations is currently not feasible given computational limits. One option may be to reduce the number of reactions and reactants; however, this would negatively affect the accuracy of the chemistry. Here, we develop an alternative approach.

We construct an approximate deuterium chemistry model built on the full astrochemical network results of K15. By parameterizing the results across a wide range of densities, we formulate a robust and efficient method to follow the growth and deuteration of N_2H^+ in 3D MHD simulations of massive core collapse. We generate a turbulent, magnetized pre-stellar core according to the paradigm of MT03, and we model the collapse of the core until the first protostar forms. We simultaneously follow the chemical evolution of N_2H^+ and N_2D^+ and compare to observed massive pre-stellar cores. By varying the initial conditions, such as the mass surface density, magnetic energy, chemical age, and initial ortho-to-para ratio of H_2, we can estimate the core properties necessary to match observed deuterium abundances.

We observe in our simulations that the collapse occurs on roughly the free-fall time, regardless of the initial mass surface density or magnetic field strength. We conclude that reaching the observed deuterium fractions requires significant prior chemical evolution, low

initial ortho-to-para ratio, and/or slower collapse, possibly by stronger magnetic fields or sustained turbulence.

We outline our numerical methods, including initial conditions and chemical model in (Section 5.2). The results of our simulations are presented and discussed in Section 5.3. We discuss the implications for massive star formation in Section 5.4 before concluding in Section 5.5.

5.2 Methods

We use a modified version of Athena (Stone et al., 2008) version 4.2 to solve the equations of ideal, inviscid MHD given by Eqs. 2.1.1–2.1.5. We include a passive color field C to trace core material, whose evolution is given by Eq. 2.1.6. We also evolve several scalar fields to trace the chemistry:

$$\frac{\partial \rho [X]}{\partial t} + \nabla \cdot (\rho \mathbf{u} [X]) = S([X]) \tag{5.2.1}$$

with the fractional abundance $[X]$ for some species X relative to hydrogen, and a source term S. Full details of the chemical model are presented in Section 5.2.2.

We use the directionally unsplit van Leer (VL) integrator (Stone & Gardiner, 2009) with second order reconstruction in the primitive variables (Colella & Woodward, 1984) and the HLLD Riemann solver (Toro, 2009). Simulations are performed on Cartesian grids in three dimensions. To obtain an approximately isothermal equation of state, we set the ratio of specific heats $\gamma = C_P/C_V = 1.001$. We do not include radiation pressure or feedback; we do include self-gravity.

5.2.1 Setup and Initial Conditions

We initialize a spherical core according to the relations of MT03. We set the core mass $M_{\rm c} = 60$ M$_\odot$ and the density power law exponent $k_\rho = 1.5$. For our fiducial core, we set the

Table 5.1: Summary of turbulent core simulations. Fiducial simulation is S3M2.

Run Name	$\Sigma_{\rm cl}$ (g cm^{-2})	μ_Φ	$M_{\rm c}$ ($M_\odot$)	$R_{\rm c}$ (pc)	$\bar{n}$ (cm^{-3})	$t_{\rm ff}$ (kyr)	$B_{\rm c}$ (mG)	α	σ (km s^{-1})	δ (AU)
S3M2	0.3	2	60	0.104	1.97×10^5	76	0.803	2	0.99	213
S1M2	0.1	2	60	0.180	3.79×10^4	173	0.268	2	0.76	365
S3M1	0.3	1	60	0.104	1.97×10^5	76	1.606	2	0.99	213
S1M1	0.1	1	60	0.180	3.79×10^4	173	0.536	2	0.76	365

clump mass surface density $\Sigma_{\rm cl} = 0.3$ g cm^{-2}, consistent with the estimates of T13 observed cores. With these values, MT03 prescribes the radius of the core

$$R_{\rm c} = 0.057 \left(\frac{\Sigma_{\rm cl}}{1 \text{ g cm}^{-2}}\right)^{-1/2} \text{pc} \rightarrow 0.10 \text{ pc} \tag{5.2.2}$$

and the number density of hydrogen at the surface

$$n_{{\rm H},s} = 1.16 \times 10^6 \left(\frac{\Sigma_{\rm cl}}{1 \text{ g cm}^{-2}}\right)^{3/2} \text{cm}^{-3} \rightarrow 1.82 \times 10^5 \text{ cm}^{-3}, \tag{5.2.3}$$

where the value after the arrow is for the fiducial model. The mean number density in the core is $\bar{n} = 1.97 \times 10^5$ cm^{-3}, and the average free-fall time of the core is

$$t_{\rm ff} = \sqrt{\frac{3\pi}{32 G \bar{\rho}}} \rightarrow 76 \text{ kyr}, \tag{5.2.4}$$

with average density $\bar{\rho} = \bar{n}\mu m_{\rm H}$, the mean molecular weight $\mu = 2.33$, and the mass of hydrogen $m_{\rm H}$. To trace the core, we initialize the passive color field C to unity for $r \leq R_{\rm c}$ and zero otherwise. We also perform simulations with lower initial mass surface density of the surrounding clump ($\Sigma_{\rm cl} = 0.1$ g cm^{-2}); the relevant parameters for both cases are summarized in Table 5.1.

Density Structure

The core has a density profile $\rho(r) \propto r^{-1.5}$, which is consistent with observations of massive pre-stellar cores (Butler & Tan, 2012). We set the core to a constant temperature

$T_c = 15$ K; thus the thermal pressure in the core follows the same power law as the density. The sound speed in the core $c_s = \sqrt{k_B T/(\mu m_H)} = 0.2$ km s^{-1}, with the Boltzmann constant k_B. To prevent divergence as $r \to 0$, we flatten the profile over an inner radius, $R_f = 0.15 R_c$. We calculate the central density $n_c = n_s[1.0 + (R_c/R_f)^{k_\rho}] \to 1.99 \times 10^6$ cm^{-3}. We impose an order of magnitude jump in the density at the core surface, which is smoothed by a hyperbolic tangent profile with $R_s = 0.05 R_c$. The density in the ambient medium is constant at $n_0 = 0.1 n_s$. The overall density profile is given by

$$n(r) = n_0 + \frac{n_c - n_0}{1 + (r/R_f)^{k_\rho}}(0.5 - 0.5 \tanh[\frac{r - R_c}{R_s}]). \tag{5.2.5}$$

The ambient temperature T_0 is determined by thermal pressure balance with the core: $T_0 = 10 T_c = 150$ K. This mimics the effective pressure of the surrounding clump medium, which is expected to be dominated by non-thermal mechanisms, e.g., turbulence. The actual temperature of the clump is expected to be quite similar to that of the core.

The core is centered in a cubic simulation box of side length $L = 5 R_c \to 0.52$ pc with spatial resolution $\delta = L/512 \to 213$ AU. We use periodic boundary conditions to prevent gravitational evacuation at the box edges; the core is sufficiently padded to prevent any interactions with the boundaries. We use a periodic FFT solver to calculate the gravitational potential. Eventually runaway collapse in a few cells drives the global time-step to nearly zero. The collapse could be followed longer by the addition of sink particles, but as we are only interested in pre-stellar conditions, we terminate the simulation at this point.

Magnetic Fields

We initialize a cylindrically-symmetric magnetic field in the z-direction, similar to the field geometry of Myers et al. (2013). The field strength is determined by the desired mass-to-flux ratio normalized to the critical value (Mouschovias & Spitzer, 1976):

$$\mu_\Phi = \frac{M}{M_\Phi} = \frac{2\pi G^{1/2} M}{\Phi}, \tag{5.2.6}$$

where M_Φ is the critical mass-to-flux value and Φ is the magnetic flux through the center of the core. To maintain approximately constant μ_Φ throughout the core, the field strength decreases as $r^{-0.5}$; then the magnetic pressure $B^2/(8\pi) \propto r^{-1}$, as in MT03. For a given μ_Φ, we calculate the field strength at the surface of the core $B_{\rm s}$:

$$B_{\rm s} = \frac{3}{2}\frac{G^{1/2}M_{\rm c}}{\mu_\Phi R_{\rm c}^2} \rightarrow 0.22 \text{ mG}. \tag{5.2.7}$$

Similar to our treatment of the density, we smooth the magnetic field profile both at the center of the core and at the edge of the core. The field in the ambient medium is uniform at $B_0 = B_{\rm s}$, and the overall magnetic field profile is given by

$$B(\xi) = B_0 + \frac{B_{\rm c} - B_0}{1 + (\xi/R_{\rm f})^{0.5}}(0.5 - 0.5\tanh[\frac{\xi - R_{\rm c}}{R_{\rm s}}]), \tag{5.2.8}$$

where $\xi \equiv \sqrt{x^2 + y^2}$ is the distance from the z-axis and $B_{\rm c}$ is the central field strength, given by $B_{\rm c} = B_{\rm s}[1.0 + (R_{\rm c}/R_{\rm f})^{0.5}]$. Our fiducial simulation uses a slightly super-critical mass-to-flux ratio ($\mu_\Phi = 2$), in accord with observations of dense molecular gas (Crutcher, 2012); then the central field strength $B_{\rm c} \rightarrow 0.80$ mG. We also perform simulations with a stronger magnetic field, corresponding to critical mass-to-flux ratio ($\mu_\Phi = 1$). Relevant parameters in both cases are summarized in Table 5.1.

Turbulence

We initialize supersonic turbulence in the cores with random velocity perturbations. The turbulence is generated in a method similar to that described in Mac Low (1999): amplitudes are drawn from a random Gaussian with a Fourier power spectrum of form $|\delta \mathbf{v}_k| \propto k^{-2}$, with $1.0 < kL/2\pi < N/2$, where k is the wavenumber, L is the box size, and N is the number of cells. We apply fully solenoidal (divergence-free) perturbations. The initial perturbation has a one-dimensional velocity dispersion σ calculated from the virial relation, $\alpha \equiv 5\sigma^2 R_{\rm c}/(GM_{\rm c})$ (Bertoldi & McKee, 1992). Because we do not initialize any density perturbations, we set

the core to be initially super-virial ($\alpha = 2$); the initial velocity dispersion in the fiducial simulation is then $\sigma \rightarrow 0.99$ km s^{-1}. This value is close to the velocity dispersion of a virialized core including external pressure terms, given in T13:

$$\sigma_{\rm c,vir} = 1.09 \left(\frac{M_c}{60\ {\rm M}_\odot} \right)^{1/4} \left(\frac{\Sigma_{\rm cl}}{1\ {\rm gcm}^{-2}} \right)^{1/4} {\rm km\ s}^{-1} \rightarrow 0.80\ {\rm km\ s}^{-1}. \tag{5.2.9}$$

We do not drive the turbulence; energy is only injected at initialization.

5.2.2 Chemistry

We follow the evolution of two molecular species in our simulations: N_2H^+ and N_2D^+. The fractional abundance of each species is advected with the fluid as a passive color field (Eq. 5.2.1). We use an approximate chemical model based on the results of K15, in which the authors presented a time-dependent chemical network for the evolution of N_2H^+ and N_2D^+ in a single-zone approximation. We combine results from across the K15 parameter space into a unified model to predict the initial chemical abundances and growth rates.

In K15, the authors examined the influence of numerous physical conditions and found that the results depend strongly on the number density of hydrogen, $n_{\rm H}$, and the initial ortho-to-para ratio of H_2, $\mathrm{OPR}_0^{\mathrm{H_2}}$. Deuteration is most efficient when the number density is high and $\mathrm{OPR}^{\mathrm{H_2}}$ is low. Unfortunately, $\mathrm{OPR}^{\mathrm{H_2}}$ is not easy to estimate from observations. The statistical expectation for $\mathrm{OPR}^{\mathrm{H_2}}$ at H_2 formation on grains is $\mathrm{OPR}^{\mathrm{H_2}} = 3.0$; $\mathrm{OPR}^{\mathrm{H_2}}$ then decreases as ortho-H_2 is destroyed. We test the effect of different initial $\mathrm{OPR}^{\mathrm{H_2}}$ values by including three sets of K15 simulations: $\mathrm{OPR}_0^{\mathrm{H_2}} = 1.0$, 0.1, and 0.01.

For a given $\mathrm{OPR}_0^{\mathrm{H_2}}$, we use a suite of 55 uniform density models from K15 to construct our approximate model, spanning hydrogen number densities from 10^3 to 10^9 cm^{-3}. All models use the fiducial parameters of K15: gas temperature $T = 15$ K, cosmic ray ionization rate $\zeta = 2.5 \times 10^{-17}$ s^{-1}, heavy-element depletion factor $f_{\rm D} = 10$, radiation field (relative to Habing field) $G_0 = 1$, and visual extinction $A_V = 30$ mag. We note that, while $\zeta \approx 3 \times 10^{-16}$ s^{-1} in diffuse gas (Indriolo & McCall, 2012), cosmic rays are attenuated in dense

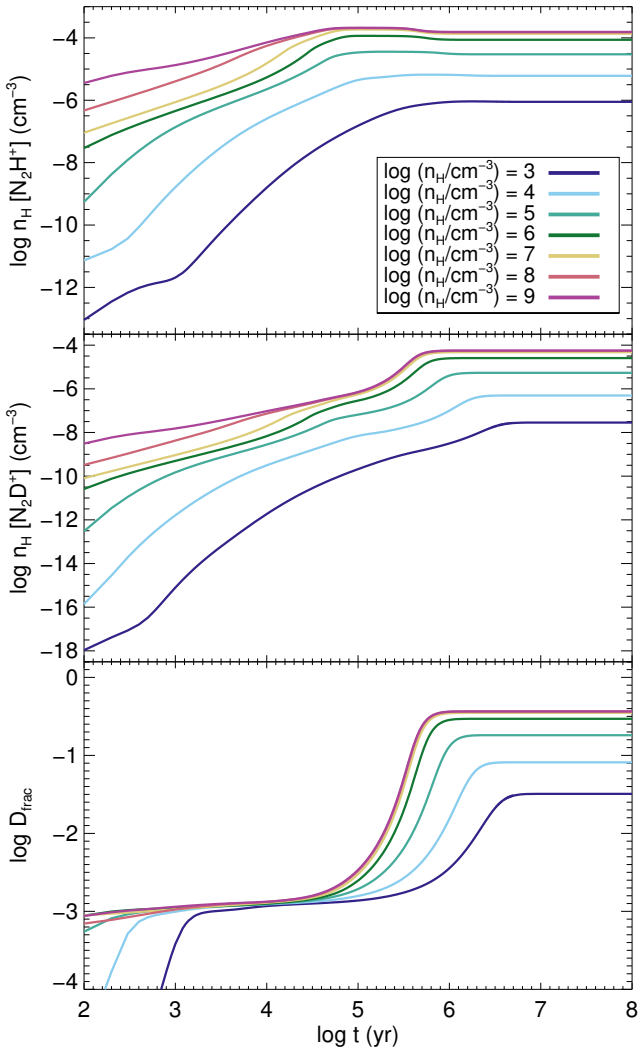

Figure 5.1: Time evolution of chemical number density and deuterium fraction from K15 for various hydrogen number densities $n_{\rm H}$. The number density is computed as $n_{\rm H}[X]$, where $[X]$ is the relative abundance of species X. From top to bottom, the number density of N_2H^+, of N_2D^+, and the deuterium fraction, $D_{\rm frac}^{\rm N_2H^+} \equiv N_2D^+/N_2H^+$. Results are obtained with K15 fiducial parameters except that $\mathrm{OPR}_0^{\rm H_2} = 0.1$. The time required to reach equilibrium decreases with increasing density. Additionally, the equilibrium values for both species abundance and the deuterium fraction increase with increasing density, reaching $D_{\rm frac}^{\rm N_2H^+} \gtrsim 0.3$ at $n_{\rm H} = 10^9$ cm^{-3}.

starless cores to a value approximately an order of magnitude lower (Padovani et al., 2009; Keto & Caselli, 2010). We also note that for these conditions of high extinction the radiation field plays a negligible role. Each K15 model provides the time evolution of the fractional abundance of species X, denoted $[X](t)$, over 100 Myr. Figure 5.1 presents the fiducial results of K15 for varying hydrogen number density $n_{\rm H}$ at $\mathrm{OPR}_0^{\mathrm{H_2}} = 0.1$, with the deuterium fraction $D_{\rm frac}^{\rm N_2H^+} \equiv \mathrm{N_2D^+/N_2H^+}$.

Chemical Age

To set the initial condition for the molecular abundances, we must make assumptions about the previous history of the gas. Deuteration begins as CO starts to freeze out, which occurred prior to $t = 0$ for our simulation; the exact amount of prior time is unknown. We therefore investigate four chemical starting times, $t_{\rm chem}$, which for simplicity we make multiples of the mean core free-fall time: $t_{\rm chem} = 0$, 1, 3, and 10 $t_{\rm ff}$. For $t_{\rm chem} = 0$, we assume $[\mathrm{N_2H^+}]$=$[\mathrm{N_2D^+}]$=0.0. For all other $t_{\rm chem}$, we reference the constant density runs of K15. We first interpolate the K15 results using a cubic spline onto an $n_{\rm H}$-t grid of 1000^2 support points. This finer grid then functions as a look-up table; given a particular starting time $t_{\rm chem}$ and density $n_{\rm H}$, we estimate the chemical abundances using bi-linear interpolation. This method implicitly assumes that the gas has been in its current configuration for the duration of $t_{\rm chem}$. While this is clearly an idealization, it provides a simple test of the importance of the previous history of the gas.

Chemical Growth Rates

The time evolution of each chemical species at a given density is provided by K15. From these runs, we can calculate a growth rate, $\mathrm{d}[X]/\mathrm{d}t$ as a function of time and density. If our simulations maintained a constant density, we could use the absolute time to determine the growth rate and easily evolve the abundances. However, in a dynamical simulation with non-linear density evolution, the time dependence is not straightforward. If we restrict the

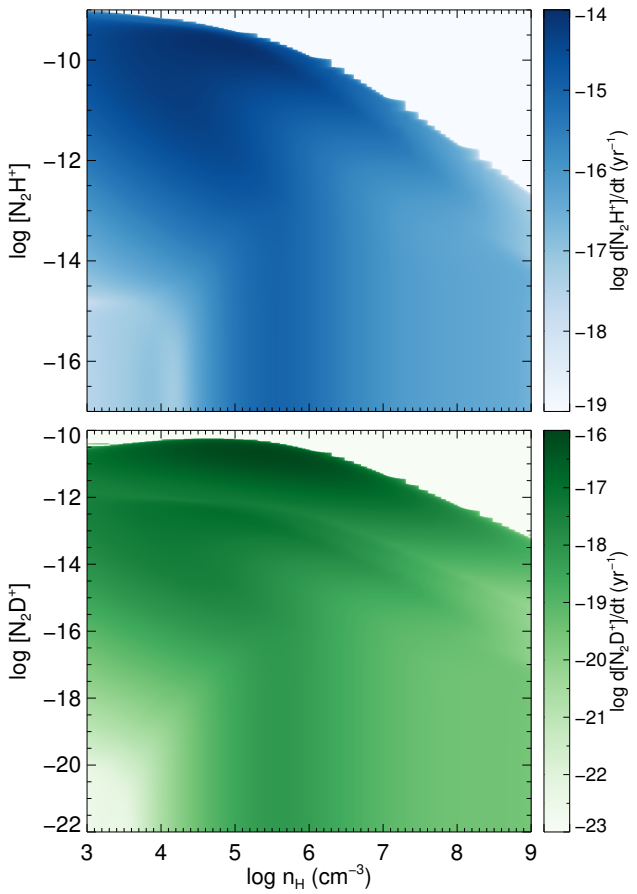

Figure 5.2: Example look-up grid for the chemical evolution of (top) $[N_2H^+]$ and (bottom) $[N_2D^+]$ in our simulation. The grid shown is for $OPR_0^{H_2} = 0.1$ and is generated from the chemical network modeling of K15. A growth rate $d[X]/dt$ is estimated for each species X using bi-linear interpolation based on the current hydrogen number density n_H and relative abundance $[X]$.

abundances to strictly grow monotonically, we can parameterize the chemical growth rate as a function of the chemical abundance itself and remove the time dependence. In the chemical modeling results of K15, $[N_2D^+]$ strictly monotonically increases, and $[N_2H^+]$ monotonically increases except for a slight decrease very near equilibrium. As the effect is relatively small ($\lesssim 30\%$), we ignore any decreases in chemical abundances. With this modification, we can parameterize the growth rate as a function of the current species abundance.

We calculate the time derivative as a function of chemical abundance for each of the constant-density runs performed in K15 using a second-order central difference. For computational efficiency, we then interpolate the results onto a 1000^2 n_H-$[X]$ look-up grid. Figure

5.2 shows an example grid for $\mathrm{OPR}_0^{\mathrm{H_2}} = 0.1$. For each cell and at each time step in the simulation, the growth rate is estimated by bi-linear interpolation based on the current density and fractional abundance. The total source term $S([X]) = \rho\ dt\ (d[X]/dt)$ is calculated using a sub-cycled fourth-order Runge-Kutta method and applied to the scalar field via operator-splitting. Numerical effects of the scalar field can potentially lead to fractional abundances larger than the equilibrium value; therefore, for each cell we calculate the equilibrium value for the current density and prevent the fractional abundance from exceeding this value.

Chemistry Tests

We validate our approximate chemical model by comparing to results from K15. We first compare simulations run with constant density. Overall, we find our approximate chemistry matches the full network calculations to within a few percent. As these models form the basis for our approximate method, it is reassuring that we match the evolution of all quantities accurately. We note that our parameterization leads to a systematic underestimate of the equilibrium values of $[\mathrm{N_2H^+}]$ and $D_{\mathrm{frac}}^{\mathrm{N_2H^+}}$, up to 30% below the values of K15. As discussed above, we need to make the growth rate a single-valued function of the current abundance, so we remove the slight decrease in $[\mathrm{N_2H^+}]$ near equilibrium.

We next compare to the Dynamic Density Evolution (DDE) simulations of K15. In these models, the authors used a single zone in which the hydrogen number density n_{H} evolved as

$$\frac{dn_{\mathrm{H}}}{dt} = \alpha_{\mathrm{ff}} \frac{n_{\mathrm{H}}(t)}{t_{\mathrm{ff}}(t)}, \tag{5.2.10}$$

where t_{ff} is the local free-fall time at the current density. Results are shown in Figure 5.3. Overall, the results agree to within 10% for most of the simulations. At early times, the short chemical time-scales are not well-resolved. Again, at late times the inability of $[\mathrm{N_2H^+}]$ to decrease leads to a systematic underestimate of $[\mathrm{N_2H^+}]$ and $D_{\mathrm{frac}}^{\mathrm{N_2H^+}}$.

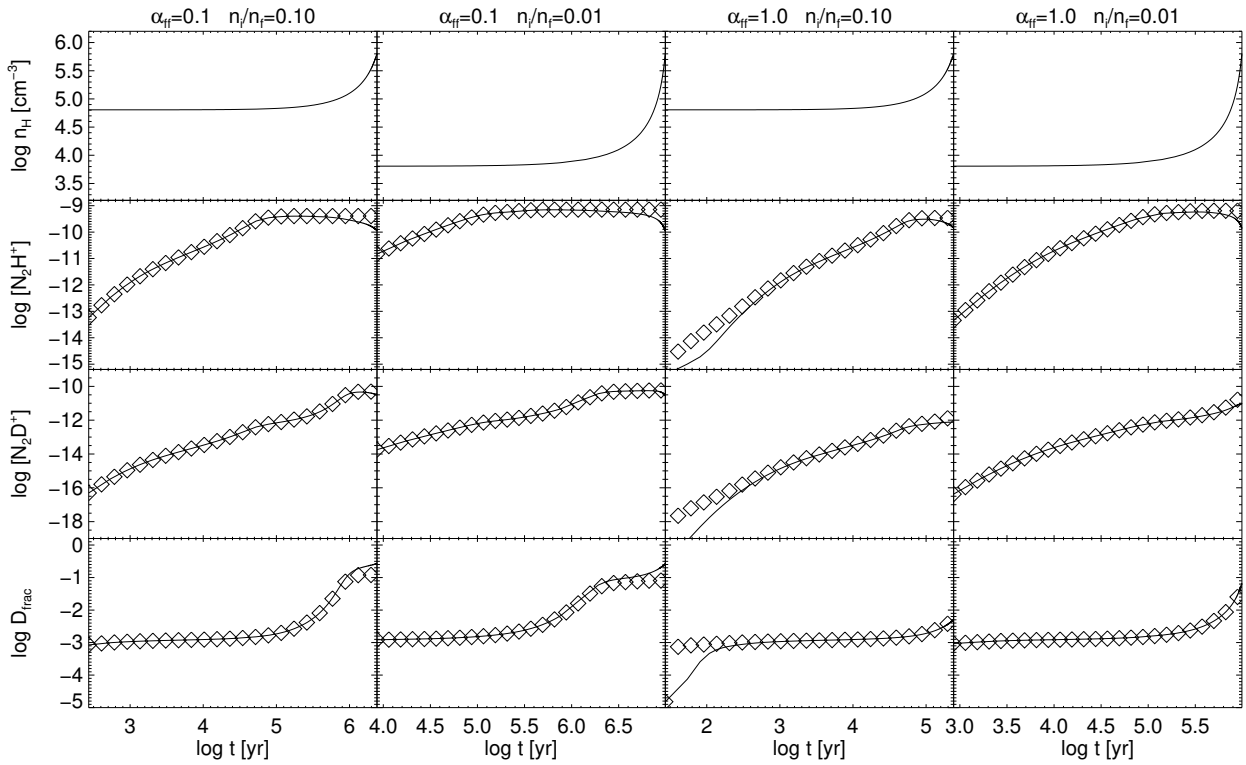

Figure 5.3: Comparison between K15 chemical network calculations (solid line) and our approximate chemical model in Athena (open diamonds) for Dynamic Density Evolution (DDE) tests. Each column shows a unique test case, with varying rates of collapse ($\alpha_{\rm ff}$) and density ratios ($n_{\rm i}/n_{\rm f}$). The evolution of the density (top row) is identical in both K15 and Athena; therefore no comparison is shown. Results are for $\mathrm{OPR}_0^{\mathrm{H_2}} = 0.1$. Overall, the results agree to within 30%, with the largest discrepancies at initialization, as the short chemical timescales are difficult to resolve. At late times, there is a small tendency to systematically overestimate N_2H^+, which can lead to an underestimation of $D_{\rm frac}^{\rm N_2H^+}$due to our parameterization method.

5.3 Results

5.3.1 Dynamical Evolution

We follow the collapse and chemical evolution of the fiducial simulation (run S3M2) for 61 kyr $\approx 0.8 t_{\rm ff}$. Figure 5.4 shows the time evolution of the mass surface density, mean velocity (weighted by the N_2D^+ abundance), and chemical tracers projected along the x-axis, perpendicular to the initial magnetic field orientation, as well as the ratio of the column densities ($D_{\rm frac}^{\rm N_2H^+} \equiv N[N_2D^+]/N[N_2H^+]$). For comparison to observations, we apply a density threshold when calculating the N_2H^+ and N_2D^+ column densities based on the $J = 3$–2 transition critical densities, which are given in table 2 of Miettinen & Offner (2013). For simplicity, we use a single value for both species of $n_{\rm crit}(3\text{–}2) \approx 4 \times 10^6$ cm^{-3}. However, emission still occurs at densities below $n_{\rm crit}$ (Evans, 1999), resulting in an effective critical density roughly an order of magnitude lower (Shirley, 2015); we therefore consider contributions to the chemical column densities only where $n_{\rm H_2} \geq n_{\rm eff} = 4 \times 10^5$ cm^{-3}. The density-weighted plane-of-sky magnetic field projection is overlaid on the mass surface density map.

The initial turbulent velocity field disrupts the smooth density distribution. The external pressure prevents significant expansion, and the core begins to collapse due to gravity. As these are ideal MHD simulations, the magnetic field in the z-direction prevents significant collapse along the perpendicular directions due to flux-freezing. Material can freely collapse along the field lines, creating an elongated filamentary structure in the x-y plane. We follow the evolution of the core until runaway gravitational collapse into a few central cells prevents further evolution; this is essentially the formation of the first protostar. As seen in Figure 5.4, the core collapses monolithically with little fragmentation, and the density appears to be centrally concentrated at termination. The magnetic field structure eventually develops an hourglass morphology as the field lines are pulled inward at the midplane.

The asymmetry introduced by the magnetic field suggests the viewing angle will be important. Figure 5.5 shows projections taken along the z-axis, parallel to the initial field

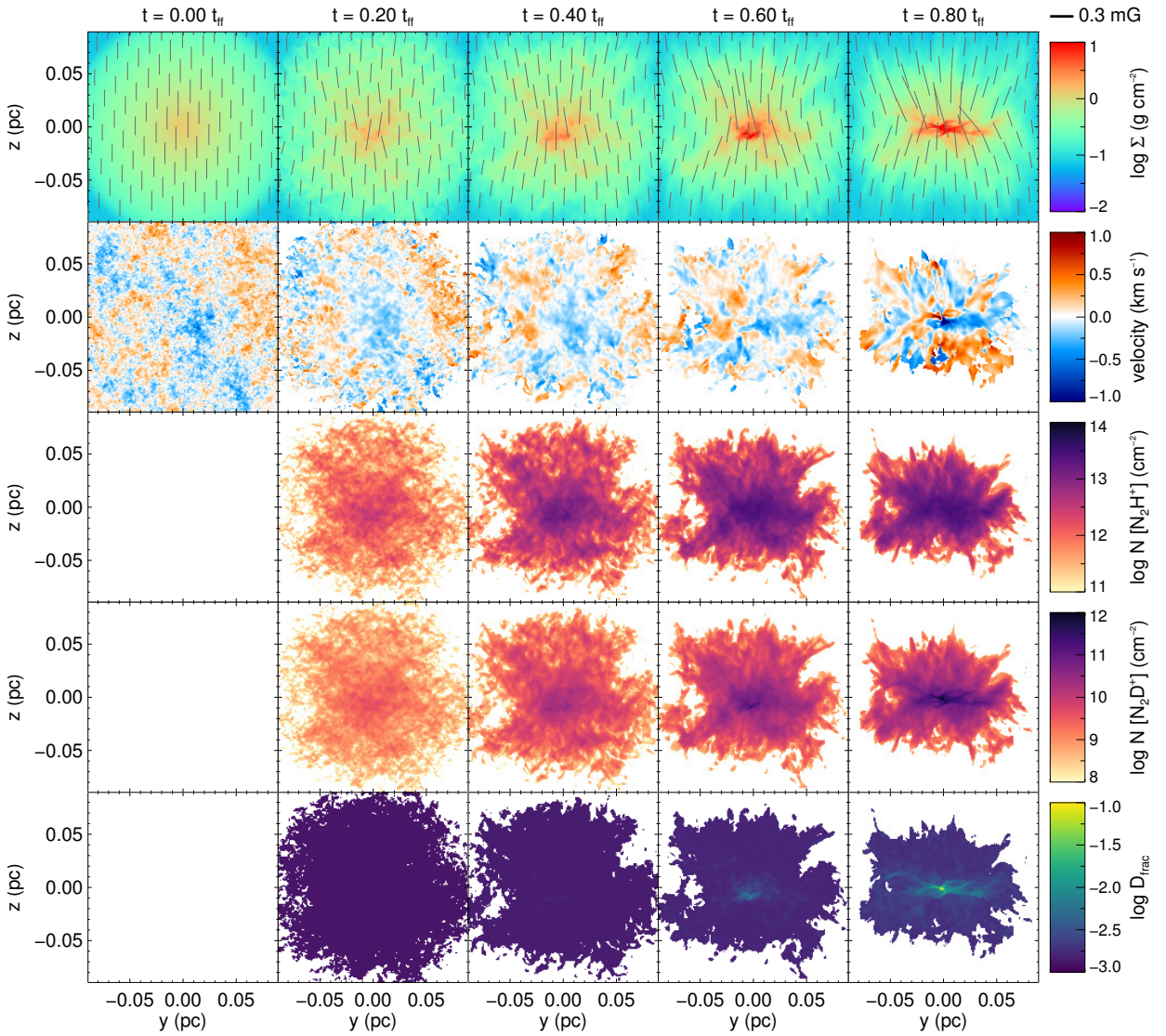

Figure 5.4: Projections from our fiducial turbulent, magnetized core model (run S3M2). Time proceeds from left to right in units of the initial mean free-fall time $t_{\rm ff}$. From top to bottom, the rows are: the mass surface density Σ; the mean velocity along the line of sight weighted by N_2D^+; the column density of N_2H^+; the column density of N_2D^+; and the deuterium fraction $D_{\rm frac}^{\rm N_2H^+}$. The chemical starting time $t_{\rm chem} = 0$ $t_{\rm ff}$ and the initial ortho-to-para ratio of H_2 $\mathrm{OPR}_0^{\rm H_2} = 0.1$. Projections are taken along the x-axis, perpendicular to the initial magnetic field direction. The density-weighted magnetic field projection in the plane-of-sky is overlaid on the mass surface density in black lines, with the length proportional to the field strength. For reference, the length corresponding to $B = 0.3$ mG is shown in the top right. The chemical tracers are only considered where the molecular hydrogen number density is greater than $n_{\rm eff} = 4 \times 10^5$ cm^{-3}, roughly 10% of the critical density for the (3–2) transition. As $[N_2D^+]$=0 at t=0, we instead show the density-weighted mean velocity for that panel only.

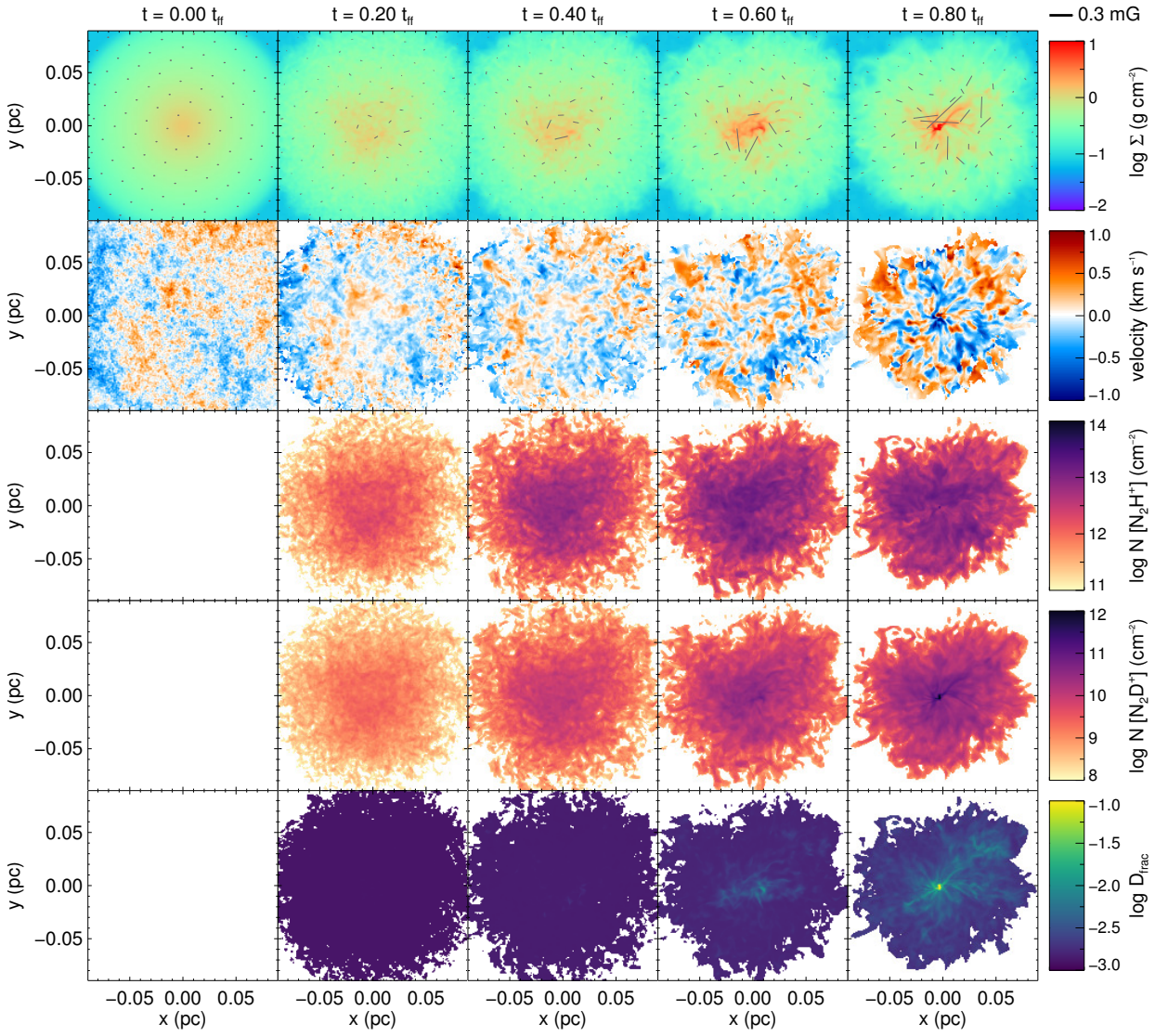

Figure 5.5: Same as Figure 5.4, but now the projection is taken along the z-axis, parallel to the initial field direction.

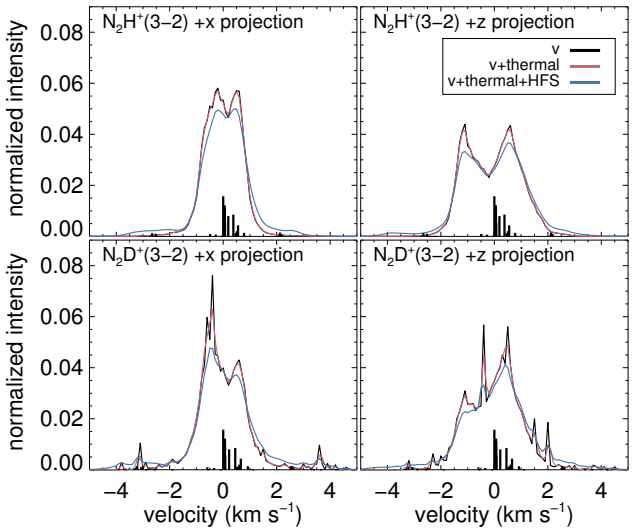

Figure 5.6: "Spectra" of the total emission from N_2H^+(3–2) (top row) and N_2D^+(3–2) (bottom row) in run S3M2 at simulation termination, for line-of-sight velocities parallel (left column) and perpendicular (right column) to the magnetic field. The velocity binsize is 0.1 km s^{-1}. Assuming the gas is optically thin, we weight the velocities with the abundance of the tracer species. The black line shows the unprocessed distribution; the red line shows the effect of thermal broadening at $T = 15$ K; and the blue line includes both thermal and hyperfine structure (HFS) broadening. For reference, the normalized HFS intensities are shown in black at the bottom of each panel.

orientation. The core now appears circular, suggesting a disk-like structure in the x-y plane. More small-scale structure is visible, as the velocity perturbations tangle and amplify the plane-of-sky magnetic field in the core; however, the central condensation remains distinct, surrounded by less-dense filaments or streams.

In the mean velocity map at $t = 0.8t_{\rm ff}$ in Figure 5.4, there is a velocity gradient of several km s^{-1} across the central condensation, suggesting rotation in the x-y plane. This is further evidenced in the velocity "spectra" shown in Figure 5.6, which all exhibit a double-peaked distribution. The spectra are computed from the integrated intensity of N_2H^+(3–2) and N_2D^+(3–2) assuming LTE optically-thin emission ($j_X \propto n[X]$). To examine the effect of different broadening mechanisms, Figure 5.6 presents the abundance-weighted velocity distribution with no broadening (black line), with thermal broadening at $T = 15$ K (red line), and with hyperfine structure (HFS) broadening (where each component has the same Gaussian profile with a thermal velocity dispersion corresponding to $T = 15$ K; blue line).

The thermal velocity dispersion is sufficiently small ($\sigma_X \approx 0.06$ km s^{-1}) that the broadening has only a modest effect. The projection direction has a pronounced effect, as the dispersion in the $+z$-direction (parallel to the magnetic field) is much wider than in the $+x$-direction. This may be attributed to material collapsing freely along the magnetic field lines. There are also noticeable differences between the N_2H^+ and N_2D^+ spectra; the N_2D^+ spectra exhibit more small scale structures than the N_2H^+. As will be discussed in Section 5.3.2, N_2H^+ largely reaches equilibrium throughout the core, whereas N_2D^+ does not; N_2D^+ may therefore probe smaller and denser structures within the core.

T13 assessed the virial state of observed pre-stellar cores by comparing the velocity dispersion of N_2D^+(3–2), $\sigma_{N_2D^+}$, to the predictions for a virialized core based on MT03, $\sigma_{c,vir}$ (Eq. 5.2.9). We present a similar analysis in Figure 5.7. At each time step, we calculate the projected area in which N_2D^+(3–2) emission is present, then ascribe an equivalent area circle to determine the effective core radius $R_{c,eff}$. The clump mass surface density Σ_{cl} is then determined within the annulus from R_c to $2R_c$. To match the observations of T13, the effective core mass is determined from the projections in two ways: 1) the total mass surface density Σ is summed within the equivalent area to compute the maximum core mass $M_{c,max}$; 2) the clump surface density is subtracted from the total mass surface density before summing to compute the minimum core mass $M_{c,min}$, removing contributions from the foreground and background to the core mass. The velocity dispersion of N_2D^+(3–2) is determined by fitting a Gaussian to the thermally-broadened spectrum computed along each Cartesian projection direction. For comparison, we also show the velocity dispersion calculated from the core color tracer (σ_c), which should represent the actual velocity dispersion of the core. Finally, the clump mass surface density and minimum core mass are used to estimate the velocity dispersion of a virialized core, $\sigma_{c,vir}$ (Eq. 5.2.9), compared to $\sigma_{N_2D^+}$ and σ_c.

In the fiducial run, the effective radius decreases as the core collapses. The effective core mass also decreases due to the central concentration of the N_2D^+ tracer. The core is initialized with a velocity dispersion $\sigma = 1$ km s^{-1}; yet by $t = 0.1t_{ff}$, $\sigma \approx 0.4$ km s^{-1}.

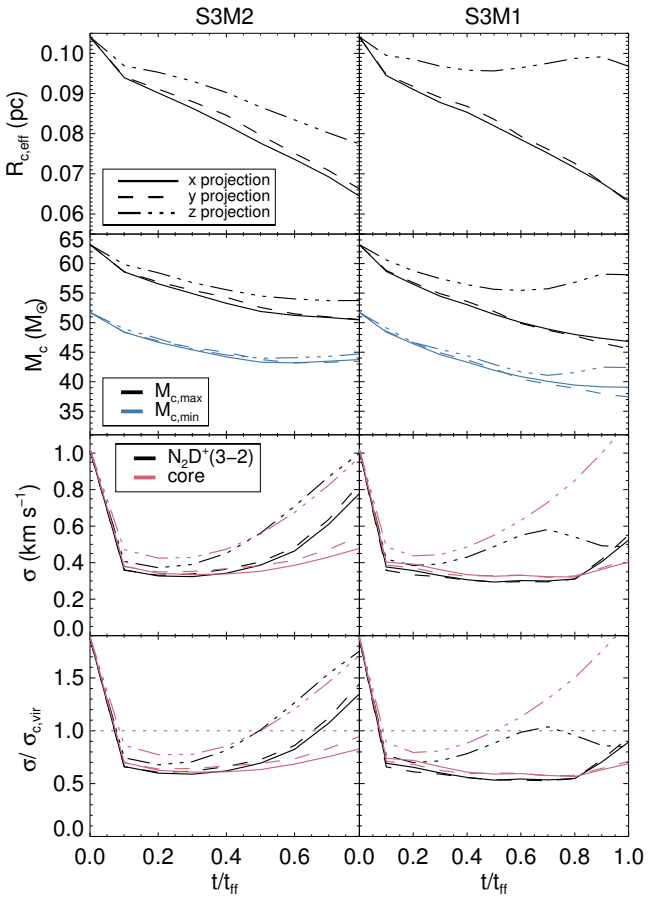

Figure 5.7: Time evolution of T13 observed quantities in runs S3M2 (left column) and S3M1 (right column). The rows show, from top to bottom: the effective core radius $R_{\rm c,eff}$; the core mass determined both with the clump contribution ($M_{\rm c,max}$; black) and without ($M_{\rm c,min}$; blue); the one-dimensional velocity dispersion of N_2D^+(3–2) ($\sigma_{\rm N_2D^+}$; black) and core tracer color field ($\sigma_{\rm c}$; red); and the ratio of σ to the mass-averaged velocity dispersion of a virialized core $\sigma_{\rm c,vir}$, computed from Eq. 5.2.9 using the minimum core mass (using $M_{\rm c,max}$ instead results in a 5% increase in $\sigma_{\rm c,vir}$). σ is determined from the total thermally-broadened spectra projected along the three Cartesian lines-of-sight (solid: x-direction; dashed: y-direction; dash-dotted: z-direction). For reference, $\sigma/\sigma_{\rm c,vir} = 1$ is indicated with a dotted horizonatal line. As $[N_2D^+] = 0$ at $t = 0$, we show instead the total velocity dispersion for this data point only.

The velocity dispersion then increases most strongly in the z-direction, as material collapses freely along the magnetic field lines. As N_2D^+becomes concentrated in the densest regions of the core, it no longer traces the overall velocity distribution and diverges from the color field estimate. The cores analyzed in both T13 and Kong et al. (2017) were determined to be moderately sub-virial, with $\sigma_{\rm N_2D^+}/\sigma_{\rm c,vir} \sim 0.8$ (based on the mm continuum estimate of core mass, which is expected to already include subtraction of the clump mass surface density via interferometric spatial filtering and thus be consistent with using $M_{c,\rm min}$). However, for the case of the massive core C1-S, T13 found $\sigma_{\rm N_2D^+}/\sigma_{\rm c,vir} \simeq 0.45$ and argued this may imply the presence of strong ($\sim$ 1 mG), large-scale magnetic fields. Here, we observe that after the initial turbulent energy injection, the fiducial core (run S3M2) appears moderately sub-virial but later becomes super-virial as the core collapses. The simulation with a stronger magnetic field (run S3M1), which is discussed in more detail in Section 5.3.6, shows an even more sub-virial velocity dispersion when viewed in the x and y directions, consistent with the T13 estimate for C1-S.

The evolution of the fiducial run is further quantified in Figure 5.8, which shows the evolution of both the mean and maximum values of the mass surface density, chemical abundances, and $D_{\rm frac}^{\rm N_2H^+}$ in the core. Here we define the core using the effective number density threshold $n_{\rm eff}$; as this selects a unique volume, the mean column density is independent of viewing angle. Maximum values are computed from the x-axis projections. The mean mass surface density of the core decreases initially due to the initial turbulence and then increases slowly with time, from $\Sigma \approx 0.4$ g cm^{-2} up to 0.8 g cm^{-2}. The maximum value increases nearly two orders of magnitude between 0.5 and 0.7 $t_{\rm ff}$, as the central overdensity contracts rapidly. The chemical evolution is discussed in Section 5.3.2.

The same density threshold is applied to the column density probability distribution functions (PDFs) presented in Figure 5.9. As the core collapses, the initially (roughly) lognormal mass surface density distribution develops a high-density power-law tail, indicative of collapse. At simulation termination, roughly 10% of the core mass is at $\Sigma \geq 1.0$ g cm^{-2}.

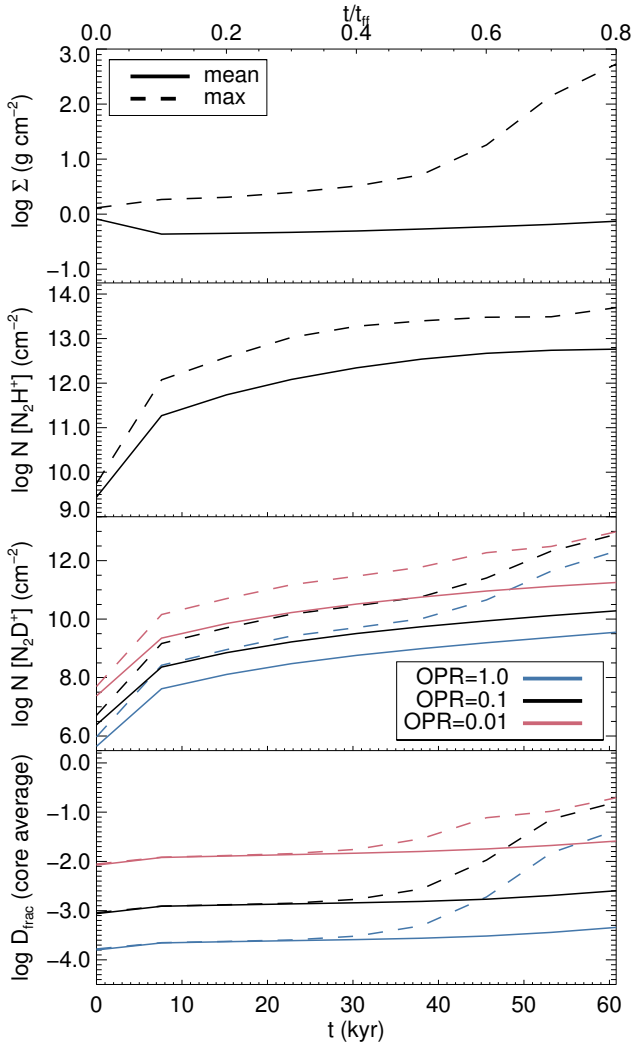

Figure 5.8: Time evolution of the mean (solid lines) and maximum (dashed lines) values of mass surface density Σ, N_2H^+ column density, N_2D^+ column density, and deuterium fraction $D_{\rm frac}^{\rm N_2H^+}$ in the fiducial core (run S3M2). For N_2D^+ and $D_{\rm frac}^{\rm N_2H^+}$, results are presented for different initial ortho-to-para ratio of H_2 (blue: $\mathrm{OPR}_0^{\rm H_2} = 1.0$; black: $\mathrm{OPR}_0^{\rm H_2} = 0.1$; red: $\mathrm{OPR}_0^{\rm H_2} = 0.01$). Time is given in units of the initial core averaged free-fall time $t_{\rm ff}$ (top x-axis) as well in absolute time (bottom x-axis). The lower the initial $\mathrm{OPR}^{\rm H_2}$, the faster the deuteration proceeds. By the end of the simulation, the only estimate for mean $D_{\rm frac}^{\rm N_2H^+}$ that is similar to observations ($\gtrsim 0.1$) is for $\mathrm{OPR}_0^{\rm H_2} = 0.01$.

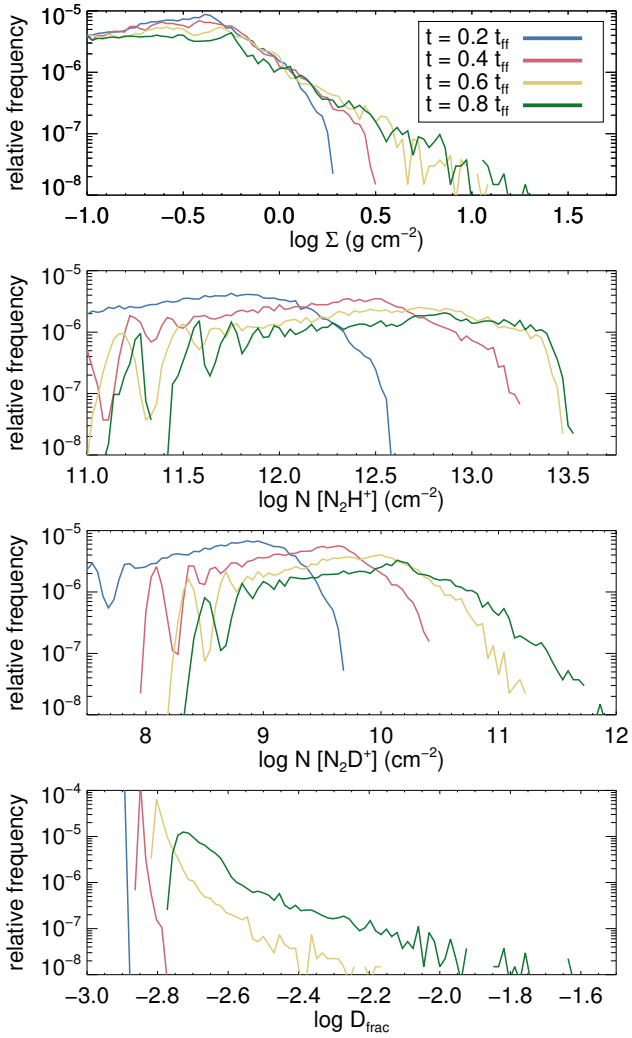

Figure 5.9: Probability distribution functions in our fiducial simulation (run S3M2) at multiple times. From top to bottom, the panels show the mass surface density Σ, the N_2H^+ column density, the N_2D^+ column density, and the deuterium fraction $D_{\rm frac}^{\rm N_2H^+}$. Simulation times are indicated by color (blue: t =0.2 $t_{\rm ff}$; red: 0.4 $t_{\rm ff}$; yellow: 0.6 $t_{\rm ff}$; green: 0.8 $t_{\rm ff}$). Projections are taken along the x-axis for $t_{\rm chem} = 0$ and $\rm OPR_0^{H_2} = 0.1$.

5.3.2 Chemical Evolution

As the density increases due to gravitational collapse, the growth rates of the chemical species also increase. We observe in Figures 5.4 and 5.5 that N_2H^+ reaches equilibrium before N_2D^+ and is more widespread. This agrees well with observations of pre-stellar core regions; K16 find an extended envelope of N_2H^+ emission around cores in IRDC G028.37+00.07, while N_2D^+ is more concentrated. The asymmetry introduced by the magnetic field also affects the chemical morphology; when viewing perpendicular to the field, the chemical tracers are more centrally-concentrated. The chemical evolution is also quantified in Figure 5.8. The mean N_2H^+ column density increases rapidly and then flattens over time as equilibrium is reached; in contrast, the mean N_2D^+ column density grows steadily throughout the simulation without reaching equilibrium, and $D_{\rm frac}^{\rm N_2H^+}$ increases only modestly until late times (after N_2H^+ has reached equilibrium). The maximum values of N_2D^+ and $D_{\rm frac}^{\rm N_2H^+}$ do reach equilibrium values, but this is limited to only the densest regions of the core. This is confirmed in Figure 5.9, which shows only a small fraction of cells in the core are able to reach $D_{\rm frac}^{\rm N_2H^+} \geq 0.1$ by the end of the simulation. As K16 detected widespread deuteration in pre-stellar cores (see also the study of Barnes et al. (2016) for evidence of widespread deuteration on parsec-sized, lower-density scales in an IRDC), this suggests more time is needed for the outer regions of the core to reach observed values.

Figure 5.10 presents radial averages of $D_{\rm frac}^{\rm N_2H^+}$ within the core at different times and projection directions. $D_{\rm frac}^{\rm N_2H^+}$ grows rapidly in the center of the core, where the density is highest, while in the outer regions, $D_{\rm frac}^{\rm N_2H^+}$remains relatively unchanged for the duration of the simulation. The direction of projection does not significantly affect the radial profile, which suggests observed radial profiles could be a useful (viewing-angle-independent) means to constrain the age of the core. Radial mapping of $D_{\rm frac}^{\rm N_2H^+}$ within observed cores is now technically feasible with ALMA.

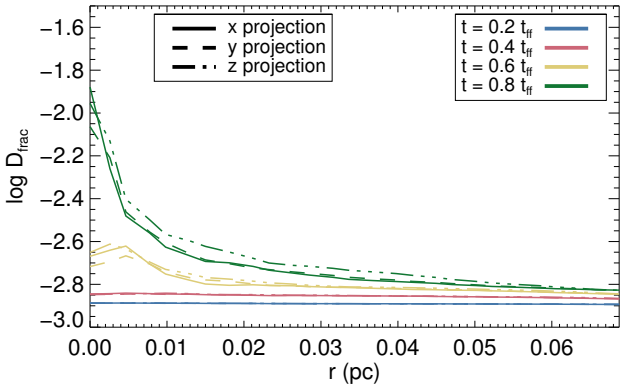

Figure 5.10: Radial averages of $D_{\rm frac}^{\rm N_2H^+}$ in our fiducial simulation (run S3M2) for $t_{\rm chem} = 0$ and $\rm OPR_0^{H_2} = 0.1$. Results are shown for different times (blue: 0.2 $t_{\rm ff}$; red: 0.4 $t_{\rm ff}$; yellow: 0.6 $t_{\rm ff}$; green: 0.8 $t_{\rm ff}$) and projection directions (solid: x-axis; dashed: y-axis; dash-dotted: z-axis).

5.3.3 Effect of Initial $\rm OPR^{H_2}$

Pagani et al. (2013) and K15 found that the initial ortho-to-para ratio of H_2 ($\rm OPR_0^{H_2}$) strongly affected the chemical evolution of N_2D^+ and $D_{\rm frac}^{\rm N_2H^+}$. Our fiducial simulation has $\rm OPR_0^{H_2} = 0.1$. As the hydrodynamics is unaffected by the chemistry, we simultaneously evolve the molecular species using $\rm OPR_0^{H_2} = 0.01$ and $\rm OPR_0^{H_2} = 1.0$. The evolution of the mean values of N_2D^+ and $D_{\rm frac}^{\rm N_2H^+}$ at different $\rm OPR_0^{H_2}$ is shown in Figure 5.8. As noted by K15, a lower $\rm OPR_0^{H_2}$ leads to faster growth of N_2D^+, as well as a larger equilibrium value of $[N_2D^+]$. Since N_2H^+ is unchanged by $\rm OPR_0^{H_2}$, $D_{\rm frac}^{\rm N_2H^+}$ also grows faster and reaches a higher value. The mean value of $D_{\rm frac}^{\rm N_2H^+}$ remains below the observed values ($\gtrsim 0.1$) even at the lowest $\rm OPR_0^{H_2}$ (=0.01), indicating a longer core lifetime and/or earlier deuteration (see Section 5.3.4) is necessary. The effect of varying $\rm OPR_0^{H_2}$ is also presented in Figure 5.11, which shows the ratio of chemical column densities (i.e., $D_{\rm frac}^{\rm N_2H^+}$) at the end of the fiducial simulation for varying $\rm OPR_0^{H_2}$. From the top row moving down, $\rm OPR_0^{H_2}$ decreases for a given chemical age, with a corresponding increase in the mean deuterium fraction in the core.

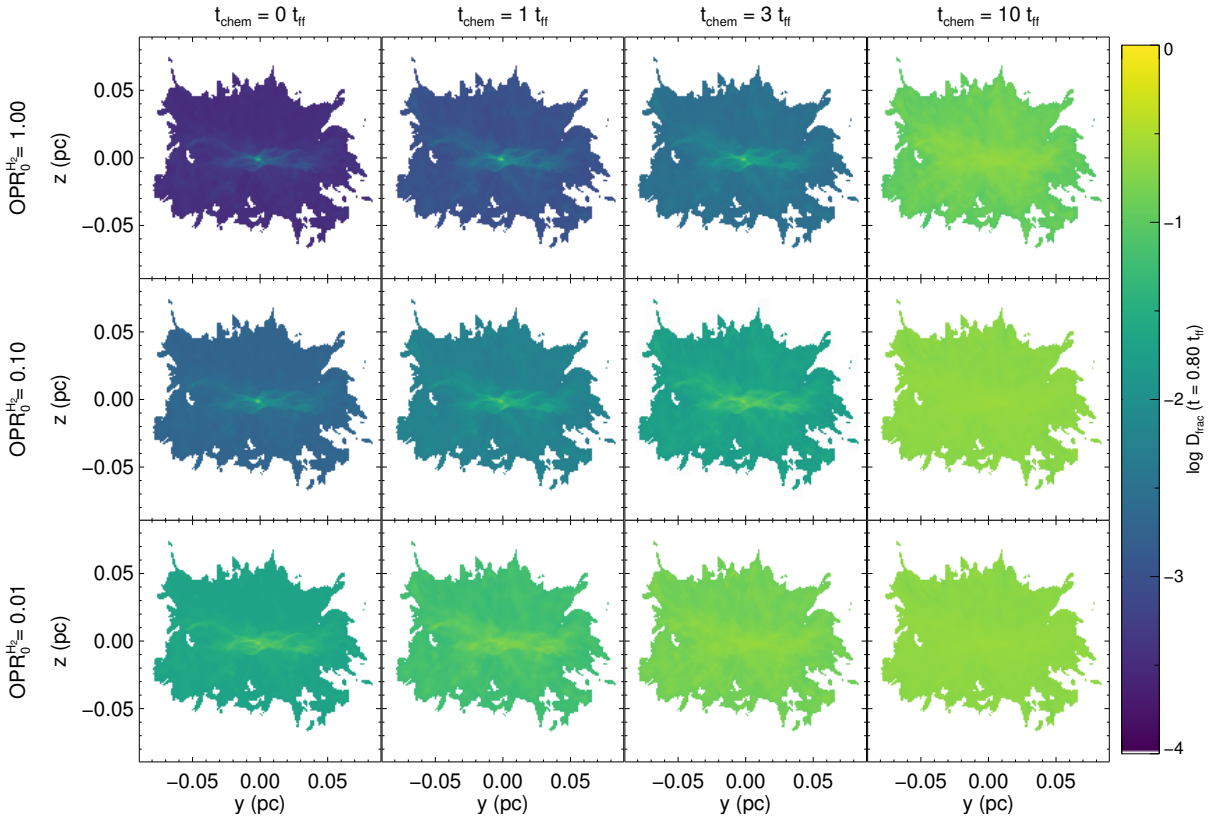

Figure 5.11: Ratio of chemical column densities ($D_{\rm frac}^{\rm N_2H^+}$) at simulation termination ($t = 0.8t_{\rm ff}$) from our fiducial model (run S3M2) for different initial chemical ages and ortho-to-para ratios of H_2. From left to right, the columns are at $t_{\rm chem}$ = 0, 1, 3, and 10 $t_{\rm ff}$; from top to bottom, the rows are $\rm OPR_0^{H_2}$ = 1.00, 0.10, and 0.01. As either $t_{\rm chem}$ or $\rm OPR_0^{H_2}$ are increased, the resulting mean deuterium fraction in the core increases.

5.3.4 Effect of Initial Chemical Age

We have thus far assumed in our calculations that the gas begins in an initially pristine condition, with $t_{\rm chem} = 0$, i.e., $[N_2H^+]$=$[N_2D^+]$=0.0 at $t = 0$. However, this may not be the case, especially given our initial condition; we initialize the core after it has already formed a centrally-concentrated structure. Deuteration begins once CO begins to freeze-out, which occurred at some unknown time prior to the current state. We therefore explore different "chemical ages" for the core: $t_{\rm chem} = 0$, 1, 3, and 10 $t_{\rm ff}$. To set the initial condition for the chemical abundances, we reference the constant density results of K15 at an absolute time, as described in Section 5.2.2. The core then begins from an advanced state of deuteration, assuming the core has been in its current density configuration for $t_{\rm chem}$. While the dynamical collapse is unchanged, the core is able to reach higher deuterium fractions. As is evident in Figure 5.11, the deuterium fraction increases for increasing chemical age, with nearly the entire core achieving the equilibrium value of $D_{\rm frac}^{\rm N_2H^+}$ for $t_{\rm chem} = 10 t_{\rm ff}$. While this may seem to agree with the estimates of K15, which indicated up to 10 free-fall times may be necessary to reach observed values of $D_{\rm frac}^{\rm N_2H^+}$, the simulations are not directly comparable. In K15, the density continually increases, with a corresponding decrease in $t_{\rm ff}$; here, we assume a constant density (hence a constant $t_{\rm ff}$) prior to initialization. Regardless, in both cases the conclusion remains that deuteration must proceed for longer than the average free-fall time, either by earlier deuteration or slower collapse.

5.3.5 Effect of Initial Mass Surface Density

We also examine the effect of varying the initial clump mass surface density $\Sigma_{\rm cl}$. Our fiducial simulation uses $\Sigma_{\rm cl} = 0.3$ g cm^{-2}; however, this is the current observed state of the cores in the T13 sample. As the cores currently show significant deuteration, we investigate an earlier phase of the core lifetime by decreasing the initial clump mass surface density to $\Sigma_{\rm cl} = 0.1$ g cm^{-2} (run S1M2). We keep the core mass fixed at 60 M$_\odot$ and use the prescription of MT03 to adjust the core radius (increase $R_{\rm c} \rightarrow 0.18$ pc) and surface number

density (decrease $n_{\mathrm{H},s} \rightarrow 8.2 \times 10^4$ cm^{-3}). The average core free-fall time then increases to $t_{\mathrm{ff}} \rightarrow 173$ kyr. We maintain the core temperature at $T_{\mathrm{c}} = 15$ K and the initial virial parameter $\alpha = 2$; the initial velocity dispersion then decreases to $\sigma \rightarrow 0.76$ km s^{-1}. We also maintain the same mass-to-flux ratio $\mu_{\Phi} = 2$; the central field strength is then reduced to $B_{\mathrm{c}} \rightarrow 0.27$ mG.

Figures 5.12 and 5.13 show the evolution of run S1M2 for projections along the x- and z-axes, respectively. Based on the results of K15 presented in Figure 5.1, we expect the lower densities in the core to lead to slower chemical growth and lower equilibrium values of $D_{\mathrm{frac}}^{\mathrm{N_2H^+}}$. The core collapses more slowly on an absolute timescale, but the simulation terminates at the same relative time, $t = 0.8\ t_{\mathrm{ff}}$. Comparing on a relative timescale, there are only modest differences in morphology and chemistry between the two cases. At termination, run S1M2 appears more filamentary and less centrally concentrated than run S3M2. Although the absolute column density values are lower, the mean $D_{\mathrm{frac}}^{\mathrm{N_2H^+}}$ is actually higher. This is displayed in Figure 5.14, which shows the final mean chemical column densities and corresponding $D_{\mathrm{frac}}^{\mathrm{N_2H^+}}$ for all simulations performed. Depending on the value of t_{chem} and $\mathrm{OPR}_0^{\mathrm{H_2}}$, $D_{\mathrm{frac}}^{\mathrm{N_2H^+}}$ is higher in run S1M2 by a factor of 1-5 over run S3M2. We therefore conclude that the initial mass surface density does not strongly affect the chemical evolution.

5.3.6 Effect of Magnetic Field Strength

We also test the effect of increasing the magnetic field strength. We perform simulations with a critical field strength ($\mu_{\Phi} = 1.0$) for both the fiducial mass surface density ($\Sigma_{\mathrm{cl}} = 0.3$ g cm^{-2}; run S3M1) and the decreased value ($\Sigma_{\mathrm{cl}} = 0.1$ g cm^{-2}; run S1M1). Projections are shown for run S3M1 in Figures 5.15 and 5.16, and for run S1M1 in Figures 5.17 and 5.18. In both instances, the stronger magnetic field leads to an initial expansion of the core before it coalesces again and collapses. The critical field does slow the contraction – both simulations run $0.2t_{\mathrm{ff}}$ past the corresponding $\mu_{\Phi} = 2.0$ simulations – but ultimately does not prevent collapse. The slower collapse leads to a larger, more diffuse core compared to

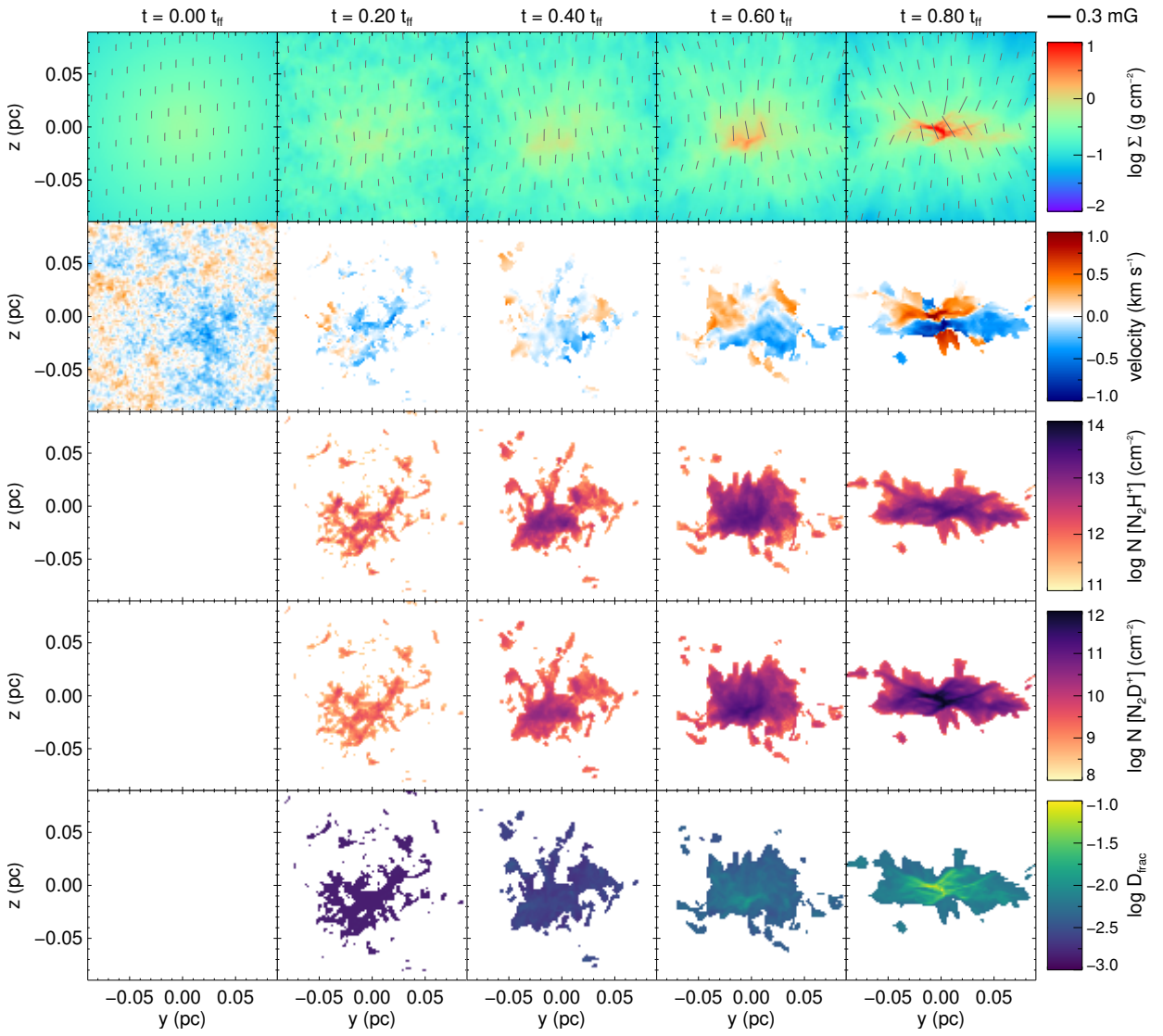

Figure 5.12: Similar to Figure 5.4 but for a core with lower initial mass surface density ($\Sigma_{\rm cl}$ = 0.1 g cm^{-2}; run S1M2). Projections are taken along the x-axis (perpendicular to initial magnetic field direction). The simulation runs to the same relative time (0.8 $t_{\rm ff}$), which corresponds to a longer absolute time (139 kyr).

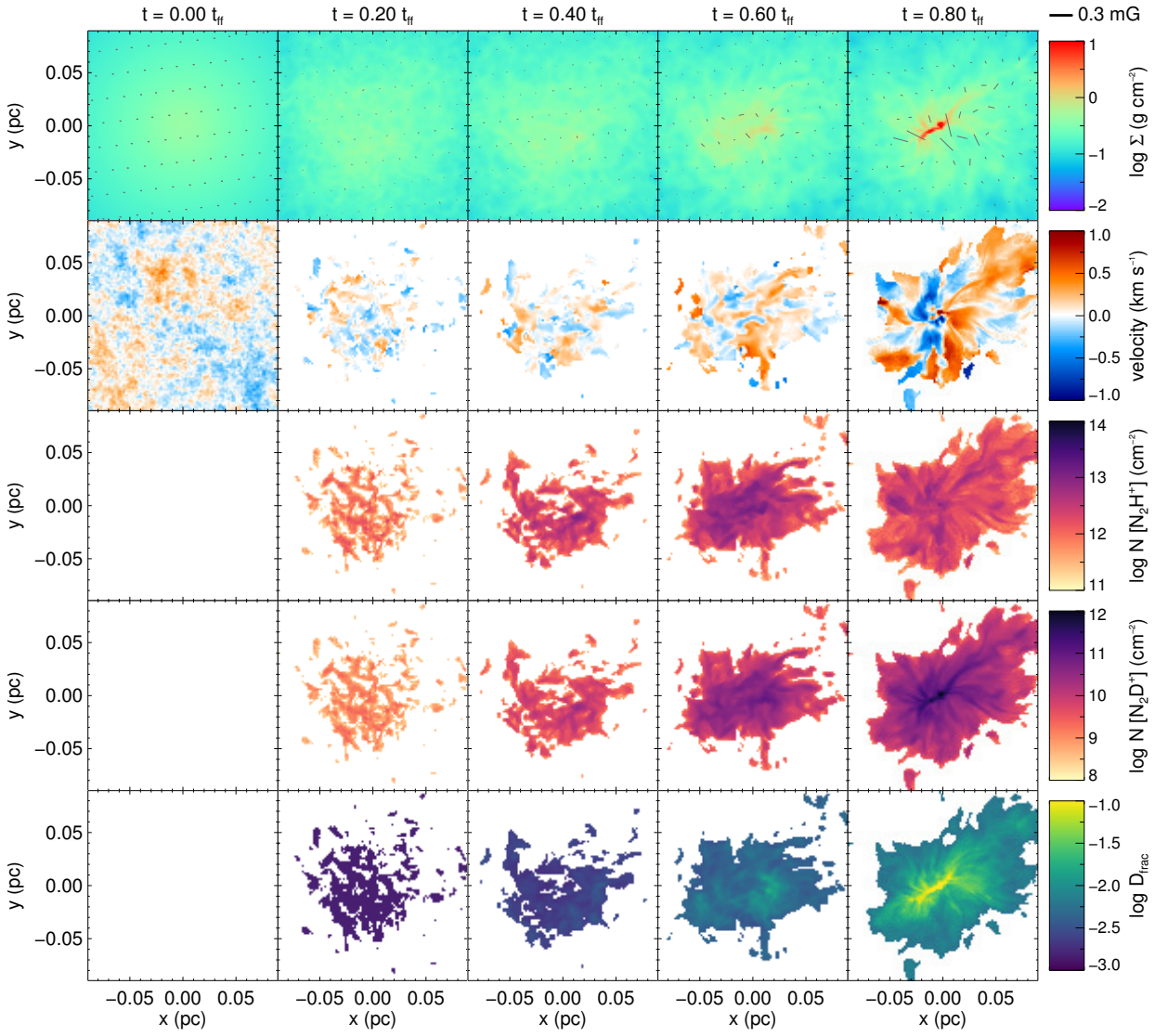

Figure 5.13: Same simulation as in Figure 5.12 (run S1M2) but now the projections are taken along the z-axis, parallel to the initial magnetic field direction.

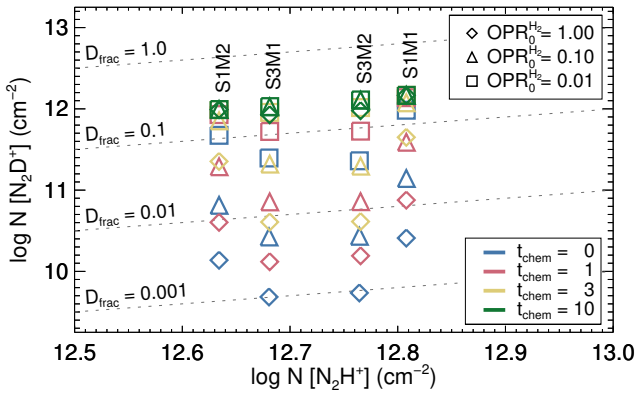

Figure 5.14: Summary of mean chemical column densities in the core for all runs at simulation termination, for varying initial chemical age (indicated by color) and ortho-to-para ratio of H_2 (indicated by symbol). Reference lines for $D_{\rm frac}^{\rm N_2H^+}$ are indicated with dashed lines. The N_2H^+ column density is largely constant across the parameter space of each run because 1) N_2H^+ is largely unaffected by changes in $\rm OPR^{H_2}$; and 2) equilibrium is reached for all values of $t_{\rm chem}$. Values of $D_{\rm frac}^{\rm N_2H^+} \geq 0.1$ are only reached for low values of $\rm OPR_0^{H_2}$ or large chemical age.

the fiducial run at a given time. The stronger field also inhibits motions perpendicular to the field, as illustrated in Figure 5.7. The velocity dispersions in the x and y directions are lower in run S3M1 compared to run S3M2, while the z direction is largely unaffected. The filamentary structure observed perpendicular to the field is also narrower, which reduces estimates of the mass.

Figure 5.14 reveals that the longer timescale at $\mu_\Phi = 1.0$ does result in a higher mean value of $D_{\rm frac}^{\rm N_2H^+}$ in both cases, but only by a factor of 1-2 over runs with $\mu_\Phi = 2.0$. As with the mass surface density, we conclude that the magnetic field strength does not strongly affect the resulting deuterium fraction. However, we caution that this result may be influenced by the initial field geometry (see Section 5.4), and further investigation is warranted.

5.4 Discussion

Figure 5.14 summarizes the final mean chemical column densities (and $D_{\rm frac}^{\rm N_2H^+}$) for all simulations performed and across the entire parameter space. In agreement with the one-zone models of K15, we find that deuteration proceeds slowly during collapse and only reaches

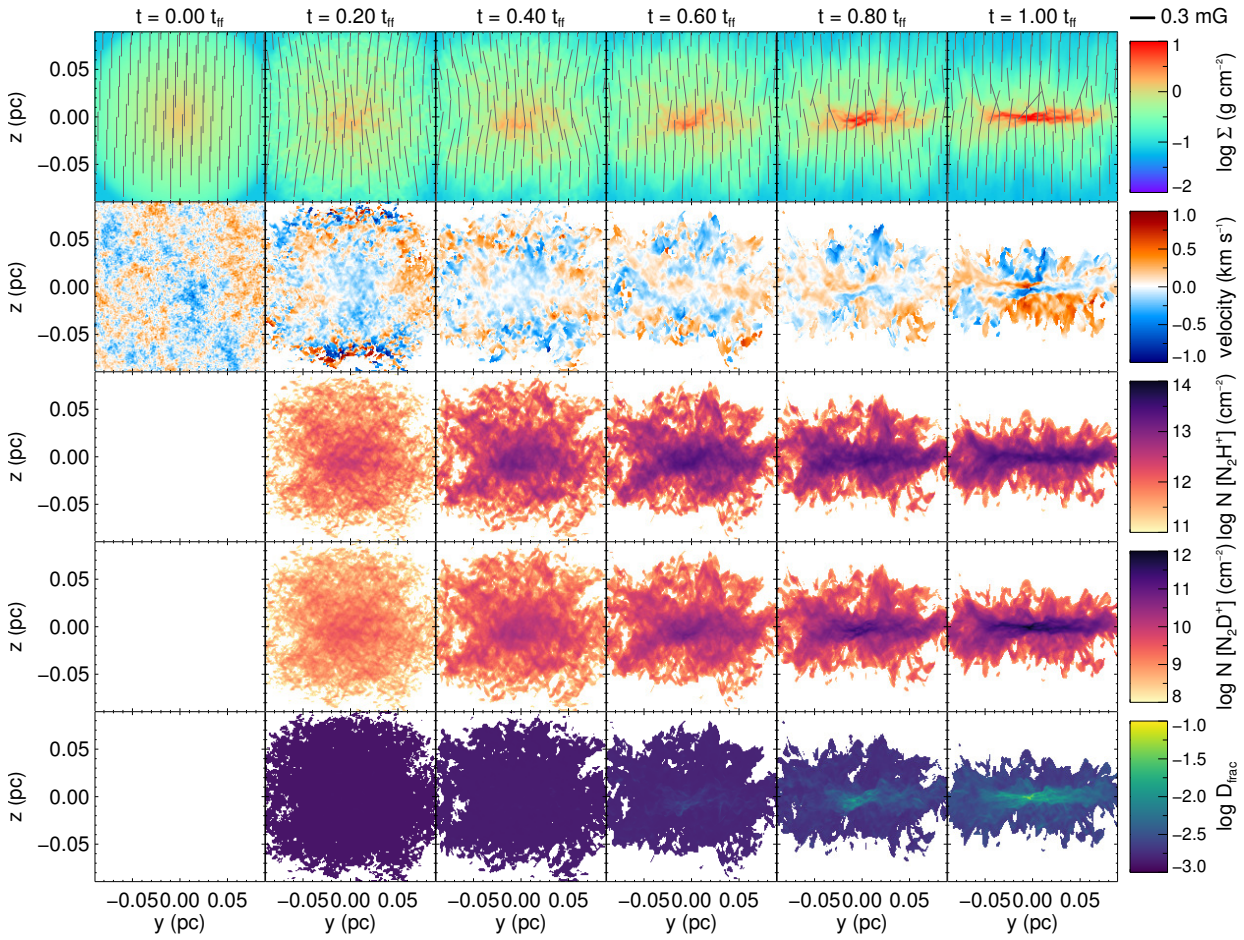

Figure 5.15: Similar to Figure 5.4 but for a core with a stronger magnetic field ($\mu_\Phi = 1$; run S3M1). Projections are taken along the x-axis, perpendicular to initial magnetic field direction. The critical magnetic field inhibits the collapse, allowing the simulation to proceed another 0.2 $t_{\rm ff}$. Due to flux-freezing, material collapses most freely parallel to the magnetic field; hence the core becomes compressed in the z-direction.

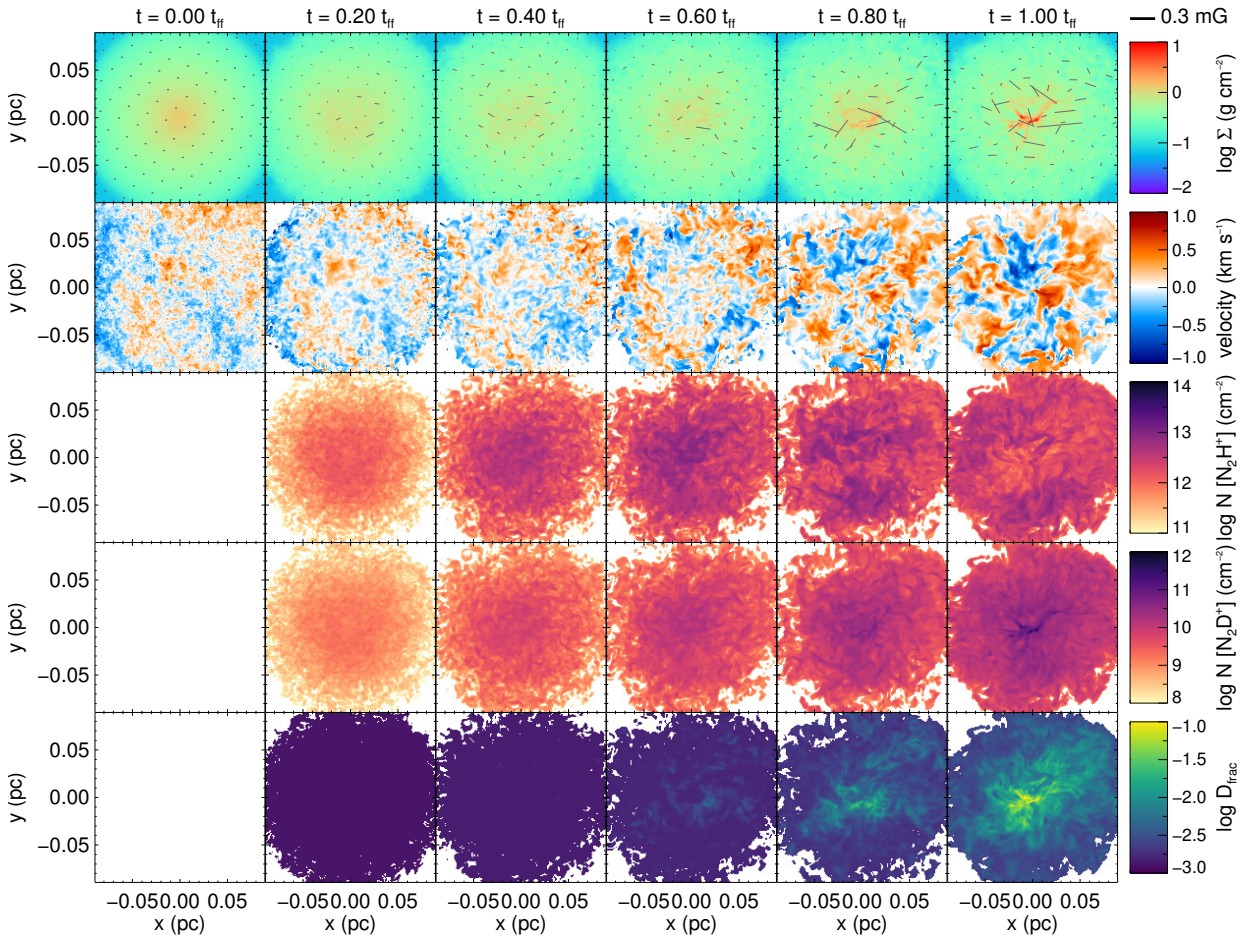

Figure 5.16: Same simulation as Figure 5.15 (run S3M1) but now the projections are taken along the z-axis, parallel to the initial magnetic field direction.

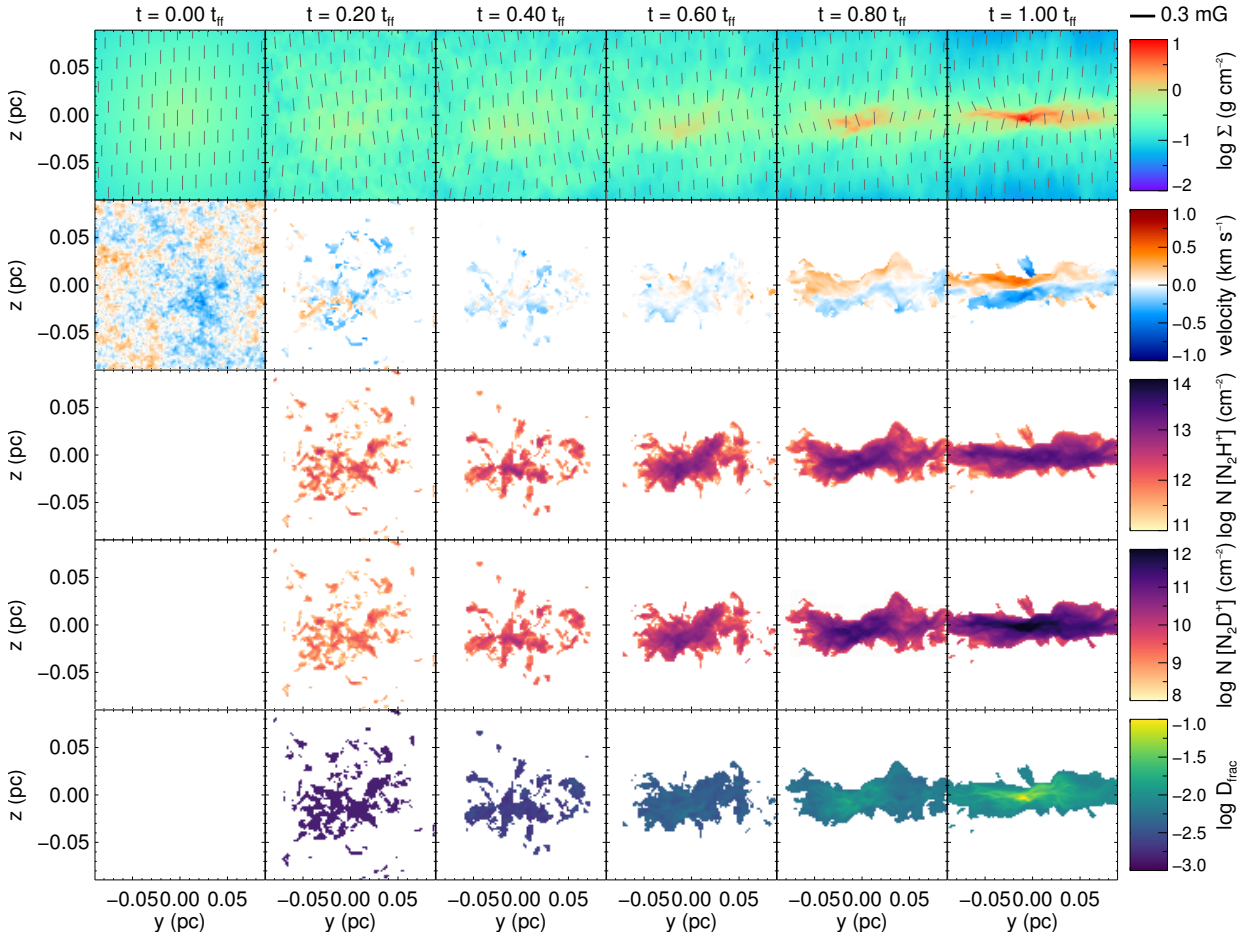

Figure 5.17: Similar to Figure 5.12 but for a core with increased magnetic field strength ($\Sigma_{\rm cl} = 0.1$, $\mu_\Phi = 1$; run S1M1). Projections are taken along the x-axis (perpendicular to initial magnetic field direction). As in Figure 5.15, the stronger field again slows the collapse and leads to an elongated core.

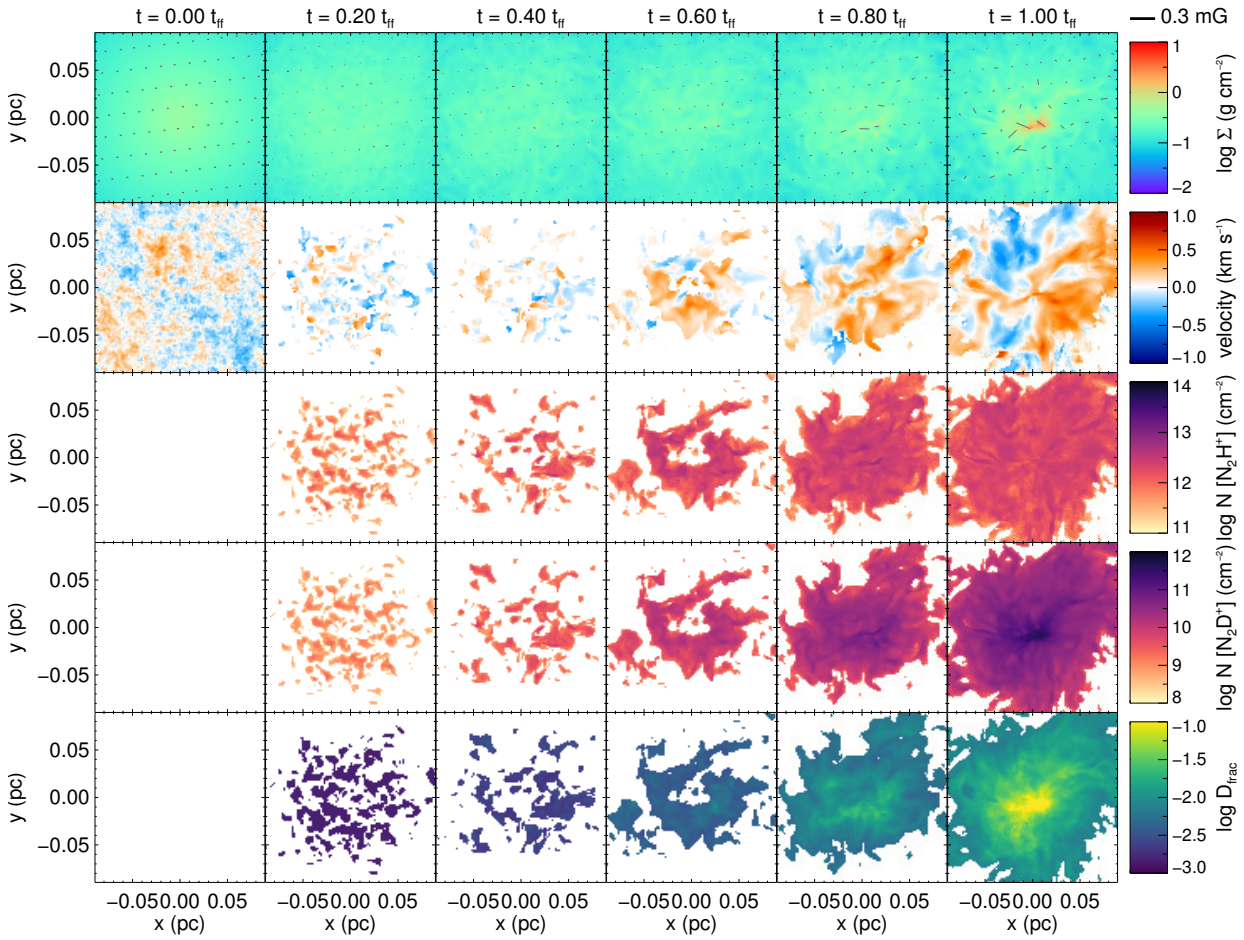

Figure 5.18: Same simulation as Figure 5.17 (run S1M1) but for projections taken along the z-axis, parallel to the initial magnetic field direction.

observed values under certain conditions, namely low $\mathrm{OPR}_0^{\mathrm{H_2}}$ ($\lesssim 0.01$) or advanced chemical evolution ($t_{\mathrm{chem}} \gtrsim 3t_{\mathrm{ff}}$). The initial mass surface density and magnetic field strength do not largely alter this conclusion.

Our approximate chemistry model for N_2H^+ deuteration is constructed from the results of K15. The K15 chemical network calculations were performed with the same physical conditions (e.g., temperature, ionization rate, dust-to-gas ratio) except for the density and $\mathrm{OPR}_0^{\mathrm{H_2}}$. As noted in Section 5.2.2, these two quantities play a large role in determining the deuteration and are therefore parameters of our model. However, varying any of the other K15 model parameters could shift the equilibrium value of $D_{\mathrm{frac}}^{\mathrm{N_2H^+}}$ by an order of magnitude, as is evident in fig. 5 of K15. In particular, increasing the initial heavy-element depletion factor f_{D} decreases the timescale for deuteration. This may explain the discrepancy between our work and the results of Pagani et al. (2013); we set $f_{\mathrm{D}} = 10$ and obtain results consistent with slow collapse, whereas Pagani et al. (2013) chose $f_{\mathrm{D}} \gtrsim 300$ and determined a fast collapse best matched $D_{\mathrm{frac}}^{\mathrm{N_2H^+}}$observations. While there is evidence for some CO depletion ($f_{\mathrm{D}} \lesssim 5$) in IRDCs (Hernandez et al., 2011, 2012), further observations are necessary to better constrain this parameter. Fig. 5 of K15 also demonstrates the effect of changing the cosmic ray ionization rate ζ; increasing ζ will both decrease the equilibrium value of $D_{\mathrm{frac}}^{\mathrm{N_2H^+}}$and increase the growth rate of $D_{\mathrm{frac}}^{\mathrm{N_2H^+}}$. We also note that the K15 fiducial parameter values may not be applicable across the full range of densities ($10^3 \leq n_{\mathrm{H}} \leq 10^9 \mathrm{cm}^{-3}$). Short of implementing the full network in 3D MHD simulations, future work could introduce density-dependent parameters to better span the K15 parameter space. Finally, our parameterization introduces a systematic overestimate of N_2H^+ and underestimate of $D_{\mathrm{frac}}^{\mathrm{N_2H^+}}$, by up to 30% relative error. While the approximation is expedient for simulations, a time-dependent chemical network will be required to obtain more accurate species evolution as the density evolves.

The cores begin with a smooth density profile, and we rely on the initial super-virial turbulent velocity field to create density fluctuations. The turbulence is thus not fully developed at initialization, and the energy decays rapidly as seen in Figure 5.7. Ideally,

the density and velocity structure would be generated in a self-consistent manner, possibly through driven turbulence with subsequent application of gravity (e.g., Heitsch et al., 2001; Myers et al., 2014).

We consider magnetic fields but neglect non-ideal MHD effects, such as ambipolar diffusion (AD). The AD timescale is estimated in figure 6 of K15 to be roughly an order of magnitude longer than the free-fall timescale for all relevant densities (see also Heitsch & Hartmann, 2014). As all our simulations terminate prior to $t = 2\ t_{\rm ff}$, we do not expect AD to significantly affect the dynamics. However, the field geometry may affect the results. We begin with a smooth, cylindrically-symmetric field in the z-direction. As with the density field, the magnetic field is tangled by turbulent motions, but only after initialization. Material freely collapses along the field lines even when the field is of critical strength. Future studies should begin either with a tangled component in addition to an ordered component, or should generate a tangled field through turbulent driving (Myers et al., 2014).

We are limited in the range of spatial scales we can probe due to the lack of mesh refinement. Our fiducial simulation is performed using a fixed grid of 512^3 grid cells, for a minimum resolution of $\delta \approx 360$ AU. Following the collapse and chemical evolution further will require additional resolution, possibly through the use of mesh refinement.

We also halt our calculations when the collapsing core is no longer adequately resolved, i.e., at protostar formation. We do not include sink particles, as we are only interested in pre-stellar conditions. For similar reasons, we also neglect radiative feedback. As demonstrated by Commerçon et al. (2011) and Myers et al. (2013), including radiation feedback from protostars slows the collapse and inhibits fragmentation. It is unclear how the protostellar radiation field will affect the deuteration process; however, there is recent evidence that protostars can exist within highly-deuterated regions (Tan et al., 2016). Radiation effects could increase the core lifetime and hence the deuterium fraction, and future studies following the chemistry for longer periods should include these effects using sink particles and radiation-magnetohydrodynamics.

5.5 Conclusions

We have constructed an approximate chemical model for the deuteration of N_2H^+ in cold, dense pre-stellar gas. Our model is based on the results of the astrochemical network presented in K15. The full network is prohibitively expensive in multi-dimensional hydrodynamics simulations. Rather than reducing the number of reactions, we parameterize the results across a range of densities into look-up tables. This approximate formulation is demonstrated to perform reasonably well in comparison to full network calculations with both constant and evolving density.

We implement our approximate chemical model in the Athena MHD code. In 3D simulations, we follow deuteration during the collapse of a turbulent, magnetized pre-stellar core. The core is initialized in accordance with the Turbulent Core Accretion model of MT03. For our adopted initial conditions, the core collapses to the point of forming a protostar within roughly one free-fall time, regardless of the initial mass surface density or magnetic field strength. During most of this collapse phase the velocity dispersion of the core as traced by $N_2D^+(3–2)$ appears moderately sub-virial compared to predictions of the MT03 Turbulent Core Model, consistent with observations of T13 and Kong et al. (2017). Only near the end, just before protostar formation, does the velocity dispersion rise to appear super-virial.

As the core collapses, the increase in density accelerates the deuteration of N_2H^+. However, we find that $D_{\rm frac}^{\rm N_2H^+}$ does not reach observed values ($\gtrsim 0.1$) in $\sim 1\ t_{\rm ff}$, unless the initial ortho-to-para ratio of H_2 ($\rm OPR_0^{H_2}$) is $\lesssim 0.01$ or the core begins from an advanced chemical state ($t_{\rm chem} \gtrsim 3\ t_{\rm ff}$). This is in agreement with K15 and suggests that the collapse rate in highly-deuterated cores may be significantly slower than the free-fall time, or the deuteration process begins earlier than assumed.

CHAPTER 6: CONCLUSION

6.1 Conclusions and future work

A nearby Type II supernova (SN) remains the most likely candidate as the source of short-lived radioisotopes (SLRs) in the early solar system (ESS). However, hydrodynamical simulations of enrichment by SNe have repeatedly shown that the injection of SLRs is several orders of magnitude less than required to match ESS abundances.

It may be that mixing is suppressed by insufficient numerical resolution. I have therefore investigated the role of hydrodynamical turbulent mixing in SLR enrichment. I have implemented six two-equation Reynolds-averaged Navier-Stokes (RANS) turbulence models in the Athena hydrodynamics code. After verifying the models with standard mixing layer tests, I apply the models to the astrophysical shock-cloud interaction. To better understand SLR enrichment of the ESS, I focus on the role of turbulent mixing and injection. I find that, in contrast to previous predictions, estimates of the mixing actually increase with increasing resolution, but only once sufficient resolution is attained to resolve the turbulent cascade. This required the highest resolution fixed-grid simulations of the shock-cloud interaction to date, with over half a million CPU hours used for a single simulation. Furthermore, this finding agrees with the elevated mixing predictions of the turbulence models, but it remains unclear whether this result holds in other applications.

Even if the hydrodynamical mixing is underestimated at typical resolutions, the gas-phase injection may still be insufficent to explain ESS abundances. I have therefore explored an alternate injection mechanism, namely dust grains formed from the SN ejecta and carrying SLRs. Using hydrodynamical simulations, I model the interaction of a SNR carrying dust grains with the pre-solar cloud. I find that sufficiently large dust grains ($a \geq 1$ μm) formed

in the SN ejecta can survive entry into the cloud, where they are either stopped or destroyed. This rapidly enrichs the dense (potentially star-forming) gas with SLRs. Smaller dust grains ($a \leq 0.1$ μm) are either stopped or sputtered before impacting the cloud, although they can still enhance the enrichment through subsequent hydrodynamical mixing. While it is still unclear what sizes and amounts of dust are common in SNR, I show that any dust grains can contribute favorably in the typical SN enrichment scenario. Finally, the spatial stratification of different sized dust grains could explain the discrepancy in ^{60}Fe/^{26}Al mass ratio between SN nucleosynthesis predictions and ESS meteoritic measurements. I conclude that dust grains are a viable mechanism for the transport of SLRs into the ESS. Future studies should examine the role of magnetic fields and grain charge in SN enrichment.

Finally, the short half-lives of the SLRs constrains the time and distance from the ESS to the massive stellar nucleosynthetic source. The odds of enrichment are therefore best if the SN progenitor formed just before the ESS in the same cluster of stars. If star formation proceeds slowly, this could reduce the likelihood of enrichment. We therefore investigate the timescale for massive star formation by comparing observations of highly-deuterated pre-stellar cores to three-dimensional magnetohydrodynamical simulations with an approximate chemical model. We parameterize the results from a full chemical network to produce a robust and efficient method for the deuteration of N_2H^+ in Athena. Despite varying the initial magnetic field and surface density of the core, all models collapse to form a protostar within roughly one free-fall time. While the deuterium fraction does increase during collapse, it does not reach observed values ($\gtrsim 0.1$) within one free-fall time, unless the initial conditions are more advanced than assumed. Further work is necessary to determine when deuteration begins in the star formation process.

BIBLIOGRAPHY

Adams, F. C. 2010, Annual Review of Astronomy and Astrophysics, 48, 47

Amelin, Y., Kaltenbach, A., Iizuka, T., et al. 2010, Earth and Planetary Science Letters, 300, 343

Amelin, Y., Krot, A. N., Hutcheon, I. D., & Ulyanov, A. A. 2002, Science, 297, 1678

Bai, X.-N., & Stone, J. M. 2010, The Astrophysical Journal Supplement Series, 190, 297

Barnes, A. T., Kong, S., Tan, J. C., et al. 2016, Monthly Notices of the Royal Astronomical Society, 458, 1990

Barone, M. F., Oberkampf, W. L., & Blottner, F. G. 2006, AIAA Journal, 44, 1488

Bertoldi, F., & McKee, C. F. 1992, The Astrophysical Journal, 395, 140

Bianchi, S., & Schneider, R. 2007, Monthly Notices of the Royal Astronomical Society, 378, 973

Birch, S. F., & Eggers, J. M. 1973, in Free Turbulent Shear Flows, Vol. 1 (Hampton, VA: NASA Langley Research Center), 11–40

Biscaro, C., & Cherchneff, I. 2014, Astronomy & Astrophysics, 564, A25

—. 2016, Astronomy & Astrophysics, 589, A132

Blondin, J. M., Wright, E. B., Borkowski, K. J., & Reynolds, S. P. 1998, The Astrophysical Journal, 500, 342

Bocchio, M., Jones, A. P., & Slavin, J. D. 2014, Astronomy & Astrophysics, 570, A32

Bocchio, M., Marassi, S., Schneider, R., et al. 2016, Astronomy & Astrophysics, 587, A157

Boggs, S. E., Harrison, F. A., Miyasaka, H., et al. 2015, Science, 348, 670

Bonnell, I. A., Bate, M. R., Clarke, C. J., & Pringle, J. E. 2001, Monthly Notices of the Royal Astronomical Society, 323, 785

Boss, A. P., Ipatov, S. I., Keiser, S. A., Myhill, E. A., & Vanhala, H. A. T. 2008, The Astrophysical Journal, 686, 12

Boss, A. P., & Keiser, S. A. 2010, The Astrophysical Journal, 717, L1

—. 2012, The Astrophysical Journal, 756, L9

—. 2013, The Astrophysical Journal, 770, 51

—. 2014, The Astrophysical Journal, 788, 20

—. 2015, The Astrophysical Journal, 809, 103

Boss, A. P., Keiser, S. A., Ipatov, S. I., Myhill, E. A., & Vanhala, H. A. T. 2010, The Astrophysical Journal, 708, 1268

Brown, G. L., & Roshko, A. 1974, Journal of Fluid Mechanics, 64, 775

Bryan, G. L., Norman, M. L., O'Shea, B. W., et al. 2014, The Astrophysical Journal Supplement Series, 211, 19

Burkhardt, C., Kleine, T., Bourdon, B., et al. 2008, Geochimica et Cosmochimica Acta, 72, 6177

Butler, M. J., & Tan, J. C. 2012, The Astrophysical Journal, 754, 5

Cameron, A. G. W., & Truran, J. W. 1977, Icarus, 30, 447

Caselli, P., Walmsley, C. M., Zucconi, A., et al. 2001, The Astrophysical Journal, 565, 344

Ceccarelli, C., Caselli, P., Bockel, D., et al. 2014, in Protostars and Planets VI, ed. H. Beuther, R. S. Klessen, C. P. Dullemond, & T. Henning (University of Arizona Press), 859–882

Chandrasekhar, S. 1961, Hydrodynamic and Hydromagnetic Stability (Oxford: International Series of Monographs on Physics)

Chen, J. H., & Wasserburg, G. J. 1996, in Earth Processes: Reading the Isotopic Code, ed. A. Basu & S. Hart, Vol. 95 (Washington, DC: American Geophysical Union), 1–20

Chieffi, A., & Limongi, M. 2013, The Astrophysical Journal, 764, 21

Chiravalle, V. P. 2006, Laser and Particle Beams, 24, 381

Cho, J., & Lazarian, A. 2003, Monthly Notices of the Royal Astronomical Society, 345, 325

Cioffi, D. F., McKee, C. F., & Bertschinger, E. 1988, The Astrophysical Journal, 334, 252

Clayton, D. D. 1975, The Astrophysical Journal, 199, 765

—. 1979, Astrophysics and Space Science, 65, 179

Clayton, D. D., & Nittler, L. R. 2004, Annual Review of Astronomy and Astrophysics, 42, 39

Cobb, A. K., & Pudritz, R. E. 2014, The Astrophysical Journal, 783, 140

Colella, P. 1990, Journal of Computational Physics, 87, 171

Colella, P., & Woodward, P. R. 1984, Journal of Computational Physics, 54, 174

Commerçon, B., Hennebelle, P., & Henning, T. 2011, The Astrophysical Journal, 742, L9

Couch, S. M., Graziani, C., & Flocke, N. 2013, The Astrophysical Journal, 778, 181

Crutcher, R. M. 2012, Annual Review of Astronomy and Astrophysics, 50, 29

Cunningham, A. J., Klein, R. I., Krumholz, M. R., & McKee, C. F. 2011, The Astrophysical Journal, 740, 107

DeLaney, T., Rudnick, L., Stage, M. D., et al. 2010, The Astrophysical Journal, 725, 2038

Diehl, R., Halloin, H., Kretschmer, K., et al. 2006, Nature, 439, 45

Dimonte, G., & Tipton, R. 2006, Physics of Fluids, 18, 085101

Dimonte, G., Youngs, D. L., Dimits, A., et al. 2004, Physics of Fluids, 16, 1668

Dimotakis, P. E. 1991, in High Speed Flight Propulsion Systems, 137th edn., ed. S. N. B. Murthy & E. T. Curran (Pasadena, CA: AIAA Progress in Astronautics and Aeronautics), 265–340

Draine, B. T., & Salpeter, E. E. 1979, The Astrophysical Journal, 231, 77

Dunne, L., Maddox, S. J., Ivison, R. J., et al. 2009, Monthly Notices of the Royal Astronomical Society, 394, 1307

Elmegreen, B. G. 1981, The Astrophysical Journal, 251, 820

Elmegreen, B. G., & Scalo, J. 2004, Annual Review of Astronomy and Astrophysics, 42, 211

Evans, C. R., & Hawley, J. F. 1988, The Astrophysical Journal, 332, 659

Evans, N. J. 1999, Annual Review of Astronomy and Astrophysics, 37, 311

Falgout, R. D., Jones, J. E., & Yang, U. M. 2006, in Numerical Solution of Partial Differential Equations on Parallel Computers, ed. A. Bruaset & A. Tveito (Berlin, Heidelberg: Springer), 267–294

Fontani, F., Palau, A., Caselli, P., et al. 2011, Astronomy & Astrophysics, 529, L7

Foster, P. N., & Boss, A. P. 1997, The Astrophysical Journal, 489, 346

Fryxell, B., Olson, K., Ricker, P., et al. 2000, The Astrophysical Journal Supplement Series, 131, 273

Gaidos, E., Krot, A. N., Williams, J. P., & Raymond, S. N. 2009, The Astrophysical Journal, 696, 1854

Garnier, E., Adams, N., & Sagaut, P. 2009, Large Eddy Simulation for Compressible Flows, Scientific Computation (Dordrecht: Springer), 276, doi:10.1007/978-90-481-2819-8

Gatski, T., & Jongen, T. 2000, Progress in Aerospace Sciences, 36, 655

Girichidis, P., Federrath, C., Banerjee, R., & Klessen, R. S. 2011, Monthly Notices of the Royal Astronomical Society, 413, 2741

Goldreich, P., & Sridhar, S. 1995, The Astrophysical Journal, 438, 763

Goodson, M. D., Heitsch, F., Eklund, K., & Williams, V. A. 2017, Monthly Notices of the Royal Astronomical Society, 468, 3184

Goodson, M. D., Kong, S., Tan, J. C., Heitsch, F., & Caselli, P. 2016a, The Astrophysical Journal, 833, 274

Goodson, M. D., Luebbers, I., Heitsch, F., & Frazer, C. C. 2016b, Monthly Notices of the Royal Astronomical Society, 462, 2777

Gounelle, M. 2015, Astronomy & Astrophysics, 582, A26

Gounelle, M., & Meibom, A. 2008, The Astrophysical Journal, 680, 781

Gounelle, M., Meibom, A., Hennebelle, P., & Inutsuka, S. I. 2009, The Astrophysical Journal Letters, 694, L1

Gounelle, M., & Meynet, G. 2012, Astronomy & Astrophysics, 545, A4

Gray, W. J., & Scannapieco, E. 2011, The Astrophysical Journal, 733, 88

Grefenstette, B. W., Harrison, F. A., Boggs, S. E., et al. 2014, Nature, 506, 339

Gritschneder, M., Lin, D. N. C., Murray, S. D., Yin, Q.-Z., & Gong, M.-N. 2012, The Astrophysical Journal, 745, 22

Groopman, E., Zinner, E., Amari, S., et al. 2015, The Astrophysical Journal, 809, 31

Harten, A., Lax, P. D., & van Leer, B. 1983, SIAM Review, 25, 35

Hartmann, L. 2003, The Astrophysical Journal, 585, 398

Hartmann, L., BallesterosParedes, J., & Bergin, E. A. 2001, The Astrophysical Journal, 562, 852

Heitsch, F., & Hartmann, L. 2014, Monthly Notices of the Royal Astronomical Society, 443, 230

Heitsch, F., Mac Low, M., & Klessen, R. S. 2001, The Astrophysical Journal, 547, 280

Heitsch, F., Zweibel, E. G., Slyz, A. D., & Devriendt, J. E. G. 2004, The Astrophysical Journal, 603, 165

Hennebelle, P., Commerçon, B., Joos, M., et al. 2011, Astronomy & Astrophysics, 528, A72

Hernandez, A. K., Tan, J. C., Caselli, P., et al. 2011, The Astrophysical Journal, 738, 11

Hernandez, A. K., Tan, J. C., Kainulainen, J., et al. 2012, The Astrophysical Journal, 756, L13

Heymann, D., & Dziczkaniec, M. 1976, Science, 191, 79

Hockney, R. W., & Eastwood, J. W. 1988, Computer Simulation using Particles (Bristol: Hilger)

Huang, P., & Coakley, T. 1992, in 30th Aerospace Sciences Meeting and Exhibit (Reston, Virigina: American Institute of Aeronautics and Astronautics)

Iapichino, L., Adamek, J., Schmidt, W., & Niemeyer, J. C. 2008, Monthly Notices of the Royal Astronomical Society, 388, 1079

Iliadis, C., Champagne, A., Chieffi, A., & Limongi, M. 2011, The Astrophysical Journal Supplement Series, 193, 16

Indebetouw, R., Matsuura, M., Dwek, E., et al. 2014, The Astrophysical Journal, 782, L2

Indriolo, N., & McCall, B. J. 2012, The Astrophysical Journal, 745, 91

Inoue, T., Shimoda, J., Ohira, Y., & Yamazaki, R. 2013, The Astrophysical Journal, 772, L20

Jacobsen, B., Matzel, J., Hutcheon, I., et al. 2009, Geochimica et Cosmochimica Acta Supplement, 73, A580

Jacobsen, B., Yin, Q.-z., Moynier, F., et al. 2008, Earth and Planetary Science Letters, 272, 353

Jiang, Y. F., Belyaev, M., Goodman, J., & Stone, J. M. 2013, New Astronomy, 19, 48

Jura, M., Xu, S., & Young, E. D. 2013, The Astrophysical Journal, 775, L41

Keto, E., & Caselli, P. 2010, Monthly Notices of the Royal Astronomical Society, 402, 1625

Kim, C.-G., & Ostriker, E. C. 2015, The Astrophysical Journal, 802, 99

Klein, R. I., McKee, C. F., & Colella, P. 1994, The Astrophysical Journal, 420, 213

Kong, S., Caselli, P., Tan, J. C., Wakelam, V., & Sipilä, O. 2015, The Astrophysical Journal, 804, 98

Kong, S., Tan, J. C., Caselli, P., et al. 2017, The Astrophysical Journal, 834, 193

—. 2016, The Astrophysical Journal, 821, 94

Koyama, H., & Inutsuka, S.-i. 2001, The Astrophysical Journal, 564, L97

Kozasa, T., Hasegawa, H., & Nomoto, K. 1989, The Astrophysical Journal, 344, 325

Kruijer, T. S., Kleine, T., Fischer-Gödde, M., Burkhardt, C., & Wieler, R. 2014, Earth and Planetary Science Letters, 403, 317

Krumholz, M. R., Cunningham, A. J., Klein, R. I., & McKee, C. F. 2010, The Astrophysical Journal, 713, 1120

Krumholz, M. R., Klein, R. I., & McKee, C. F. 2007, The Astrophysical Journal, 656, 959

Kuffmeier, M., Mogensen, T. F., Haugbølle, T., Bizzarro, M., & Nordlund, . 2016, The Astrophysical Journal, 826, 22

Lada, C. J., & Lada, E. A. 2003, Annual Review of Astronomy and Astrophysics, 41, 57

Launder, B., & Spalding, D. 1974, Computer Methods in Applied Mechanics and Engineering, 3, 269

Lee, T., Papanastassiou, D. A., & Wasserburg, G. J. 1976, Geophysical Research Letters, 3, 41

—. 1977, The Astrophysical Journal, 211, L107

Lemaster, M. N., & Stone, J. M. 2009, The Astrophysical Journal, 691, 1092

Limongi, M., & Chieffi, A. 2006, The Astrophysical Journal, 647, 483

Lin, Y., Guan, Y., Leshin, L. A., Ouyang, Z., & Wang, D. 2005, Proceedings of the National Academy of Sciences, 102, 1306

Liu, M.-C., Chaussidon, M., Srinivasan, G., & McKeegan, K. D. 2012, The Astrophysical Journal, 761, 137

Lodders, K. 2003, The Astrophysical Journal, 591, 1220

Looney, L. W., Tobin, J. J., & Fields, B. D. 2006, The Astrophysical Journal, 652, 1755

Mac Low, M. 1999, The Astrophysical Journal, 524, 169

Makide, K., Nagashima, K., Krot, A. N., et al. 2013, Geochimica et Cosmochimica Acta, 110, 190

Marassi, S., Schneider, R., Limongi, M., et al. 2015, Monthly Notices of the Royal Astronomical Society, 454, 4250

Margolis, S. H. 1979, The Astrophysical Journal, 231, 236

Matsuura, M., Dwek, E., Barlow, M. J., et al. 2015, The Astrophysical Journal, 800, 50

McKee, C. F., & Ostriker, J. P. 1977, The Astrophysical Journal, 218, 148

McKee, C. F., & Tan, J. C. 2003, The Astrophysical Journal, 585, 850

McKeegan, K. D., Chaussidon, M., & Robert, F. 2000, Science, 289, 1334

McKeegan, K. D., & Davis, A. M. 2007, in Treatise on Geochemistry, Vol. 1 (Elsevier), 1–38

Melioli, C., de Gouveia Dal Pino, E. M., & Raga, A. 2005, Astronomy and Astrophysics, 443, 495

Meyer, B. S., & Clayton, D. D. 2000, Space Science Reviews, 92, 133

Micelotta, E. R., Dwek, E., & Slavin, J. D. 2016, Astronomy & Astrophysics, 590, A65

Miesch, M., Matthaeus, W., Brandenburg, A., et al. 2015, Space Science Reviews, 194, 97

Miettinen, O., & Offner, S. S. R. 2013, Astronomy & Astrophysics, 555, A41

Mishra, R., & Goswami, J. 2014, Geochimica et Cosmochimica Acta, 132, 440

Miyoshi, T., & Kusano, K. 2005, Journal of Computational Physics, 208, 315

Morán-López, J. T., & Schilling, O. 2013, High Energy Density Physics, 9, 112

Mouschovias, T. C., & Spitzer, L. 1976, The Astrophysical Journal, 210, 326

Moynier, F., Blichert-Toft, J., Wang, K., Herzog, G. F., & Albarede, F. 2011, The Astrophysical Journal, 741, 71

Myers, A. T., Klein, R. I., Krumholz, M. R., & McKee, C. F. 2014, Monthly Notices of the Royal Astronomical Society, 439, 3420

Myers, A. T., McKee, C. F., Cunningham, A. J., Klein, R. I., & Krumholz, M. R. 2013, The Astrophysical Journal, 766, 97

Nakamura, F., McKee, C. F., Klein, R. I., & Fisher, R. T. 2006, The Astrophysical Journal Supplement Series, 164, 477

Nozawa, T., Kozasa, T., & Habe, A. 2006, The Astrophysical Journal, 648, 435

Nozawa, T., Kozasa, T., Habe, A., et al. 2007, The Astrophysical Journal, 666, 955

Ouellette, N., Desch, S., Hester, J., & Leshin, L. 2005, in Astronomical Society of the Pacific Conference Series, Vol. 341, Chondrites and the Protoplanetary Disk, ed. A. Krot, E. Scott, & B. Reipurth (San Francisco: Astronomical Society of the Pacific Conference Series), 527

Ouellette, N., Desch, S. J., & Hester, J. J. 2010, The Astrophysical Journal, 711, 597

Padovani, M., Galli, D., & Glassgold, A. E. 2009, Astronomy and Astrophysics, 501, 619

Pagani, L., Lesaffre, P., Jorfi, M., et al. 2013, Astronomy & Astrophysics, 551, A38

Pagani, L., Vastel, C., Hugo, E., et al. 2009, Astronomy and Astrophysics, 494, 623

Palacios, A., Meynet, G., Vuissoz, C., et al. 2005, Astronomy and Astrophysics, 429, 613

Palotti, M. L., Heitsch, F., Zweibel, E. G., & Huang, Y. 2008, The Astrophysical Journal, 678, 234

Pan, L., Desch, S. J., Scannapieco, E., & Timmes, F. X. 2012, The Astrophysical Journal, 756, 102

Pantano, C., & Sarkar, S. 2002, Journal of Fluid Mechanics, 451, 329

Papamoschou, D., & Roshko, A. 1988, Journal of Fluid Mechanics, 197, 453

Parker, R. J., Church, R. P., Davies, M. B., & Meyer, M. R. 2013, Monthly Notices of the Royal Astronomical Society, 437, 946

Patel, N. A., Goldsmith, P. F., Heyer, M. H., Snell, R. L., & Pratap, P. 1998, The Astrophysical Journal, 507, 241

Peters, T., Banerjee, R., Klessen, R. S., & Low, M.-M. M. 2011, The Astrophysical Journal, 729, 72

Pfalzner, S. 2013, Astronomy & Astrophysics, 549, A82

Pittard, J. M., Falle, S. a. E. G., Hartquist, T. W., & Dyson, J. E. 2009, Monthly Notices of the Royal Astronomical Society, 394, 1351

Pittard, J. M., & Parkin, E. R. 2016, Monthly Notices of the Royal Astronomical Society, 457, 4470

Prantzos, N., & Casse, M. 1986, The Astrophysical Journal, 307, 324

Reynoso, E. M., Hughes, J. P., & Moffett, D. A. 2013, The Astronomical Journal, 145, 104

Ricker, P. M. 2008, The Astrophysical Journal Supplement Series, 176, 293

Roe, P. 1981, Journal of Computational Physics, 43, 357

Russell, S. S., Gounelle, M., & Hutchison, R. 2001, Philosophical Transactions of the Royal Society of London Series A, 359, 1991

Rybicki, G. B., & Lightman, A. P. 1985, Radiative Processes in Astrophysics (Weinheim, Germany: Wiley-VCH Verlag GmbH), doi:10.1002/9783527618170

Sahijpal, S., Soni, P., & Gupta, G. 2007, Meteoritics & Planetary Science, 42, 1529

Sarangi, A., & Cherchneff, I. 2015, Astronomy & Astrophysics, 575, A95

Sarkar, S., Erlebacher, G., Hussaini, M. Y., & Kreiss, H. O. 1989, The analysis and modelling of dilatational terms in compressible turbulence, Tech. rep., NASA Contractor Report 181959

Scannapieco, E., & Brüggen, M. 2008, The Astrophysical Journal, 686, 927

Schmidt, W. 2014, Numerical Modelling of Astrophysical Turbulence, ed. M. A. Ratcliffe, W. Hillebrandt, & M. Inglis, SpringerBriefs in Astronomy (Dordrecht: Springer), doi:10.1007/978-3-319-01475-3

Schmidt, W., & Federrath, C. 2011, Astronomy & Astrophysics, 528, A106

Schmidt, W., Niemeyer, J. C., Hillebrandt, W., & Roepke, F. K. 2006, Astronomy and Astrophysics, 450, 265

Schmidt, W., Almgren, A. S., Braun, H., et al. 2014, Monthly Notices of the Royal Astronomical Society, 440, 3051

Schönbächler, M., Carlson, R., Horan, M., Mock, T., & Hauri, E. 2008, Geochimica et Cosmochimica Acta, 72, 5330

Sedov, L. 1959, Similarity and Dimensional Methods in Mechanics (New York: Academic Press)

Seifried, D., Banerjee, R., Klessen, R. S., Duffin, D., & Pudritz, R. E. 2011, Monthly Notices of the Royal Astronomical Society, 417, 1054

Seifried, D., Pudritz, R. E., Banerjee, R., Duffin, D., & Klessen, R. S. 2012, Monthly Notices of the Royal Astronomical Society, 422, 347

Shin, M., Stone, J. M., & Snyder, G. F. 2008, The Astrophysical Journal, 680, 336

Shirley, Y. L. 2015, Publications of the Astronomical Society of the Pacific, 127, 299

Shukolyukov, A., & Lugmair, G. W. 2006, Earth and Planetary Science Letters, 250, 200

Silvia, D. W., Smith, B. D., & Shull, J. M. 2010, The Astrophysical Journal, 715, 1575

—. 2012, The Astrophysical Journal, 748, 12

Smagorinsky, J. 1963, Monthly Weather Review, 91, 99

Spalart, P., & Allmaras, S. 1992, in 30th Aerospace Sciences Meeting and Exhibit, Aerospace Sciences Meetings (Reston, Virigina: American Institute of Aeronautics and Astronautics)

Srinivasan, G., & Chaussidon, M. 2013, Earth and Planetary Science Letters, 374, 11

Stone, J. M., & Gardiner, T. 2007, Physics of Fluids, 19, 094104

—. 2009, New Astronomy, 14, 139

Stone, J. M., Gardiner, T. A., Teuben, P., Hawley, J. F., & Simon, J. B. 2008, The Astrophysical Journal Supplement Series, 178, 137

Stone, J. M., & Norman, M. L. 1992, The Astrophysical Journal, 390, L17

Sutherland, R. S., & Dopita, M. A. 1993, The Astrophysical Journal Supplement Series, 88, 253

Tachibana, S., & Huss, G. R. 2003, The Astrophysical Journal, 588, L41

Takigawa, A., Miki, J., Tachibana, S., et al. 2008, The Astrophysical Journal, 688, 1382

Tan, J. C., Beltran, M. T., Caselli, P., et al. 2014, Protostars and Planets VI, 149

Tan, J. C., Kong, S., Butler, M. J., Caselli, P., & Fontani, F. 2013, The Astrophysical Journal, 779, 96

Tan, J. C., Kong, S., Zhang, Y., et al. 2016, The Astrophysical Journal, 821, L3

Tang, H., & Dauphas, N. 2012, Earth and Planetary Science Letters, 359-360, 248

Tasker, E. J., Brunino, R., Mitchell, N. L., et al. 2008, Monthly Notices of the Royal Astronomical Society, 390, 1267

Taylor, G. 1950, Proceedings of the Royal Society of London Series A, 201, 159

Toro, E. F. 2009, Riemann Solvers and Numerical Methods for Fluid Dynamics: A Practical Introduction, 3rd edn. (Berlin Heidelberg: Springer-Verlag)

Tóth, G., & Roe, P. 2002, Journal of Computational Physics, 180, 736

Travis, B. J., & Schubert, G. 2005, Earth and Planetary Science Letters, 240, 234

Trinquier, A., Birck, J.-L., Allègre, C., Göpel, C., & Ulfbeck, D. 2008, Geochimica et Cosmochimica Acta, 72, 5146

Urey, H. C. 1955, Proceedings of the National Academy of Sciences, 41, 127

van Leer, B. 2006, Communications in Computational Physics, 1, 192

Vasileiadis, A., Nordlund, Å., & Bizzarro, M. 2013, The Astrophysical Journal, 769, L8

Vázquez-Semadeni, E., Gómez, G., Jappsen, A., et al. 2007, The Astrophysical Journal, 657, 870

Vlaykov, D. G., Grete, P., Schmidt, W., & Schleicher, D. R. G. 2016, Physics of Plasmas, 23, 062316

Vreman, A. W., Sandham, N. D., & Luo, K. H. 1996, Journal of Fluid Mechanics, 320, 235

Wasserburg, G. J., Busso, M., Gallino, R., & Raiteri, C. M. 1994, The Astrophysical Journal, 424, 412

Wilcox, D. C. 1988, AIAA Journal, 26, 1299

—. 1992, AIAA Journal, 30, 2639

—. 1998, Turbulence Modeling for CFD (Second Edition), 2nd edn. (La Cañada, CA: DCW Industries, Inc.)

—. 2006, Turbulence Modeling for CFD (Third Edition), 3rd edn. (La Cañada, CA: DCW Industries, Inc.)

—. 2008, AIAA Journal, 46, 2823

Wolfire, M. G., Hollenbach, D., Mckee, C. F., Tielens, A. G. G. M., & Bakes, E. L. O. 1995, The Astrophysical Journal, 443, 152

Wongwathanarat, A., Müller, E., & Janka, H.-T. 2015, Astronomy & Astrophysics, 577, A48

Woosley, S. E., & Heger, A. 2007, Physics Reports, 442, 269

Wyrowski, F., Güsten, R., Menten, K. M., et al. 2016, Astronomy & Astrophysics, 585, A149

Xu, J., & Stone, J. M. 1995, The Astrophysical Journal, 454, 172

Young, E. D. 2014, Earth and Planetary Science Letters, 392, 16

Young, E. D., Gounelle, M., Smith, R. L., Morris, M. R., & Pontoppidan, K. M. 2011, The Astrophysical Journal, 729, 43

Young, E. D., Simon, J., Galy, A., et al. 2005, Science, 308, 223

Zeman, O. 1990, Physics of Fluids A: Fluid Dynamics, 2, 178

Zinnecker, H., & Yorke, H. W. 2007, Annual Review of Astronomy and Astrophysics, 45, 481